

**A Study of Sparse Linear Array Configurations:
Unifying Array Designs for Passive Sensing**

(スパーズリニアアレーの構成に関する研究:
パッシブセンシングのためのアレー設計法)

A Dissertation Submitted
in Partial Fulfilment of the Requirements
for the Degree of

Doctor of Engineering
in
Electrical and Computer Engineering

by

Steven Wandale

to

**Graduate School of Engineering Sciences
Yokohama National University**

September 2023

Copyright ©

Steven Wandale (ORCID:[0000-0002-4118-5000](https://orcid.org/0000-0002-4118-5000))

All rights reserved.

Acknowledgement


I sincerely thank my mentor, Professor Koichi Ichige, who graciously accepted me as his student. His unwavering guidance, encouragement, and professional insights have helped me navigate challenging waters. Moreover, his steadfast support has been instrumental in my academic journey.

My appreciation extends equally to the members of the thesis committee: Professors Hiroyuki Arai, Toshihiko Baba, Hideki Ochiai, Nobuhiro Kuga and Naoki Ishikawa. Amid their demanding schedules, they have generously dedicated time to assess my work. Their insightful feedback and constructive criticism have substantially improved the quality of my thesis.

I sincerely thank the government of Malawi and the University of Malawi (UNIMA) for their consistent support throughout my studies. I also wish to acknowledge my esteemed colleagues at the Department of Physics, UNIMA. Additionally, I'm grateful to the Japanese government and its Malawi embassy for the honor of the MEXT Scholarship.

Collaborating with my colleagues at the Ichige Laboratory has been a transformative experience. Our intellectual exchanges, collective victories, and (other) shared challenges have significantly contributed to my professional growth. I am profoundly thankful for their input and privileged to be part of such an exceptional team.

Lastly, my heartfelt thanks go to my supportive family and everyone who, directly or indirectly (including Symon Mkandawire, Dr. T. Basikolo, and Associate Prof. C. Mikeka), contributed to the successful completion of this research project.



Steven Wandale, (Reg. # 20QC598)

Dedicated to my mother

Abstract

Direction-of-arrival (DOA) estimation is a process of determining the direction of electromagnetic sources from the output of a receiving sensor array. The approach has a wide range of applications in radar, astronomy, imaging, wireless communication, and other fields. Sparse linear arrays (SLAs) have gained popularity in this industry due to their increased degrees of freedom (DOF). Given a concept of difference co-array (DCA), the SLAs retain a $\mathcal{O}(N^2)$ long central uniform linear array (ULA) segment in their DCA, which increases their DOF and allows them to resolve $\mathcal{O}(N^2)$ uncorrelated sources with only N sensors. The classic ULA, on the other hand, can only estimate $N - 1$ sources given N sensors. The conventional SLAs include minimum redundancy arrays (MRAs), nested arrays (NAs), and coprime arrays (CAs). These arrays, however, have shortcomings ranging from a lack of closed-form expression (MRAs) to incomplete difference coarray (CAs) and strong mutual coupling (NAs). Hence, this paper explores innovative sparse linear array design methodologies for sparse arrays with high DOF and low mutual coupling.

The key contribution of this dissertation is to offer new design approaches for SLAs. The first part of this dissertation introduces novel fundamental SLA designs including the extended nested array with multiple subarrays (ENAMS) and its extension, the flexible ENAMS (f-ENAMS). These SLAs offer improved DOF and high-resolution DOA estimation compared to existing ones. Besides, the trade-offs between robustness to mutual coupling (MC) and DOA estimation accuracy are also provided to demonstrate the effectiveness of the proposed array designs. The second part of this dissertation introduces novel unified SLA configurations via the interelement spacing criterion (IES) with higher DOF and relatively reduced MC effect. The unified SLAs include the generalized ENAMS (GENAMS) and the enhanced sparse array via the maximum IES criterion (xMISC). The unified SLAs show improved DOF and high-resolution DOA estimation performance compared to state-of-the-art SLAs, even in mutual coupling scenarios. Furthermore, the paper develops a simulated annealing (SA)-assisted deep learning-based sparse array design method. The two-stage method leverages the SA algorithm to circumvent the computationally expensive stage of dataset notation, thereby alleviating overall computation time. Naturally, the paper concludes with remarks on future research directions.

Contents

List of Figures	viii
List of Tables	xiii
1 Introduction	1
1.1 Introduction	1
1.2 Fundamentals of array signal processing	2
1.3 Contributions	5
1.4 Scope and outline of the dissertation	8
1.5 Notations	9
2 Review of Difference Coarray Concept and Sparse Linear Arrays	10
2.1 Introduction	10
2.2 Coarray signal model for DOA estimation	11
2.2.1 Coarray signal model for sparse linear arrays	11
2.2.2 The coarray signal model and mutual coupling effect	14
2.2.3 Coarray-based direction-of-arrival estimator	15
2.2.4 Extension to sparse planar arrays	16
2.3 Conventional sparse linear arrays	18
2.3.1 Minimum redundancy array	18
2.3.2 Nested array	19
2.3.3 Coprime array	20
2.3.4 A note on MRA, NA and PCA array properties	21
2.4 Conventional sparse planar arrays	22
2.4.1 Open box array	22
2.4.2 SA-based sparse planar arrays	24
2.5 Chapter summary	25
3 A Nested Array Geometry with Enhanced Degrees of Freedom and	

Hole-Free Difference Coarray	26
3.1 Introduction	26
3.2 Conventional sparse linear arrays	28
3.2.1 1D representation of NA and extended NA	28
3.2.2 2D representation of NA and extended NA	29
3.3 The proposed ENAMS array design	30
3.4 Numerical examples	33
3.4.1 Co-array, weight functions, and achievable DOF	33
3.4.2 MUSIC spectra of DOA estimation	35
3.4.3 RMSE of DOA estimation	35
3.5 Chapter summary	38
4 Flexible Extended Nested Array with Multiple Subarrays Achieving Improved Degrees of Freedom	39
4.1 Introduction	39
4.2 Conventional sparse linear arrays	41
4.3 Proposed flexible ENAMS array designs	41
4.3.1 Flexible Extended NA with Multiple Subarrays-I	42
4.3.2 Flexible extended NA with multiple subarrays-II	44
4.4 Numerical examples	47
4.4.1 Achievable degrees of freedom	47
4.4.2 Weight functions	48
4.4.3 DOA estimation in the absence of mutual coupling	50
4.4.4 DOA estimation in the presence of mutual coupling	51
4.5 Chapter summary	52
5 A Generalized Extended Nested Array Design via Maximum InterElement Spacing Criterion	58
5.1 Introduction	58
5.2 Conventional sparse linear arrays	59
5.2.1 Maximum interelement spacing constrained array	60
5.2.2 TS-ENA array via interelement spacing criterion	61
5.2.3 Flexible ENAMS array via IES principle	62

5.2.4	TS-ENA vs. flexible ENAMS array configuration	63
5.3	Proposed generalized ENAMS array design	65
5.4	Numerical examples	67
5.4.1	DOF capacity and coupling leakage analysis	68
5.4.2	RMSE of DOA estimation in the presence of MC	69
5.5	Chapter summary	70
6	xMISC: Improved Sparse Linear Array via Maximum Inter-Element Spacing Concept	72
6.1	Introduction	72
6.2	Conventional improved MISC array	73
6.3	Hole analysis and filling strategy	75
6.3.1	Hole Identification and Anaysis	75
6.3.2	Hole filling strategy	75
6.4	Proposed enhanced MISC array design	78
6.5	Numerical examples	79
6.5.1	DOF capacity and mutual coupling analysis	79
6.5.2	RMSE of DOA estimation in the presence of MC	81
6.6	Chapter summary	81
7	Sparse Array Design via Deep Learning: Trade-Offs Analysis	84
7.1	Introduction	84
7.2	Antenna selection and sparse array design	86
7.3	Review of sparse array design	87
7.3.1	Heuristic optimization methods	87
7.3.2	Machine learning methods	89
7.4	Trade-off analysis	95
7.4.1	Computational complexity analysis	95
7.4.2	Quality analysis: DOA estimation performance	98
7.5	Chapter summary	100
8	Concluding Remarks and Future Work	102
8.1	Concluding remarks	102
8.2	Future work	103

Bibliography	105
Appendix A Proof of Lemmata and Properties of Chapter 3	119
Appendix B Proof of Lemmata and Properties of Chapter 4	123
Appendix C Proof of Lemmata and Properties of Chapter 5	126
Appendix D Proof of Lemmata and Properties of Chapter 6	128
Author's Curriculum Vitae	131

List of Figures

Number	Page
1.1	The basic representation of sensor array signal processing. 2
1.2	The basic direction finding setup using (a) ULA and (b) non-uniform/sparse array. Here, the \bullet and \times represent a physical sensor and a blank space. 3
2.1	The sparse linear arrays are \mathbb{S}_a , \mathbb{S}_b , and \mathbb{S}_c , and their difference co-arrays are \mathbb{D}_a , \mathbb{D}_b , and \mathbb{D}_c , respectively. Here, the \bullet and \times denote a sensor and a blank space, respectively. 13
2.2	Examples of 2D sparse arrays with $N = 9$ and their corresponding difference co-array. Here, (a) shows a 2D sparse array with <i>holes</i> , and (b) its corresponding difference co-array, whereas (c) shows a hole-free 2D sparse array, and (d) its corresponding difference coarray. Note, the crosses, circles, and brown circles represent empty spaces, physical sensors, and virtual sensors. 17
2.3	The MRA array configuration with $N = 10$ sensors and corresponding coarray weight functions (only positive segment is shown in the view of $w(n) \in [0, 15]$). In the figure, the red stems denote physical sensors. 19
2.4	The NA array configuration with $N = 10$ sensors ($N_1 = N_2 = 5$) and corresponding coarray weight functions (only positive segment is shown in the view of $w(n) \in [0, 10]$). In the figure, the red stems denote physical sensors. 20
2.5	The PCA array configuration with $\bar{N} = 12$ sensors ($M = 6, N = 7$) and corresponding coarray weight functions (only positive segment is shown in the view of $w(n) \in [0, 15]$). In the figure, the red stems denote physical sensors. 21
2.6	(a) The OBA array configuration with ($N_x = 7, N_y = 6$) and (b) its corresponding difference co-array. Here, the circles, and asterisks represent physical sensors and virtual sensors. 23

2.7	(a) The SAPSA array configuration with ($N_x = 7, N_y = 6$) and (b) its corresponding difference co-array. Here, the circles, and asterisks represent physical sensors and virtual sensors.	25
3.1	Comparison of sparse linear array configurations. Here, (a) NA with $N_1 = N_2 = 5$ and $N = 10$, and (b) ENA array with $N_1 = N_2 = 5$ and $N = 10$. The bullets denote physical sensors, and empty spaces stand for crosses.	29
3.2	The 2D representation of 1D sparse linear array configurations with $N_1 = N_2 = 5$ and $N = 10$ sensors. Here, (a) 1D representation of NA, (b) 2D representation of NA, (c) 2D representation of ENA, and (d) 2D representation of ENAMS array. Note the bullets denote physical sensors, and empty spaces stand for crosses. Notations: i) black bullets (dense ULA sensors), ii) red bullets (sparse ULA sensors), and iii) blue dotted circles (relocated sensors).	30
3.3	The sparse linear array configurations of ENAMS array with $N_1 = N_2 = 5$ and $N = 10$ sensors. The bullets denote physical sensors, and empty spaces stand for crosses.	31
3.4	Comparison of sparse linear array configurations and their corresponding coarray weight functions (only positive segment is shown in the view of $w(n) \in [0, 15]$).	34
3.5	The SS-MUSIC spectra $P(\bar{\theta})$ for the NA, ENA, ENAMS and MRA when $N = 12$ and $K = 26$ normalized sources distributed in the range $-0.3 \leq \bar{\theta} \leq 0.3$. The SNR is 0 dB, while the number of snapshots is 500. The dotted lines on the x-axis denote the true DOAs.	36
3.6	RMSE of DOA estimation performance for different sparse linear arrays where (a) SNR= $-30 \sim 10$ dB with 500 snapshots and (b) $100 \sim 1000$ snapshots with 0 dB SNR.	37
3.7	RMSE of DOA estimation performance for different sparse linear arrays where (a) $ c_1 = 0 \sim 0.6$ with 0 dB SNR, 500 snapshots and (b) $K = 10 \sim 50$ with 0 dB SNR, 500 snapshots.	38

4.1	(a) Nested array configuration with $N_1 = N_2 = 6$, and $N = 12$, and (b) corresponding difference co-array. (c) f-ENAMS-I array configuration with $N_1 = 10$, $N_2 = 2$, and $N = 12$, and (d) corresponding difference co-array. The bullets denote physical sensors and the crosses represent empty spaces.	43
4.2	(a) an example of f-ENAMS-II array with $N_1 = 14$, $N_2 = 2$, and $N = 16$, and (b) corresponding difference co-array. The bullets denote physical sensors and the crosses represent empty spaces.	43
4.3	The DOF ratio $\gamma(N)$ versus the number of sensors N varying from 16 to 100.	49
4.4	The weight functions for various sparse linear arrays with 22 sensors. (a) ENAMS, (b) Improved NA, (c) f-ENAMS-I, (d) MISC array, (e) TS-ENA, and (f) f-ENAMS-II.	53
4.5	MUSIC spectra $P(\bar{\theta})$ comparison among (a) ENAMS, (b) Improved NA, (c) f-ENAMS-I, (d) MISC array, (e) TS-ENA and (f) f-ENAMS-II. The MUSIC spectra are computed using $N = 22$, $\text{SNR} = 0$ dB, 500 snapshots and $K = 32$ sources distributed in $\bar{\theta} = [-0.1, 0.1]$. Note, the dotted vertical lines on the $\bar{\theta}$ axis denote true DOAs.	54
4.6	RMSE of the normalized DOA estimates versus the input SNR when $T = 1000$	55
4.7	RMSE of the normalized DOA estimates versus the number of snapshots when $\text{SNR} = 0$ dB.	55
4.8	RMSE of the normalized DOA estimates versus the number of sources when SNR is 0 dB, $N = 22$, $T = 1000$ and K sources are located at $\bar{\theta}_k = -0.3 + 0.6(k - 1)/(K - 1)$ for $1 \leq k \leq K$	56
4.9	RMSE of the normalized DOA estimates versus the input SNR when the number of snapshots $T = 1000$, $N = 22$ and $K = 50$ sources are located at $\bar{\theta}_k = -0.3 + 0.6(k - 1)/49$ for $1 \leq k \leq 50$	56
4.10	RMSE of the normalized DOA estimates versus $ c_1 $ when SNR is 0 dB, $N = 22$, $T = 1000$ and $K = 50$ sources are located at $\bar{\theta}_k = -0.3 + 0.6(k - 1)/49$ for $1 \leq k \leq 50$	57

5.1	The MISC array configuration with $N = 12$ sensors ($Q = 8, r = 4, z = 2$) and corresponding coarray weight functions (only positive segment is shown in the view of $w(n) \in [0, 15]$). In the figure, the red stems denote physical sensors.	60
5.2	The TS-ENA array configuration with $N = 17$ sensors ($N_1 = 14$ and $N_2 = 2$) and corresponding coarray weight functions (only positive segment is shown in the view of $w(n) \in [0, 15]$). In the figure, the red stems denote physical sensors.	62
5.3	The f-ENAMS-2 array configuration with $N = 17$ sensors ($N_1 = 14$ and $N_2 = 2$) and corresponding coarray weight functions (only positive segment is shown in the view of $w(n) \in [0, 20]$). In the figure, the red stems denote physical sensors.	63
5.4	Comparison of the DOF ratio versus the number of sensors N for various z -level sparse arrays.	65
5.5	An example of the GENAMS array with $N = 10$ sensors ($Q = 7, r = 3, P = 3$ and $z = 2$) and corresponding coarray weight functions (only positive segment is shown in the view of $w(n) \in [0, 10]$). In the figure, the red stems denote physical sensors.	66
5.6	Comparison of DOF ratio $\gamma(N)$ versus the number of sensors N for various sparse linear arrays.	68
5.7	Comparison of coupling leakage $L(N)$ versus the number of sensors N for various sparse linear arrays.	69
5.8	Comparison of RMSE versus input SNR for various sparse linear arrays.	70
5.9	Comparison of RMSE versus $ c_1 $ for various sparse linear arrays. . . .	71
6.1	Comparison of sparse linear array configurations and their difference co-arrays. (a) Improved MISC array and (b) its difference co-array where \mathbb{H}_o is the location set of holes. (c) Relaxed IMISC and (d) its difference co-array where \mathbb{H}_1 and \mathbb{H}_2 denote the 1st and 2nd set of holes, respectively. Finally, (e) Enhanced MISC array where the dotted line represents sensor relocation and (f) its difference co-array.	77
6.2	Performance of the xMISC array in terms of the DOF ratio $\gamma(N)$. . .	80
6.3	Performance of the xMISC array in terms of the coupling leakage $L(N)$.	81

6.4	Comparison of the DOF ratio and coupling leakage for different arrays.	82
6.5	Performance of the xMISC array in terms of the RMSE versus SNR.	82
6.6	Performance of the xMISC array in terms of the RMSE versus $ c_1 $.	83
7.1	(a) The flow diagram of simulated annealing algorithm for optimization of HA.	89
7.2	The array configurations of (a) parent 42-sensor URA, (b) the conventional DL-based array (16-sensors), (c) the conventional SA-based array (16-sensors) and (d) the proposed DL-based array (16-sensors). Note that the dots denote physical sensors.	95
7.3	Comparison of DOA estimation of the conventional and proposed method for different array configurations.	96
7.4	Performance of the conventional and SA-assisted method for different SNR_{TEST} values.	97
7.5	Comparison of computation time between the DL-based and traditional SA sparse array design techniques.	98
7.6	RMSE versus input SNR performance of different 2D sparse arrays.	101
7.7	RMSE versus the number of snapshot performances of different 2D sparse arrays.	101

List of Tables

Number		Page
2.1	Comparison of achievable uniform DOF and weight functions of different sparse linear arrays	22
3.1	Comparison of achievable DOF of various sparse arrays	35
4.1	Achievable uniform DOF of different sparse linear arrays	48
7.1	Realized training data for various techniques	93
7.2	Simulation parameters for estimation performance evaluation	94
7.3	Comparison of the computation complexity of the deep learning and SA-based sparse array design methods	97
7.4	2D DOA estimation simulation parameters	100

Introduction

1.1 Introduction

Sensor arrays are one of the critical components in 21st-century technologies as they yield captured environmental signals as output for various applications, including wireless communication [1], biomedical engineering (medical imaging, bioinformatics, wearable technology) [2]-[4], and so forth [5]-[6]. With the upcoming 5th generation (5G) network, the highest data rates can be achieved at millimeter-Wave (mmWave) frequencies [7]. However, high path loss and attenuation at these frequencies and interference among components necessitate efficient mitigation strategies while addressing compactness and performance constraints. Achieving this remains a problem to this day, but the progress in computing technology has made it possible to address some of these issues through sparse sensing [8].

Sparse sensing (SS) is characterized by sparse sampling and inference [8]. Collection of a few samples of high-dimensional data based on prior knowledge and transferring it to signal processors to recover low-dimensional information of interest under specific conditions entail sparse sampling [9]-[12]. Sparse sampling is one of the most researched areas in signal processing, and many SS methods such as nested samplers [9], coprime samplers [10], and many more [11]-[12], have demonstrated widespread applications in source direction finding, cognitive wireless systems, and imaging [12]. These approaches offer reduced data rates while maintaining performance levels comparable to traditional methods [13].

This thesis focuses on source localization as applied in various areas such as wireless communication, sonar, seismography, and so on [14]. And in this context, sparse samplers correspond to sparse sensor array configuration, and information inference relates to angle/direction-of-arrival estimation (AOA or DOA), estimation of signal's amplitude, power, speed, and related parameters as the post-processed output [8], [15]. More specifically, it focuses on DOA estimation within the source localization area. Typically, DOA estimation can be considered as a two-fold problem: a) design

of an optimal sampler or sensor array configuration that captures the DOAs accurately and efficiently; and b) given the solution for a) developing a DOA estimation algorithm to resolve the DOAs based on the output from the array. The following introduces the basic array signal equation that forms the basic building block of most intricate array signal processing problems.

1.2 Fundamentals of array signal processing

In general array signal processing, the outline in Fig. 1.1 summarizes the basic arrays signal model where the arrows indicate the environmental source signals waves impinging the sensor array. The array signal-processing algorithm processes the output from the array to infer the signal’s information, i.e., waveforms, frequencies, DOAs, and so forth [8], [16]. For the sake of generalization, the primary array signal model, as shown in Fig. 1.1, can be derived into an array signal equation, forming the foundation for the most intricate computations in sensor array signal processing.

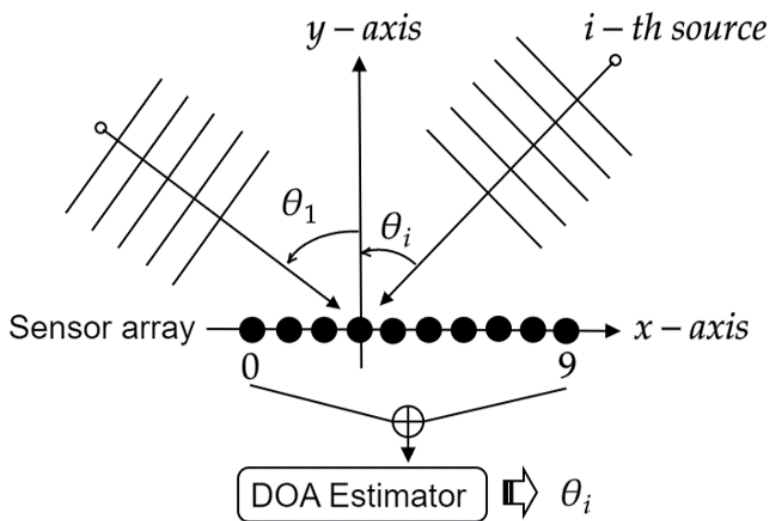


Figure 1.1: The basic representation of sensor array signal processing.

For simplicity, we assume that the sensors in the array are uniformly spaced in d steps on the x-axis (unless otherwise stated). Thus, nd for $n \in \mathbb{S}$ where \mathbb{S} contains the physical array sensor positions [8]. Figure Fig. 1.2 (a) depicts the uniform

linear array (ULA) with 10 sensors where the dots denote physical sensors. As shown in Fig. Fig. 1.2 (a), the sensors are located at $\mathbb{S} = \{0, 1, 2, 3, 4, 5, 6, 7, 8, 9\}d$. Usually, the $d = \lambda/2$ but for simplicity, d is normalized to 1. Hence, \mathbb{S} becomes $\mathbb{S} = \{0, 1, 2, 3, 4, 5, 6, 7, 8, 9\}$.

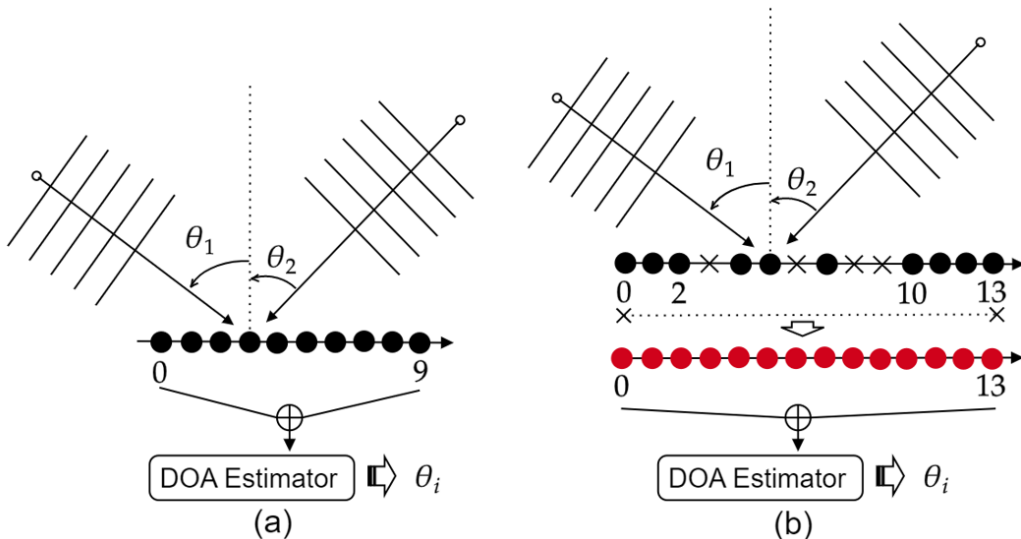


Figure 1.2: The basic direction finding setup using (a) ULA and (b) non-uniform/sparse array. Here, the \bullet and \times represent a physical sensor and a blank space.

Consider a linear array with N -sensors, whose sensor positions are $n_i d$ where n_i belongs to $\mathbb{S} = \{n_i\}_{i=1}^N$ and $d = \lambda/2$ is the unit intersensor spacing, with λ being the wavelength of the source signal [17]. Assume K uncorrelated narrowband far-field sources from directions $\theta_k, k = 1, 2, \dots, K$ are impinging on the array [4]. Then, the received signal vector at time t can be expressed as

$$\mathbf{x}(t) = \mathbf{B}\mathbf{s}(t) + \mathbf{n}(t), \quad (1.1)$$

such that $\mathbf{s}(t) = [s_1(t), s_2(t), \dots, s_K(t)]^T$ is the signal vector and $\mathbf{n}(t)$ denotes the zero mean white Gaussian noise vector with variance $\sigma_n^2 \mathbf{I}_N$, where σ_n^2 is the noise power. Moreover, $\mathbf{B} = [\mathbf{b}(\theta_1), \mathbf{b}(\theta_2), \dots, \mathbf{b}(\theta_K)]$ is the array manifold whose k -th source steering vector $\mathbf{b}(\theta_k)$ can be expressed as

$$\mathbf{b}(\theta_k) = [e^{j\pi d_1 \sin(\theta_k)}, e^{j\pi d_2 \sin(\theta_k)}, \dots, e^{j\pi d_N \sin(\theta_k)}]^T. \quad (1.2)$$

The covariance of $\mathbf{x}(t)$ can be defined as

$$\mathbf{R}_{\mathbf{xx}} = E[\mathbf{x}(t)\mathbf{x}^H(t)] = \mathbf{B}\mathbf{R}_s\mathbf{B}^H + \sigma_n^2\mathbf{I}_N, \quad (1.3)$$

where $\mathbf{R}_s = E[\mathbf{s}(t)\mathbf{s}^H(t)] \approx \text{diag}([\rho_1^2, \rho_2^2, \dots, \rho_K^2])$ is the signal covariance matrix and ρ_k^2 denotes the signal power. This signal model assumes that the signals from the source are not related and have a circularly symmetric complex Gaussian distribution with zero mean [8]. The directions of arrival for each source are unique. The noise added is circularly symmetric and complex, with no correlation to the sources. Additionally, there is no temporal correlation between snapshots [8], [17]. Thus, either $\mathbf{R}_{\mathbf{xx}}$ or \mathbf{x} can be further manipulated using different DOA estimation algorithms depending on the nature of the sensor array to resolve the sources [17]-[30].

Traditionally, ULAs have been widely used to tackle this problem in conjunction with where DOA estimators like the Bartlett [17], Capon beamformer [18], the Pisanenko [19], the minimum-norm [20], Multiple Signal Classification (MUSIC) [21]-[25], maximum likelihood estimator [26], method of DOA estimation (MODE) [27] and its variants [28]-[30]. However, ULA can only resolve up to $N - 1$ sources given N physical sensors. Besides, adding more sensors could improve the resolution but at the cost of extra hardware costs and computation complexity, which is limiting when the limited mounting platform and computing capacity are available [31].

To circumvent this, recently, with the development of the concept of difference co-array, it is possible to estimate more sources than the number of sensors using sparse arrays (see Fig. 1.2 (b)). The difference co-array is expressed as the difference between the sensor positions, i.e., $\mathbb{D} = \{n_1 - n_2 | n_1, n_2 \in \mathbb{S} \text{ where } \mathbb{S} \text{ contains sensor locations [32]. So based on the difference co-array, various co-array-based methods, including Toeplitz completion [32], spatial smoothing MUSIC [33]-[34], co-array interpolation [35]-[36], and Khatri-Rao methods [37]-[40]. In array signal processing, especially when dealing with the underdetermined case where there are more sources than the number of sensors, two problems emerged to be of paramount importance: a) reducing the mutual coupling (MC) effect between sensors that have a detrimental effect on source estimation accuracy, and b) enhancing the aperture while maintaining the difference coarray to increase the degrees of freedom [33], [41].$

Furthermore, a number of sparse arrays have been proposed over the decades

alongside these co-array-based DOA estimators [9]-[10], [42]-[73]. The classic ones include minimum redundancy arrays [42], minimum hole arrays [43], nested arrays [9], and coprime arrays [10]. Later, with efforts to realize sparse arrays with enhanced degrees of freedom and reduced mutual coupling, several variations of the nested array and coprime arrays have been introduced [44]-[73]. Besides, those sparse arrays with incomplete difference co-array make application of co-array-based methods challenging to apply as it requires a complete difference co-array, coarray interpolation methods have been proposed over the years to fill in the missing lags [74]-[81]. Moreover, learning-based methods have also been exploited to solve sparse array design and DOA estimation problems [82]-[109]. More details reviews of some of the well-known sparse arrays will be discussed in Chapter 2.

In light of all this discussion on DOA estimation, and sensor arrays, the original contribution of this thesis focuses on the design of optimal sparse linear array geometries with enhanced degrees of freedom for DOA estimation. The following discusses the contributions of this study in detail.

1.3 Contributions

The main contributions in this thesis are summarized as follows:

- **Extended nested array with multiple subarrays**

Although the classic sparse arrays such as nested arrays, coprime arrays, minimum redundancy, and minimum hole arrays are well-known, these sparse arrays have disadvantages. The minimum redundancy array and minimum hole arrays lack closed-form expressions for sensor positions, and the coprime arrays have holes in their co-array. Besides, the nested arrays have dense, closely spaced subarray, contributing immensely to the mutual coupling effect. As such, this chapter introduces a new extended nested array with multiple subarrays with enhanced degrees of freedom and hole-free difference co-array. The systematic approach is used to derive a closed-form expression for sensor positions, weight functions of closely spaced sensors, and achievable degrees of freedom. Furthermore, the theoretical properties above are proved, and numerical sim-

ulation examples demonstrate the superiority of the proposed array.

- **Flexible extended nested array with multiple subarrays**

Despite that, the proposed extended nested array with multiple subarrays has closed-form expression for sensor positions, enhanced degrees of freedom, and reduced mutual coupling than coprime array and nested array. The achievable degrees of freedom of the extended nested array with multiple subarrays are still limited compared to some of the state-of-the-art sparse linear arrays such as maximum interelement spacing constrained array (MISC), and one/two sides extended nested arrays (OS/TS-ENA).

Next, based on the rudimentary structure of an extended nested array with multiple subarrays, we extended the ENAMS array further by designing a systematic approach of relocating multiple sensors from the dense subarray of the nested array, thereby forming a flexible extended nested array with multiple subarrays (f-ENAMS). And depending on the number of sensors that can be relocated, the f-ENAMS is further divided into Type-I (relocates two sensors) and Type-II (relocates three sensors). The proposed arrays enjoy all good coarray properties of the ENAMS array with enhanced degrees of freedom compared to other state-of-the-art arrays. The closed-form expression for sensor positions, weights functions, and achievable degree of freedom are derived in detail. Moreover, the properties above are theoretically proved, and numerical examples are used to demonstrate the performance of the proposed flexible extended nested array with multiple subarrays.

- **Unified extended nested array with multiple subarrays**

In sparse array design, the array is often represented using a set of integers where each integer denotes a sensor. Although it is a widely accepted method to describe a sparse array, it does not offer much information about the array structure, especially the fundamental sensor distribution pattern within the array. Recently, a new technique known as the interelement spacing criterion has been proposed that uses the spacing between consecutive sensors in the

array to describe the array. Thus, the interelement spacing approach uses a set of interelement spacing terms to describe an array instead of a set of integers. Apart from the compactness of the set, the interelement spacing criterion depicts the sensor distribution pattern of a sparse array.

Therefore, using the interelement spacing technique, a new generalized extended nested array with multiple subarrays via an extension of a two-sides extended nested array and a flexible extended nested array with multiple subarray Type-II is proposed. Basic sensor distribution patterns of two-sides extended nested array and flexible extended nested array with multiple subarrays demonstrate that the two share a similar basic array pattern, and a unified pattern is derived from the two arrays. Thus, the unified array shares all good properties of the extended nested array with multiple subarrays except for enhanced degrees of freedom. The closed-form expressions for sensor positioning, weight functions, and achieved are derived in detail and proved. Numerical examples demonstrate that the proposed unified array has enhanced degrees of freedom and high-resolution direction-of-arrival estimation performance.

- **Enhanced maximum interelement constrained array design via simple hole-filling strategy**

Taking the reduced mutual coupling perspective, one of the recently proposed sparse arrays with reduced MC effect and improved DOF is an improved sparse array via maximum interelement spacing (IMISC) criterion. The IMISC array is an IES-based sparse array with a balanced reduced MC effect and DOF. However, it is not hole-free. Hence, the realized DOF is limited.

Considering the limitations of IMISC, we propose an enhanced sparse array design via the maximum interelement spacing constraint (xMISC) criterion. The xMISC array is developed by filling the holes in the conventional improved MISC array (IMISC). First, the hole locations in the IMISC array are analyzed, then a simplified hole-filling strategy is proposed to recover the missing lags. Compared to the existing MISC and IMISC arrays, the xMISC array exhibits enhanced uniform degrees of freedom (uDOF) while maintaining relatively re-

duced mutual coupling. Besides, the xMISC retains a hole-free difference coarray. The closed-form expressions for sensor locations, weight functions, and achievable DOF are also derived in detail. Numerical examples validate the merits of the xMISC array.

- **Sparse array design via deep learning: trade-offs analysis**

The prior work introduced a method for designing sparse arrays using a combination of a convolutional neural network (CNN) and simulated annealing (SA). This method involves two stages: i) generating data using the SA algorithm and ii) annotating the data and the CNN implementation. Traditionally, machine learning techniques for sparse array design require creating a large dataset by enumerating all possible combinations, which can be computationally expensive. However, the proposed SA algorithm generates only the necessary samples, optimizing them to meet specific objectives and streamlining the labeling process. While numerical examples showed the effectiveness of the DL-based method, the paper did not discuss the computation complexity and accuracy trade-offs between the SA and the proposed method. Therefore, the problem is revisited, and the proposed technique and analyze its trade-offs in comparison with the conventional method. The analysis shows that the DL-based method produces optimal sparse arrays with minimal matrix computations and has a fast computation time, making it more suitable and efficient for larger and more complex problems than the SA algorithm. In other words, this chapter answers whether the SA algorithm, which can generate good sparse array samples, has any advantages over the ML-based approach.

1.4 Scope and outline of the dissertation

The preliminaries to sparse array signal processing and conventional sparse array designs are discussed in Chapter 2. Following Chapter 2, the thesis is divided into two parts. The first part of the thesis considers basic sparse linear array designs (Chapters 3 and 4), including extended nested array with multiple subarrays (ENAMS), the flexible extended nested array with multiple subarrays Type-I (f-ENAMS-I), and the

flexible extended nested array with multiple subarrays Type-II (f-ENAMS-II). The second part introduces generalized sparse linear array designs, such as generalized extended nested arrays with multiple arrays (Chapter 5) and enhanced sparse via maximum interelement spacing criterion array (Chapter 6). Lastly, Chapter 7 discusses the sparse array design via a deep learning approach. In conclusion, Chapter 8 summarizes the thesis and discusses potential future research directions on sparse array designs for DOA estimation and source localization applications.

1.5 Notations

Throughout this thesis, the operators $[\cdot]^*$, $[\cdot]^T$, $[\cdot]^H$, $[\cdot]^{-1}$ and $|\cdot|$ represent complex conjugate, transpose, complex conjugate transpose, and inverse operation. Besides, $\|\cdot\|$, \odot , \otimes , $\text{vec}(\cdot)$, and $E[\cdot]$ denote norm, Khatri-Rao product (KR product), Kronecker product, vectorization and statistical expectation operators. The vectors, matrices, and sets of numbers are represented by $\{\mathbf{a}, \mathbf{b}, \dots, \mathbf{x}, \mathbf{y}, \mathbf{z}\}$, $\{\mathbf{A}, \mathbf{B}, \dots, \mathbf{X}, \mathbf{Y}, \mathbf{Z}\}$ and $\{\mathbb{A}, \mathbb{B}, \mathbb{C}, \dots, \mathbb{X}, \mathbb{Y}, \mathbb{Z}\}$, respectively. Special matrices like diagonal and identity matrices are denoted as $\text{diag}(\cdot)$ and \mathbf{I} , in that order. The notation $\langle r_1, r_2 \rangle$ denotes an integer set, i.e., $\{r \in \mathbb{S} | r_1 \leq r \leq r_2\}$ whereas $\mathcal{O}(\cdot)$ denotes order symbol. The set $\text{diff}(\mathbb{A}, \mathbb{A})$ means self-difference set, i.e., $\{a_i - a_j | a_i, a_j \in \mathbb{A}\}$ while set $\text{diff}(\mathbb{A}, \mathbb{B})$ stands for cross-difference set, i.e., $\{a_i - b_j | a_i \in \mathbb{A}, b_j \in \mathbb{B}\}$.

Review of Difference Coarray Concept and Sparse Linear Arrays

2.1 Introduction

In the direction-of-arrival (DOA) estimation field, it is well known that the conventional subspace-based DOA estimation methods can resolve up to $N - 1$ sources only given N sensors [13]-[16]. However, due to the demand to process big data quickly, researchers have turned to underdetermined DOA estimation techniques [1]-[10], [44]-[106]. This is the case as sparse arrays via difference co-array can achieve enhanced degrees of freedom (DOF) by exploiting inherently large interelement spacing to extend the effective array aperture [44]-[72]. Traditional uniform linear arrays (ULAs) have uniformly spaced sensors with the interelement spacing of $d = \lambda/2$ where λ is the wavelength of the source signal's frequency. The sensor spacing of $d = \lambda/2$ is deliberate to avoid grating lobes, which usually appear in the beam pattern of the array when $d > \lambda/2$. Furthermore, the closely spaced sensors consume the already limited mounting platform contributing to low resolution due to the limited aperture. Besides, the closely spaced sensors contribute considerably to mutual coupling between sensors [44]-[76].

On the other hand, sparse or non-uniform linear arrays have different interelement spacing d_s with some $d_s \gg \lambda/2$ [31]. Hence, the overall aperture is considerably large, given the same number of sensors as ULA. Furthermore, by exploiting the difference co-array (DCA), the empty spaces created by the larger d_s are filled by virtual sensors, thereby improving the degrees of freedom [41]-[43]. Besides, the larger interelement spacing reduces the mutual coupling between sensors [96]-[44], [72]. This chapter discusses the concept of difference co-array and related tools for analyzing co-array properties of sparse arrays (linear or planar). Moreover, we review a few selected conventional sparse linear arrays (SLAs) including nested array (NA) [9], minimum redundancy array (MRA) [42], and coprime array (CA) [10], as well as planar arrays including open box array (OBA) [95] and simulated annealing based

planar arrays (SAPSA) [92]-[94].

The remainder of this chapter is outlined as follows. Section 2.2 discusses the co-array signal model and related terminologies necessary to understand sparse linear arrays in view of the DCA concept. The co-array signal model in the presence of the MC effect is discussed in Section 2.2.2. Then, a few selected conventional sparse linear arrays and planar sparse arrays are reviewed in Section 2.3 and 2.4, respectively. Finally, Section 2.5 summarizes the chapter.

2.2 Coarray signal model for DOA estimation

This section introduces a linear array (1D array) signal model followed by a planar array (2D array) signal model. We close the section with array signal model uncertainties, i.e., mutual coupling effect.

2.2.1 Coarray signal model for sparse linear arrays

According to [33]-[34], [36]-[40], vectorizing the \mathbf{R}_{xx} as expressed in (1.3) yields

$$\mathbf{y} = \text{vec}(\mathbf{R}_{xx}) = (\mathbf{B}^* \odot \mathbf{B})\mathbf{p}_c + \sigma_n^2 \mathbf{1}_N, \quad (2.1)$$

where $\mathbf{1}_N = \text{vec}(\mathbf{I}_N)$, and $(\mathbf{B}^* \odot \mathbf{B})$ denotes the extended array manifold due to the difference co-array. The difference co-array is defined as a difference in sensor positions. Formally, the DCA can be expressed as

Definition 2.2.1. The difference co-array \mathbb{D}_c of a physical sparse array \mathbb{S} , is expressed as

$$\mathbb{D}_c = \{n_1 - n_2 | n_1, n_2 \in \mathbb{S}\} \quad (2.2)$$

where $n_1, n_2 \in \mathbb{S}$ denotes the sensor location set [9].

The virtual sensors or distinct elements in the difference co-array are known as lags, i.e.,

Definition 2.2.2. Given the difference co-array \mathbb{D}_c , the number of distinct elements in the difference co-array identifies the number of unique lags provided by \mathbb{D}_c [15].

Besides, the number of unique lags of a sparse linear array identifies with the number of resolvable source signals. Specifically, of interest in the co-array are the lags that form the consecutive central ULA segment \mathbb{U} of the difference co-array because the total number of resolvable sources by any co-array-based estimators is considered to be $(|\mathbb{U}| - 1)/2$ sources [33]-[34], [38]. Thus, the central ULA segment of \mathbb{D}_c can be defined formally as

Definition 2.2.3. The central ULA segment of the difference co-array \mathbb{D}_c of a physical sparse array is expressed as

$$\mathbb{U} = \langle -L_u, L_u \rangle \subseteq \mathbb{D}_c \quad (2.3)$$

and the cardinality of \mathbb{D}_c , \mathbb{U} and L_u are known as the DOF, uniform DOF (uDOF), and one-side uDOF [9], [33]-[34].

However, some autocorrelation values in the difference co-array cannot be computed in certain scenarios, or the lags are missing. In co-array properties, these missing lags are known as “holes”, and can be defined as

Definition 2.2.4. An integer n_i is a hole or a missing lag in difference co-array if $n_i \in \mathbb{D}_c$ but $n \notin \mathbb{U}$. Moreover, the difference co-array is hole-free if $\mathbb{D}_c = \mathbb{U}$ [114].

Typically, (2.1) is used instead of a physical array output (1.2). Therefore, if the sparse linear array is appropriately designed, the size of \mathbb{U} can be larger than the physical array, i.e., $\mathbb{D}_c = \mathcal{O}(|\mathbb{S}|^2)$. Since the total number of resolvable sources by most co-array-based estimators is $(|\mathbb{U}| - 1)/2$ [33], then an optimal sparse array design should maximize uniform DOF while retaining a hole-free DCA. In other words, it should satisfy the $\mathcal{O}(|\mathbb{S}|^2)$ and hole-free properties in order to harness all advantages of the sparse array over ULA [9], [44].

Next, we demonstrate the properties discussed above using three linear arrays. Figure 2.1 (a) depicts the ULA with 10 sensors, i.e., $\mathbb{S}_a = \{0, 1, 2, 3, 4, 5, 6, 7, 8, 9\}$. Obviously, these sensors are equally spaced with a unit spacing. Moreover, Fig. 2.1 (b) and (c) show the SLAs with 10 sensors located at $\mathbb{S}_b = \{0, 1, 2, 4, 5, 7, 11, 12, 13, 14\}$ and $\mathbb{S}_c = \{0, 1, 2, 4, 7, 11, 12, 13, 14, 18\}$, respectively. It can be observed that both sparse arrays have non-uniform interelement spacings. As for the co-array properties,

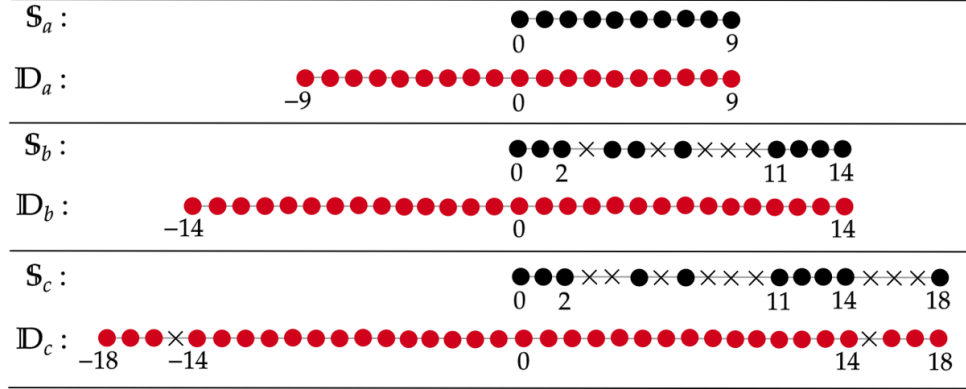


Figure 2.1: The sparse linear arrays are \mathbb{S}_a , \mathbb{S}_b , and \mathbb{S}_c , and their difference co-arrays are \mathbb{D}_a , \mathbb{D}_b , and \mathbb{D}_c , respectively. Here, the \bullet and \times denote a sensor and a blank space, respectively.

\mathbb{S}_a in Fig. 2.1 (a) and \mathbb{S}_b in Fig. 2.1 (b) exhibit complete difference co-array with no missing lags or holes, whereas \mathbb{S}_c in Fig. 2.1 (c) has a hole or a missing lag at position 15 and -15 . In short, \mathbb{S}_a and \mathbb{S}_b show hole-free difference co-array characteristics.

Furthermore, it follows from Fig. 2.1 (a) that the size of the difference co-array of ULA is $|\mathbb{D}_a| = 19$. Thus, the size of the ULA's DCA is almost $2N$, i.e., $|\mathbb{D}_a| = \mathcal{O}(N)$. Note, operator \mathcal{O} stands for the order of function. However, as shown in Fig. 2.1 (b) and (c), the sizes of difference co-arrays of \mathbb{S}_b and \mathbb{S}_c are $|\mathbb{D}_b| = 29$ and $|\mathbb{D}_c| = 29$ in that order.

The DOF ratio is usually used to quantitatively evaluate a sparse linear array's achievable uniform DOF capacity. Below is the formal definition of the DOF ratio.

Definition 2.2.5. Given one-side DOF of a sparse linear array L_u and the number of sensors N . The DOF capacity of a sparse linear array can be expressed as

$$\gamma(N) = \frac{N^2}{L_u(N)} \quad (2.4)$$

Fundamentally, the small $\gamma(N)$ entails higher DOF capacity [41]-[65].

2.2.2 The coarray signal model and mutual coupling effect

In the presence of the mutual coupling effect, which is inevitable in a practical setting, the received signal $\mathbf{x}(t)$ as defined in (1.2), becomes

$$\mathbf{x}(t) = \mathbf{C}\mathbf{B}\mathbf{s}(t) + \mathbf{n}(t), \quad (2.5)$$

where \mathbf{C} is the mutual coupling matrix which can be approximated as a B -banded matrix

$$\mathbf{C} = \begin{cases} c_{|n_1-n_2|}, & |n_1 - n_2| \leq B, \\ 0, & |n_1 - n_2| > B, \end{cases} \quad (2.6)$$

such that $n_1, n_2 \in \mathbb{S}$ and $c_b, b \in [0, B]$ denotes MC coefficients which satisfy $1 = c_0 > |c_1| > |c_2| > \dots > |c_B|$ and $|c_k/c_\ell| = k/\ell$, $k, \ell \in [1, B]$ [8]. Normally, the threshold B is set to 100 [53]-[66].

Typically, in sparse linear arrays, the total mutual coupling effect is evaluated using coupling leakage $L(N)$ [58]-[62] as

$$L(N) = \frac{\|\mathbf{C} - \tilde{\mathbf{C}}\|_F}{\|\mathbf{C}\|_F} \quad (2.7)$$

where

$$\tilde{\mathbf{C}}_{i,j} = \begin{cases} 0 & \text{for } i \neq j \\ \mathbf{C}_{i,j} & \text{for } i = j \end{cases} \quad (2.8)$$

and the $\|\mathbf{C} - \tilde{\mathbf{C}}\|$ is the energy of all off-diagonal elements, which characterizes the amount of mutual coupling effect. Essentially, the smaller the $L(N)$, the lesser the mutual coupling effect [12]. Alternatively, the weight function $w(\ell)$ can be used to quantify the mutual coupling effect. For a sparse linear array, the weight function $w(\ell)$ is defined as follows,

Definition 2.2.6. The weight function $w(\ell)$ is the number of sensor pairs that contribute to the coarray index ℓ , i.e.,

$$w(\ell) = |\{(n_1, n_2) \in \mathbb{S}^2 | n_1 - n_2 = \ell\}|, \quad \ell \in \mathbb{D}_c. \quad (2.9)$$

According to [8]-[10], [13]-[16], weight functions $w(1)$, $w(2)$ and $w(3)$ contribute the most to mutual coupling effect. Hence, reducing the first three weight functions during the sparse array design process is desirable [42]-[72].

2.2.3 Coarray-based direction-of-arrival estimator

As highlighted in Chapter 1, Section 1.2, there are several co-array-based DOA estimation algorithms [32]-[40] which can be applied on (2.1) to estimate sources. However, for brevity's sake, we adopt the spatial smoothing MUSIC (SS-MUSIC) algorithm [33]-[34] as a default DOA estimator throughout this work unless otherwise stated. Having established the default estimator, we briefly discuss the key steps behind the SS-MUSIC algorithm in the subsequent paragraphs.

Starting for the extended signal model in (2.1), we can observe that $(\mathbf{B}^* \odot \mathbf{B})$ embeds a steering vector of an array whose sensor location is given by the difference co-array as defined in (2.3). The virtual ULA can be divided into N_v overlapping uniform subarrays of size $|N_v|$ where the output is given as

$$\mathbf{y}_i = \mathbf{\Gamma}_i \mathbf{y} \quad \text{for } i = 1, 2, \dots, N_v, \quad (2.10)$$

where $\mathbf{\Gamma}_i = [\mathbf{0}_{N_v \times (i-1)} \mathbf{I}_{N_v \times N_v} \mathbf{0}_{N_v \times N_v - i}]$ is the selection matrix for the i -th subarray. Thus, the corresponding covariance matrix for \mathbf{y}_i can be expressed as

$$\mathbf{R}_{\mathbf{y}_i \mathbf{y}_i - 1} = [y_{N_v}, y_{N_v-1}, \dots, y_1], \quad (2.11)$$

or

$$\mathbf{R}_{\mathbf{y}_i \mathbf{y}_i - 2} = \frac{1}{N_v} \sum_{i=1}^{N_v} \mathbf{y}_i \mathbf{y}_i^H. \quad (2.12)$$

The approach in (2.11) is known as the *direct augmentation* method [33]-[34] whilst the one in (2.12) is called *spatial smoothing* method [37]-[39].

Following (2.12), any subspace-based DOA estimation method can be applied to $\mathbf{R}_{\mathbf{y}_i \mathbf{y}_i - 2}$ to estimate DOAs. In our case, we assume the MUSIC algorithm [1]. Essentially, the MUSIC algorithm takes advantage of the orthogonality property to isolate the signal and noise subspaces of $\mathbf{R}_{\mathbf{y}_i \mathbf{y}_i - 2}$. Thus, the Eigen Value Decomposition (EVD) is performed on $\mathbf{R}_{\mathbf{y}_i \mathbf{y}_i - 2}$ to obtain the noise subspace as \mathbf{E}_n which contains

the smallest $N_v - K$ eigenvalues. Then, a peak check function is initiated as

$$P(\theta) = \frac{1}{\mathbf{b}^H(\theta_k) \mathbf{E}_n \mathbf{E}_n^H \mathbf{b}(\theta_k)}, \quad (2.13)$$

where $\mathbf{b}(\theta_k)$ is the virtual ULA steering vector. The result from (2.13) is $(N_v - 1)$ main peaks that correspond to the estimated DOAs. Therefore, the SS-MUSIC algorithm is the combination of (2.12) and (2.13).

2.2.4 Extension to sparse planar arrays

Besides the co-array signal model for sparse linear arrays, let us consider a case of a sparse planar array (also known as a 2-dimensional or a 2D array) with N sensors such that $N = (N_x, N_y)$. In the array, the sensor locations are denoted as nd where $n = (n_x, n_y) \in \mathbb{Z}^2$ is an integer-valued vector, and $d = \lambda/2$ is the minimum interelement spacing between sensors with λ being the wavelength of the source signal's frequency. Assume that K uncorrelated narrowband signals are impinging on the array and the i -th source has a complex amplitude $\mathbf{A}_i \in \mathbb{C}$ with azimuth $\phi_i \in [0^\circ, 360^\circ)$ and elevation $\theta_i \in [0^\circ, 90^\circ)$ components. Thus, the received signal at t -th snapshot can be expressed as

$$\mathbf{x}(t) = \sum_{i=1}^K \mathbf{A}_i(\theta_i, \phi_i) \mathbf{v}(t) + \mathbf{n}(t), \quad (2.14)$$

where $\theta_i = (d/\lambda)\sin\theta_i\cos\phi_i$, $\phi_i = (d/\lambda)\sin\theta_i\sin\phi_i$ and the term \mathbf{v} is the steering vector such that elements associated with sensors at (n_x, n_y) can be expressed as $e^{j2\pi(\theta_i n_x + \phi_i n_y)}$ [48]. And, the covariance matrix of $\mathbf{x}(t)$ can be expressed as

$$\mathbf{R}_{\mathbf{xx}} = E[\mathbf{x}(t)\mathbf{x}^H(t)]. \quad (2.15)$$

Like (2.1), vectorizing (2.15) and cleaning the duplicates yields a difference co-array model of $\mathbf{x}(t)$ as $\mathbf{y}_{\mathcal{Q}}$ which can be further exploited by a DOA estimator instead of (2.14). Here, the DCA $\mathcal{Q} = \{n_1 - n_2 | n_1, n_2 \in \mathbb{S}\}$.

Figure 2.2 shows examples of planar arrays with $N = 9$ sensor (see Fig. 2.2 (a) and (c)), and their corresponding difference co-arrays (see Fig. 2.2 (b) and (d)). Following Fig. 2.2, we highlight the following concerning the DCA properties of the

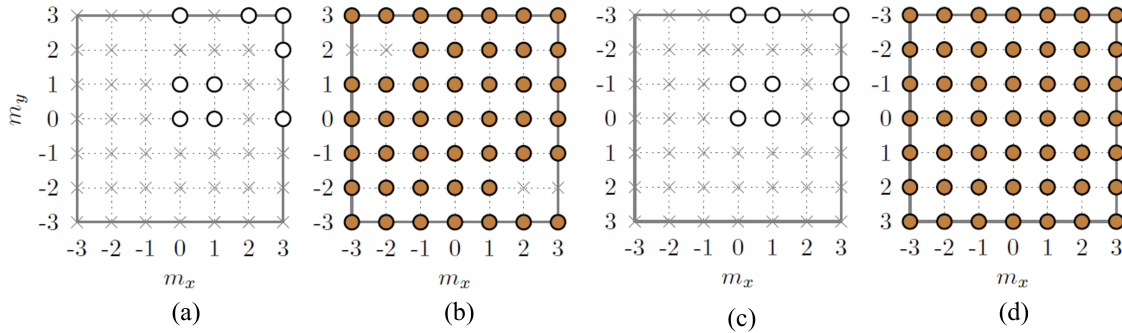


Figure 2.2: Examples of 2D sparse arrays with $N = 9$ and their corresponding difference co-array. Here, (a) shows a 2D sparse array with *holes*, and (b) its corresponding difference co-array, whereas (c) shows a hole-free 2D sparse array, and (d) its corresponding difference coarray. Note, the crosses, circles, and brown circles represent empty spaces, physical sensors, and virtual sensors.

sparse planar arrays:

- a) Similar to SLAs, the missing sensors in the DCA are called *holes* (see the cross in Fig. 2.2 (b) at grid $(2, -2)$). Moreover, the difference co-array with *holes* is termed *non-separable* as most DOA estimators, such as the 2D ESPRIT algorithm, divide the co-array into minor equal square or rectangular subarrays as a decorrelation step [27].
- b) On the other hand, if the DCA of the planar array, as shown in Fig. 2.2 (d), is complete or has no *holes*, the planar array is designated to have a *hole-free* DCA. Consequently, the DCA is termed *separable*, and any off-the-shelf DOA estimator can be applied for DOA estimation purposes [27].
- c) In case the *holes* in (a) are not repairable, a co-array interpolation method can be utilized to fill the holes. Over the decade, a number of co-array interpolation methods via nuclear norm minimization techniques have been widely studied for sparse linear arrays [32], [39], [74]-[75], [77], [79]-[81] and planar arrays [76], [78], [92]-[94].

On a brighter side, it should be noted that the conditions (b)-(c) above are necessary if one is considering a DOA estimation problem involving more sources than the number of sensors ($K > N$), i.e., the *underdetermined case* [33]-[48]. Otherwise,

any DOA estimator can be applied on the consecutive subset of the difference co-array or directly on (2.15) under the assumption that $K \approx (|\mathbb{U}| - 1)/2$ [34].

2.3 Conventional sparse linear arrays

This section reviews a few selected classical sparse linear arrays and their corresponding co-array properties. The SLAs include minimum redundancy array [42], nested array [9], and conventional coprime array [10].

2.3.1 Minimum redundancy array

A minimum redundancy array (MRA) is one of the classic sparse linear arrays proposed in [8], [42]. The MRA minimizes the co-array redundancy \mathbb{R} as

$$\mathbb{R} = \frac{\binom{\mathbb{S}}{2}}{(|\mathbb{U}| - 1)/2}, \quad (2.16)$$

while constraining the difference co-array to be hole-free. In other words, MRA maximizes the consecutive central ULA segment of the difference co-array for a fixed number of sensors [42]. Formally, MRA with N sensors can be expressed as

$$\mathbb{S}_{mra} = \underset{\mathbb{S}}{\operatorname{argmax}} |\mathbb{D}| \quad \text{s.t.} \quad |\mathbb{S}| = N, \mathbb{D} = \mathbb{U}. \quad (2.17)$$

According to [41]-[72], the MRA has the largest hole-free difference coarray for any given number of sensors N . Unfortunately, since MRA is found by solving (2.17), the MRA has no closed-form expression for sensor position, achievable DOF, and weight functions. Hence, MRA has inspired researchers to include closed-form expression for sensor position as one of the key characteristics of a good sparse array design [60]-[72]. Figure 2.3 shows the MRA with 10 sensors, and it follows from Fig. 2.3 that the MRA has a hole-free difference.

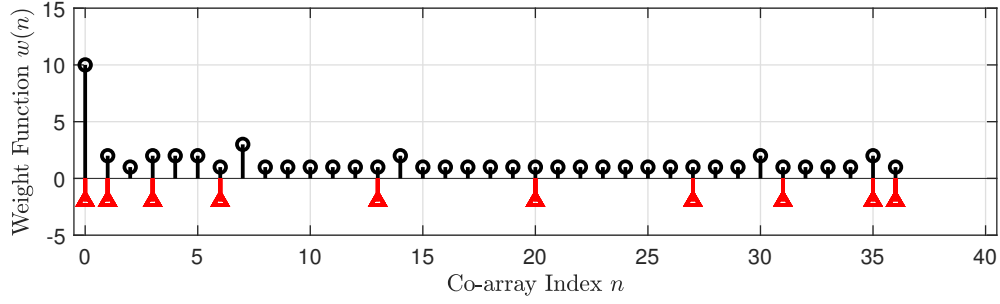


Figure 2.3: The MRA array configuration with $N = 10$ sensors and corresponding coarray weight functions (only positive segment is shown in the view of $w(n) \in [0, 15]$). In the figure, the red stems denote physical sensors.

2.3.2 Nested array

The nested array is one of the common sparse linear arrays, and it consists of two ULAs with different interelement spacing [9]. A dense ULA made up of N_1 sensors with a unit interelement spacing and a sparse ULA comprised of N_2 elements with the interelement spacing of $(N_1 + 1)$ [44]. In short, the NA can be expressed as

$$\mathbb{S}_n = \{1, 2, \dots, N_1, (N_1 + 1), \dots, N_2(N_1 + 1)\}. \quad (2.18)$$

However, the existence of a dense ULA increases the mutual coupling effect in NAs [44], [60]. Figure 2.4 shows the NA configuration with $N = 10$ sensors such that $N_1 = N_2 = 5$. Like MRA, the NA exhibits a hole-free difference apart from the closed-form expression for sensor locations. However, the first three weight functions are high and a bit redundant.

According to [9] the achievable uniform DOF of NA is $\frac{N^2}{2} + N - 1$ given N sensors. Moreover, given parameters $N_1 = \lfloor N/2 \rfloor$ and $N_2 = N - N_1$, the NA has the weight functions $w(1) = N_1$, $w(2) = N_1 - 1$ and $w(3) = N_1 - 2$ which are much higher [9], [44]. As such, several variants of NA have been proposed to reduce the mutual coupling effect and expand the DOF [44]-[45], [48]-[50], [52]-[57], [60].

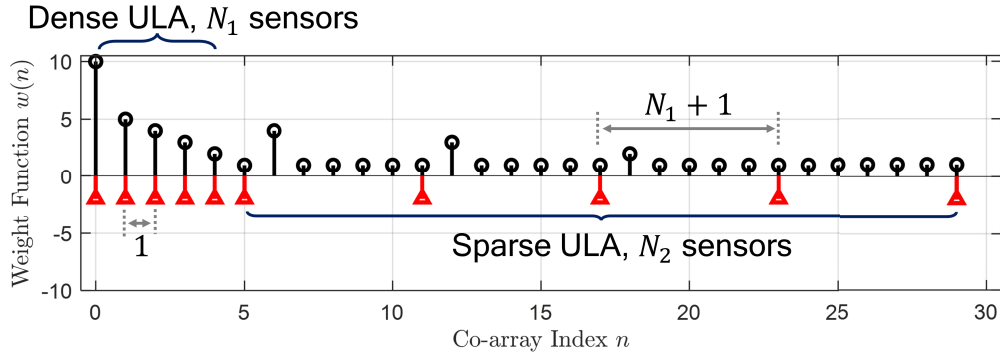


Figure 2.4: The NA array configuration with $N = 10$ sensors ($N_1 = N_2 = 5$) and corresponding coarray weight functions (only positive segment is shown in the view of $w(n) \in [0, 10]$). In the figure, the red stems denote physical sensors.

2.3.3 Coprime array

Unlike NAs, coprime arrays are designed with the reduction of mutual coupling effect as a goal. A coprime array consists of two sparse subarrays with two different coprime interelement spacing. The first subarray is composed of M sensors with N interelement spacing, and the second subarray contains N sensors with M interelement spacing where M and N are coprime integers [10], [16]. The well-known classic coprime array is known as *prototype coprime array* (PCA), and its made up of $M + N - 1$ sensors (as the M sensor subarray and the N sensor subarray shares the zeroth sensor position).

Figure 2.5 shows an example of a prototype coprime array with 12 sensors where $M = 6$ and $N = 7$. Evidently, as shown in Fig. 2.5, the PCA does not have a hole-free difference co-array like NA or MRA. Therefore, the the achievable DOF is based on the extraction of the consecutive section of the difference co-array. For a given optimal M and N , the PCA achieves $2(M + N) - 1$ consecutive lags in the range $[-M - N + 1, M + N - 1]$, as such the PCA is able to resolve up to $\mathcal{O}(MN)$ sources given $M + N - 1$ sensors. However, the PCA has a reduced mutual coupling effect compared to MRA and NA. This can be validated using the weight function of PCA shown in Fig. 2.5. Here, the PCA has $w(1) = w(2) = w(3) = 1$ compared to NA which yields $w(1) = \lfloor N/2 \rfloor$, $w(2) = \lfloor N/2 \rfloor - 1$ and $w(3) = \lfloor N/2 \rfloor - 2$ given the same number of sensors N . Over the decade, several variants of PCA have been

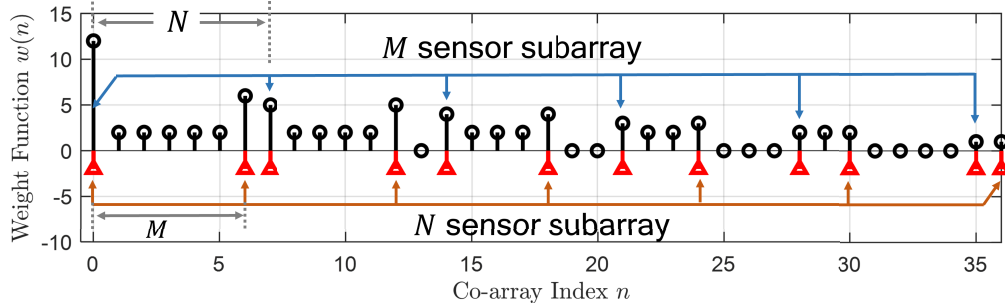


Figure 2.5: The PCA array configuration with $\bar{N} = 12$ sensors ($M = 6, N = 7$) and corresponding coarray weight functions (only positive segment is shown in the view of $w(n) \in [0, 15]$). In the figure, the red stems denote physical sensors.

proposed in [46]-[47], [61]-[63], [68], [70]-[71] by mainly exploiting the redundancy in the difference co-array of the prototype coprime array to improve the size of the achievable DOF.

2.3.4 A note on MRA, NA and PCA array properties

As established in Sections 2.3.1-2.3.3, the achievable uniform DOF and weight function for MRA, NA, and PCA are summarized in Table 2.1. From Table 2.1, three key desirable characteristics of sparse linear array design emerged based on the properties of MRA, NA and PCA as follows:

- a) The sparse linear array should have a closed-form expression for sensor positions from which closed-form expressions of weight functions and achievable degrees of freedom can be derived. For instance, MRA shows attractive properties such as hole-free difference co-array, enhanced DOF, and relatively reduced weight functions. However, the lack of a closed-form expression for the sensor position limits the design process.
- b) The difference co-array of the sparse linear array should retain a hole-free property since most co-array-based DOA estimators utilize the consecutive central segment of a difference co-array, i.e., the central ULA, \mathcal{U} . More importantly, since the number of resolvable sources is $\approx (|\mathcal{U}| - 1)/2$, the existence of the holes in the difference co-array diminishes the size of the usable DOF.

- c) The sparse linear array should retain minimal weight functions, mainly the first three weights, i.e., $w(1)$, $w(2)$ and $w(3)$.

In light of the (a)-(c) characteristics of the sparse linear array highlighted above, our contributions in this thesis center around the design of sparse linear arrays with improved DOF while retaining the three conditions above.

Table 2.1: Comparison of achievable uniform DOF and weight functions of different sparse linear arrays

Array Type	Optimal N_1	Max. uDOF	Weight Functions $w(n)$
Nested Array [9]	$\lfloor N/2 \rfloor$	$N^2/2 + N - 1$	$w(1) = \lfloor N/2 \rfloor - 1$ $w(2) = \lfloor N/2 \rfloor - 2$ $w(3) = \lfloor N/2 \rfloor - 3$
MRA [42]	–	–	–
PCA [10]	$M + N - 1$	$2(M + N) - 1$	$w(1)=1$ $w(2)=1$ $w(3)=1$

2.4 Conventional sparse planar arrays

Following the review of classical sparse linear arrays in Section 2.3, we extended the review to classical sparse planar arrays and their corresponding coarray properties in this section. The idea is to appreciate the use of the co-array properties such as lags, holes or missing lags, hole-free, and difference co-array in the context of high-dimensional arrays. In this section, we consider open box array (OBA) [95] and simulated-annealing-based sparse planar array (SASPA) [92]-[94].

2.4.1 Open box array

The open box array (OBA) is one of the classic 2D sparse arrays known in the array signal processing field. The OBA is developed using three ULA placed orthogonal to

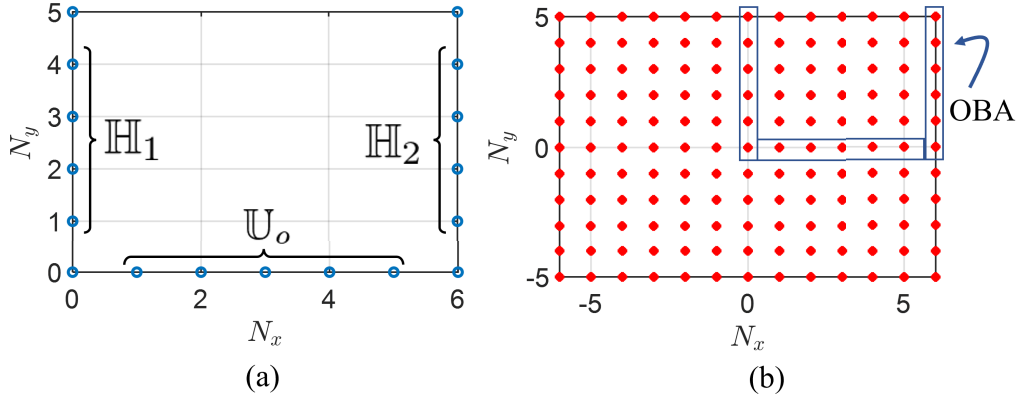


Figure 2.6: (a) The OBA array configuration with $(N_x = 7, N_y = 6)$ and (b) its corresponding difference co-array. Here, the circles, and asterisks represent physical sensors and virtual sensors.

each other such that the three ULA form a rectangle without a fourth edge. Hence, it looks like an open box [95]. Formally, given two integers, N_x and N_y , the OBA sensor positions can be expressed as

$$\mathbb{S}_{oba} = \mathbb{U}_o \cup \mathbb{H}_1 \cup \mathbb{H}_2 \cup \mathbb{C}_o, \quad (2.19)$$

where

$$\begin{cases} \mathbb{U}_o = \{(m_x, 0) | 1 \leq m_x \leq N_x - 2\}, \\ \mathbb{H}_1 = \{(0, m_y) | 1 \leq m_y \leq N_y - 2\}, \\ \mathbb{H}_2 = \{(N_x - 1, m_y) | 1 \leq m_y \leq N_y - 2\}, \\ \mathbb{C}_o = \{(0, 0), (N_x - 1, 0), (0, N_y - 1), (N_x - 1, N_y - 1)\}, \end{cases} \quad (2.20)$$

and the total number of sensors $N = 2N_y + N_x - 2$. Figure 2.6 (a) shows the array configuration of OBA with $N = 17, N_x = 7$ and $N_y = 6$, where \mathbb{H}_1 , \mathbb{U}_o and \mathbb{H}_2 denote the left ULA, the bottom ULA, and the right ULA, respectively. The corner sensors are represented by \mathbb{C}_o . As shown in Fig. 2.6 (b), OBA has a hole-free difference co-array. Mathematically, the difference co-array of OBA can be expressed as

$$\mathbb{D}_{oba} = \{(m_x, m_y) \in \mathbb{Z}^2 | -N_x + 1 \leq m_x \leq N_x + 1, \\ -N_y + 1 \leq m_y \leq N_y + 1\}. \quad (2.21)$$

Besides the co-array, as observed in Fig. 2.6 (a), the sensor pairs with a sensor separation of 1 are high due to the use of ULA. As a result, the mutual coupling effect is severe. To alleviate the mutual coupling effect, several 2D sparse arrays have been developed over the years based on the basic array structure of OBA [91]-[95], [99].

2.4.2 SA-based sparse planar arrays

In [91]-[94], a simulated annealing-based planar array (SAPSA) was investigated with the aim of reducing the mutual coupling in an hourglass array (HA) [95]. Starting with the hourglass array with N sensors as an initial sparse array, i.e., \mathbb{S}_i , the SAPSA can be realized by solving the following problem

$$\begin{aligned} \mathbb{S}_{sa} = \operatorname{argmax}_{\mathbb{S}_i} & \sum_{i=1}^N \sum_{j=i+1}^N \frac{1}{\|n_i - n_j\|_2}, \\ \text{s.t.} & \|n_i - n_j\|_2 \leq B, \end{aligned} \quad (2.22)$$

where $n_{i,j} \in \mathbb{S}_i$, N is the number of sensors and $\|\cdot\|_2$ is the l_2 -norm of a vector. The problem in (2.22) aims at optimizing the sensor positions in \mathbb{S}_i while minimizing the mutual coupling between sensors, i.e., $\sum_{i=1}^N \sum_{j=i+1}^N \frac{1}{\|n_i - n_j\|_2}$.

In [92], the simulated annealing algorithm was utilized to solve (2.22) where the sensor in \mathbb{S}_i are perturbed until the algorithm converges to a local minimum. Figure 2.7 shows an example of the SAPSA array with $N = 16$ sensors and its corresponding difference co-array. It can be observed in Fig. 2.7 (a) that the SAPSA has fewer sensor pairs with the interelement spacing of 1, hence, reduced mutual coupling effect. However, such a reduced mutual coupling effect is achieved at the cost of incomplete difference co-array (see Fig. 2.7 (b)). Despite having reduced mutual coupling, the SAPSA is not unique, it is algorithm dependent, and each run generates a different random sparse array [91]-[94].

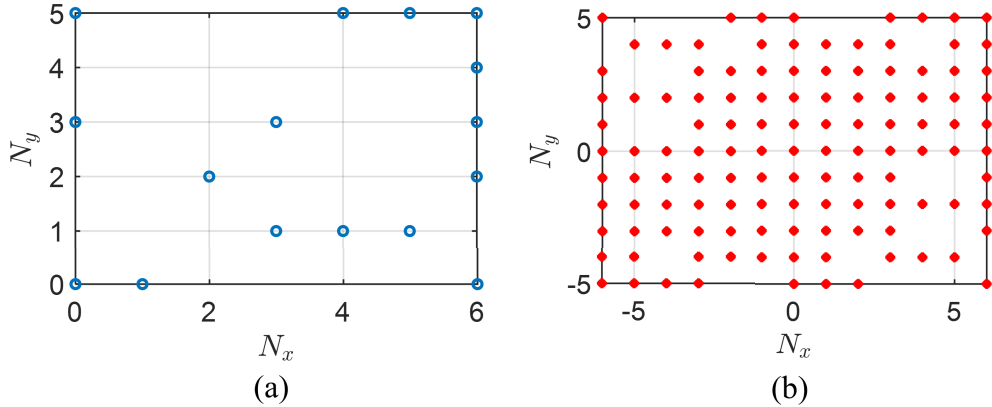


Figure 2.7: (a) The SAPSA array configuration with $(N_x = 7, N_y = 6)$ and (b) its corresponding difference co-array. Here, the circles, and asterisks represent physical sensors and virtual sensors.

2.5 Chapter summary

In this chapter, we briefly introduced preliminaries to sparse signal processing and sparse array designs. Specifically, in light of the difference co-array concept, we review co-array signal models for DOA estimation as applied in both sparse linear and planar arrays. Besides, the chapter also discussed critical co-array-related terminologies such as uniform degrees of freedom, degree of freedom ratio, and coupling leakage that are essential for the evaluation of sparse array designs for DOA estimation.

Furthermore, the chapter discussed a selected few sparse array configurations (linear and planar) as a foundation for our proposed work in Chapters 3-6. Among other key properties, coupling leakage ($L(N)$) and degrees of freedom ratio ($\gamma(N)$) emerged to be the two critical parameters with a trade-off. Hence, an optimal sparse array should be able to balance this trade-off besides retaining the closed-form expression for sensor locations. Our contributions, as we shall see in Chapters 3-6, focus on improving the DOF while retaining the hole-free difference coarray and closed-form expression for sensor positions [9], [42], [51]-[54]. As such, the reduced mutual coupling effect is a by-product, like the case of the MISC array.

A Nested Array Geometry with Enhanced Degrees of Freedom and Hole-Free Difference Coarray

3.1 Introduction

Direction-of-Arrival (DOA) estimation is one of the valuable techniques in array signal processing for detection and localization of array input signals [13]–[14]. Hence, it has many applications in sonar, automotive radar, imaging, and wireless communication systems [15], [42]. Traditional methods commonly use uniform linear arrays (ULAs), where the sensors are placed at a half-wavelength ($\lambda/2$) from each other to avoid spatial aliasing [14]. However, ULA can resolve up to $N - 1$ sources given N sensors. Besides, the closely $\lambda/2$ spaced elements in ULA contribute considerably to mutual coupling between sensors [42]–[60]. Recently, sparse linear arrays (SLAs) have become more attractive than traditional ULA for several reasons. Firstly, given the difference co-array (DCA) concept, the SLAs can attain $\mathcal{O}(N^2)$ degrees of freedom (DOF) which enables the SLAs to resolve more sources than the number of sensors [9]. Secondly, the large interelement spacing between the sparse array’s sensors alleviates the mutual coupling more effectively [9], [42]–[51]¹.

Typical sparse linear arrays include minimum redundancy array (MRA) [42], minimum hole array (MHA) [43], coprime array (CA) [10], and nested linear array (NA) [9]. Despite having good co-array and mutual coupling characteristics, the above sparse linear arrays have limitations: i) the MRA and MHA lack closed-form expressions for sensor locations [10], [44]–[53]; ii) the CAs have holes in their difference co-array. Therefore, the realized DOF is lower than those of the MRA, MHA, and NA [9]; iii) the NA exhibits a severe mutual coupling effect due to the existence of a dense section with closely spaced sensors [44], [72]. Following these limitations, several modified NAs and CAs have been developed targeting either a)

¹This chapter is based on S. Wandale and K. Ichige, “A Nested Array Geometry with Enhanced Degrees of Freedom and Hole-Free Difference Coarray,” *2021 29th European Signal Processing Conference (EUSIPCO)*, Dublin, Ireland, 2021, pp. 1905-1909, doi: [10.23919/EUSIPCO54536.2021.9616342](https://doi.org/10.23919/EUSIPCO54536.2021.9616342).

improved DOF, b) reduced mutual coupling, or c) both [44]-[53].

Specifically, to reduce the mutual coupling effect, sparse linear arrays such as the super nested array (SNA) [44], [72], the generalized nested array (GNA) [45], the generalized coprime array (GCA) [46], the thinned coprime array (TCA) [47], have been proposed. On the other hand, the augmented nested array (ANA) [48], the enhanced nested array (ENA) [49], the improved nested array (INA) [50], the Iizuka NA (IINA) [52], the sparse array with maximum inter-element spacing constraint (MISC) [51] and one/two-sides extended nested array (OS/TS-ENA) [53] have been proposed to enhance the DOF. Nonetheless, these modified arrays retain some of the limitations of their parent arrays, NA and CA. Variants like super nested arrays achieved reduced mutual coupling at the cost of constant DOF, i.e., the SNA retains the same DOF as the NA, the parent array [44]. Furthermore, Iizuka nested array and improved nested array still have the original NA's dense section with closely spaced sensors, hence, suffer severe mutual coupling effect. Besides, the difference coarray of the generalized coprime array, the generalized nested array, and the thinned coprime array are not complete or hole-free (the co-arrays contain missing virtual sensors or holes). As a result, their achievable DOFs are still limited compared to their parent arrays, CA and NA [48], [54]. Therefore, there is still potential for further extension of these classical sparse arrays.

This chapter proposes an enhanced nested array with multiple subarrays (ENAMS). The ENAMS array is designed by splitting the nested array into several sparse subarrays with different sensor separations. The sparse sensor separation enables ENAMS to possess enhanced DOF and reduced mutual coupling compared to NA, ENA, and INA, given the same number of sensors. More importantly, the ENAMS array enjoys all the desired properties of NA, including closed-form expression for sensor locations, a hole-free difference coarray, and a relatively reduced MC effect. Numerical simulations and theoretical analysis are used to demonstrate the superiority of the proposed sparse linear array. The results show that the proposed ENAMS array performs better than other sparse arrays.

The remaining sections are organized as follows. Section 3.2 reviews the NA and ENA array structures and their coarray properties as a basis for the proposed ENAMS array. The ENAMS array is introduced in Section 3.3, and some basic

properties are provided. Furthermore, a closed-form expression for achievable DOF and the weight functions are derived in detail. Numerical examples in Section 3.4 validate the enhanced DOF and high-resolution DOA estimation performance of the proposed ENAMS array. Lastly, Section 3.5 concludes this chapter.

3.2 Conventional sparse linear arrays

In this section, we review conventional sparse linear arrays, specifically the NA [9] and ENA [49]. We uncover a two-dimensional (2D) representation approach of a one-dimensional (1D) sparse linear array from these two conventional arrays. Thus, this chapter uses the 2D representation approach to design our proposed ENAMS array.

3.2.1 1D representation of NA and extended NA

The conventional NA consists of two distinct subarrays with two different interelement spacing—a dense ULA with N_1 -sensors and $\lambda/2$ interelement spacing, and a sparse ULA with N_2 -sensors and $\lambda/2(N_1 + 1)$ interelement spacing (henceforth, $\lambda/2$ is normalized to 1 for simplicity) [9]. Formally, the NA is defined as

$$\mathbb{S}_{na} = \{i_1 | 1 \leq i_1 \leq N_1\} \cup \{(N_1 + 1)i_2 | 1 \leq i_2 \leq N_2\}, \quad (3.1)$$

where $N_1 = \lfloor N/2 \rfloor$ and $N_2 = N - N_1$ for $N \geq 6$. Besides the closed-form expression for sensor locations, the NA retains a hole-free difference co-array, i.e., $\mathcal{O}(N^2)$ DOF. However, the dense ULA of NA is highly redundant, and the closely spaced sensors contribute to severe mutual coupling effects. As a result, several variants of NA have proposed to either alleviate the mutual coupling effect or improve the DOF of NA [44]-[53]. Among all variants of NA, the ENA [53] is of interest in this chapter.

The ENA array was designed by extending NA via two operations. Firstly, the gap of length $(N_1 + 1)$ is introduced between the dense ULA and sparse ULA of the NA instead a unit spacing as seen in (3.1). Then, the interelement spacing of sensors in the sparse ULA is reduced to N_1 from $(N_1 + 1)$ as used in (3.1). Thus, these two operations extended the overall aperture of the NA by 1. Essentially, the ENA can

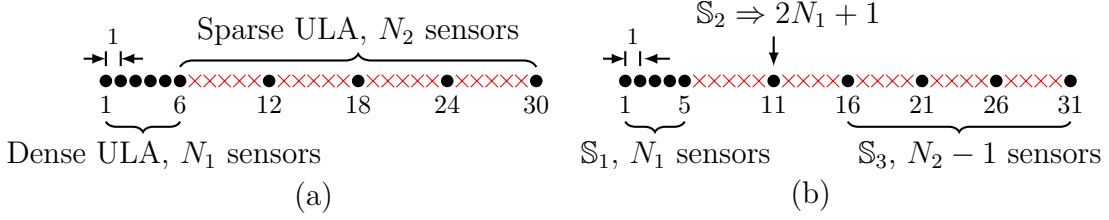


Figure 3.1: Comparison of sparse linear array configurations. Here, (a) NA with $N_1 = N_2 = 5$ and $N = 10$, and (b) ENA array with $N_1 = N_2 = 5$ and $N = 10$. The bullets denote physical sensors, and empty spaces stand for crosses.

be expressed as

$$\mathbb{S}_{ena} = \{(N_1 + 1) - i_1 | i_1 \in [1, N_1]\} \cup (2N_1 + 1) \cup \{(i_2 + 2)N_1 + 1 | i_2 \in [1, N_2 - 1]\}, \quad (3.2)$$

where $N_1 = \lfloor N/2 \rfloor$ and $N_2 = N - N_1$ for $N \geq 6$ [53]. Figure 3.1 compares the sparse array configurations of the NA and ENA with $N = 10$ sensors. Obviously, from Fig. 3.1, the ENA (Fig. 3.1 (a)) has an extended aperture compared to NA (Fig. 3.1 (b)). It can be observed that the sparse ULA begins from $2N_1 + 1$ instead of $N_1 + 1$, which is $N_1 + 1$ than in NA. Furthermore, like NA, the ENA retains a hole-free difference co-array.

3.2.2 2D representation of NA and extended NA

To understand the connection between the NA and ENA as defined in Section 3.2.1, we adopt a 2D representation approach of a 1D sparse linear array as suggested in [44], [72]. Note that this does not mean converting a 1D sparse linear array to a 2D sparse array but instead presenting the interelement spacing pattern of a 1D array in a vertically stacked format such that it looks like a 2D sparse array.

Beginning with the NA with $N = 10$ sensors, as shown in Fig. 3.2 (a), the distance between the 1st and the 2nd sensor in the sparse ULA of the NA is $(N_1 + 1)$, and a quick analysis of the whole NA array structure indicates that the NA can be divided into N_2 section of length $(N_1 + 1)$ [44]. The first $(N_1 + 1)$ section, subsequently, the $\ell - 1$ layer, consists of N_1 sensors from the dense ULA and the 1st sensor of the sparse ULA. Then, starting with the $\ell - 1$ layer and stacking the subsequent $N_2 - 1$

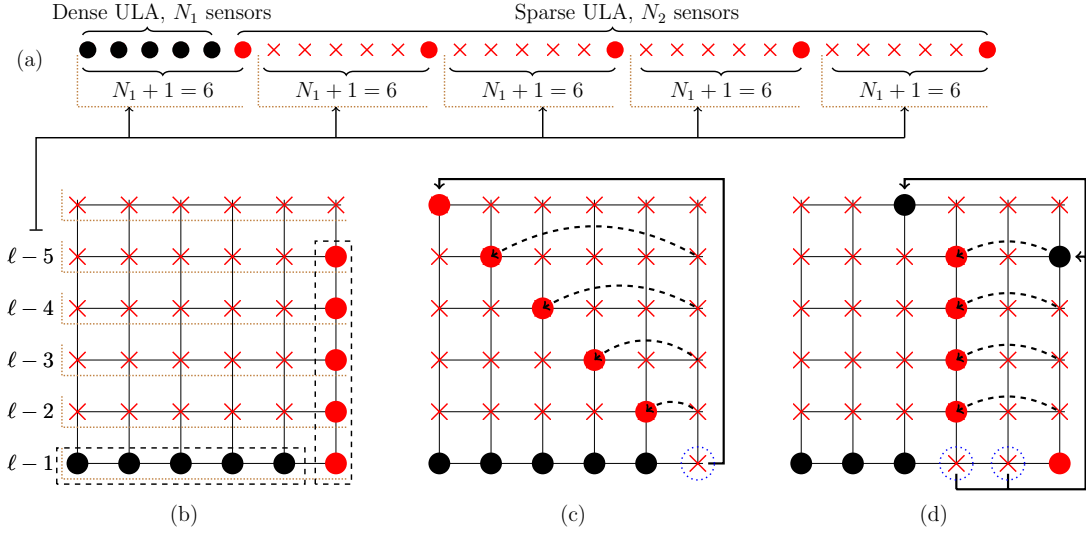


Figure 3.2: The 2D representation of 1D sparse linear array configurations with $N_1 = N_2 = 5$ and $N = 10$ sensors. Here, (a) 1D representation of NA, (b) 2D representation of NA, (c) 2D representation of ENA, and (d) 2D representation of ENAMS array. Note the bullets denote physical sensors, and empty spaces stand for crosses. Notations: i) black bullets (dense ULA sensors), ii) red bullets (sparse ULA sensors), and iii) blue dotted circles (relocated sensors).

sections on top of it, forms a 2D structure as a 2D representation of the NA as shown in Fig. 3.2 (b).

Similarly, by using the same criterion of length $(N_1 + 1)$ and dividing the ENA as shown in Fig 3.1 (b) into segments of length $(N_1 + 1)$, we can generate a 2D representation of the ENA as shown in Fig. 3.2 (b) by stacking the segments together. A closer look at Fig. 3.2 (b) suggests that the ENA is realized by relocating the sensors from the far-right column into the diagonal of the square grid. And to complete the diagonal, a sensor is relocated from $(N_1 + 1)$ to $N_2(N_1 + 1) + 1$, thereby increasing the aperture of NA by 1 [Proposition 2, 53] given any number of sensors N provided that $N_1 = \lfloor N/2 \rfloor$ and $N_2 = N - N_1$.

3.3 The proposed ENAMS array design

The 2D representation depicted in Fig. 3.2 (b)-(c) indicates that there are many possibilities for extending the NA, and one such extension is the proposed ENAMS

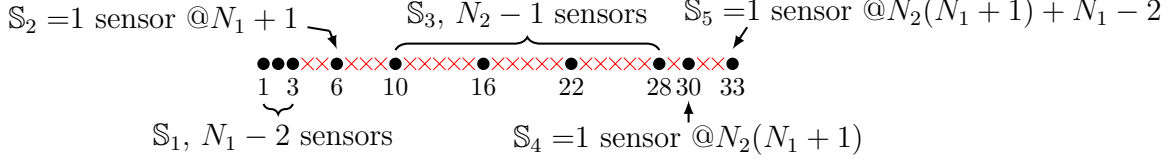


Figure 3.3: The sparse linear array configurations of ENAMS array with $N_1 = N_2 = 5$ and $N = 10$ sensors. The bullets denote physical sensors, and empty spaces stand for crosses.

array. These possible extensions can be achieved by relocating sensors from i) the bottom first row, ii) the far-right column of the 2D representation of the NA, or iii) both. To improve the DOF of the ENA further, the ENAMS array is designed by relocating the sparse ULA sensors from the far-right column to the N_1 th column except for the first sensor located at $N_1 + 1$. Then, two sensors at locations $N_1 - 1$ and N_1 are relocated to locations $N_2(N_1 + 1)$ and $N_2(N_1 + 1) + N_1 - 2$, respectively (see Fig. 3.2 (d)). Thus, the proposed ENAMS array can be defined as

$$\mathbb{S}_{enam} = \mathbb{S}_1 \cup \mathbb{S}_2 \cup \mathbb{S}_3 \cup \mathbb{S}_4 \cup \mathbb{S}_5, \quad (3.3)$$

where

$$\begin{aligned} \mathbb{S}_1 &= \{\ell_1 | 1 \leq \ell_1 \leq N_1 - 2\}, \\ \mathbb{S}_2 &= N_1 + 1, \\ \mathbb{S}_3 &= \{2N_1 + \ell_2(N_1 + 1) | 0 \leq \ell_2 \leq N_2 - 2\}, \\ \mathbb{S}_4 &= N_2(N_1 + 1), \\ \mathbb{S}_5 &= N_2(N_1 + 1) + N_1 - 2, \end{aligned}$$

where $N_1 = \lfloor N/2 \rfloor$ and $N_2 = N - N_1$ for $N \geq 6$ [54]. Figure 3.3 shows the ENAMS array configuration with $N = 10$ sensors. Compared to NA and ENA (Fig. 3.1 (a)-(b), respectively), the proposed ENAMS array offers an improved aperture than NA and ENA. Besides, the ENAMS array retains a hole-free difference co-array, as formally summarized in Lemma 3.3.1 below.

Lemma 3.3.1. *Given $N_1 = \lfloor N/2 \rfloor$, $N_2 = N - N_1$ and $N \geq 6$, the difference co-array of ENAMS array is hole-free ULA, i.e., $\mathbb{D} = [-L_u, L_u]$ such that $L_u = N_2(N_1 + 1) + N_1 - 3$.*

Proof. Refer to Appendix 8.2 □

Property 3.3.2. Given $N_1 = \lfloor N/2 \rfloor$, $N_2 = N - N_1$ and $N \geq 6$, the achievable uniform DOF of the ENAMS array is $\frac{N^2}{2} + 2N - 5$.

Proof. According to (5.5) and Lemma 3.3.1, the uniform DOF of the ENAMS array is

$$uDOF = 2L_u + 1 = 2N_2(N_1 + 1) + 2N_2 - 5. \quad (3.4)$$

Assuming $N_1 = \lfloor N/2 \rfloor \approx (N/2)$ and $N_2 = N - N_1$, and substituting them into (3.4) yields

$$uDOF = \frac{N^2}{2} + 2N - 5, \quad (3.5)$$

and, therefore, completes the proof. □

Property 3.3.3. Given $N_1 = \lfloor N/2 \rfloor$, $N_2 = N - N_1$ and $N \geq 10$, the ENAMS array satisfies the following first three weight functions: $w(1) = N_1 - 3$, $w(2) = N_1 - 3$ and $w(3) = N_1 - 4$.

Proof. See Appendix 8.2 □

According to Property 3.3.3, the first three weight functions of the proposed ENAMS array are less than those of the NA [9]

$$w(1) = N_1, w(2) = N_1 - 1, \text{ and } w(3) = N_1 - 2, \quad (3.6)$$

and those of the ENA array [53]

$$w(1) = N_1 - 1, w(2) = N_1 - 2, \text{ and } w(3) = N_1 - 3. \quad (3.7)$$

This is due to the fact that the weights $w(1)$, $w(2)$, and $w(3)$ contribute largely to mutual coupling effects. As a result, the robustness of a sparse array to the mutual coupling effect can be judged based on the value of these weight functions. The smaller the values of these weight functions, the lower the mutual coupling effect and vice versa [44].

3.4 Numerical examples

In this section, we examine the performance of the proposed ENAMS array in terms of i) weight functions, ii) achievable DOF, iii) MUSIC spectra [33], and iv) root-mean-square-error (RMSE) of DOA estimates. For comparison purposes, the following sparse arrays are considered: NA, ENA, and MRA. The RMSE averaged over \mathcal{J} trials is expressed as

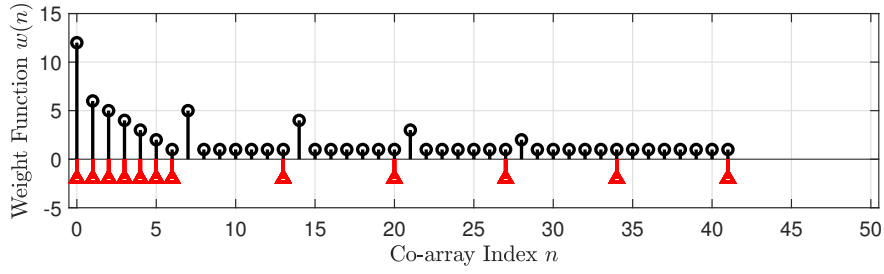
$$RMSE = \sqrt{\frac{1}{\mathcal{J}K} \sum_{j=1}^{\mathcal{J}} \sum_{k=1}^K (\tilde{\theta}_k^j - \bar{\theta}_k)^2}, \quad (3.8)$$

where $\tilde{\theta}_k^i$ denotes i -th estimated normalized DOA for i -th trial and $\bar{\theta}_k$ is the true normalized DOA.

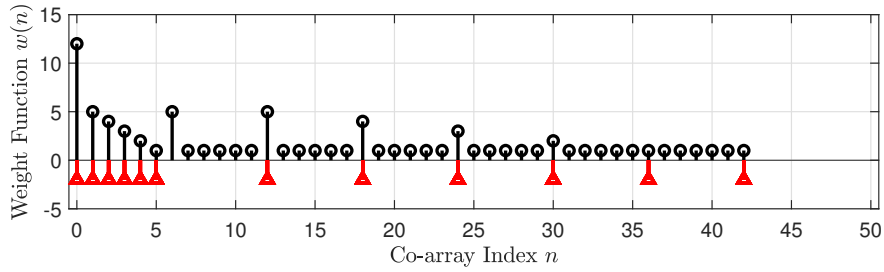
3.4.1 Co-array, weight functions, and achievable DOF

In this subsection, we evaluate the co-array properties and weight functions of the proposed ENAMS array against other existing sparse arrays. Figure 3.4 shows the sensor placement of various sparse arrays and their corresponding weight functions. As shown in Fig. 3.4, all sparse arrays retain a hole-free difference coarray, and the ENAMS array has a larger aperture than the NA and the ENA array. This observation agrees with Lemma 3.3.1 and Property 3.3.2. Moreover, the ENAMS array has weight functions $w(1) = 4$, $w(2) = 4$ and $w(3) = 3$ which validates Property 3.3.3. Compared to weights of the NA ($w(1) = 6$, $w(2) = 5$ and $w(3) = 4$), and the ENA ($w(1) = 5$, $w(2) = 4$ and $w(3) = 3$), the ENAMS array possesses small weights than the NA besides the enhanced DOF. However, the weights are still high than those of the MRA ($w(1) = 2$, $w(2) = 1$, and $w(3) = 2$).

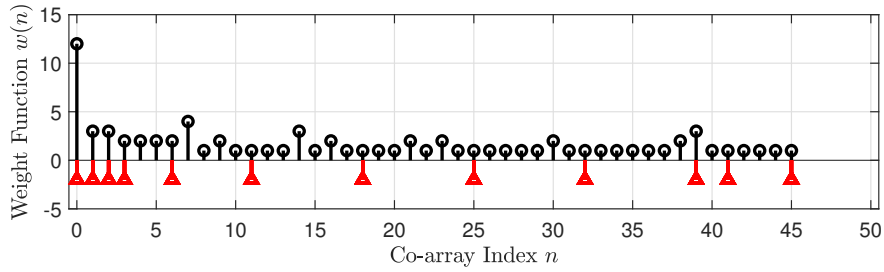
Next, we compare the closed-form expressions of achievable DOF of difference sparse linear arrays versus the number of sensor N . The achievable DOF of the NA, ENA, and ENAMS array are summarized in Table 3.1. Note that according to our knowledge, the closed-form expression for achievable DOF of the MRA does not exist [42], [44], hence, omitted in Table 3.1. As shown in Table 3.1, the ENAMS array attains high DOF than other sparse arrays given the same number of sensors N .



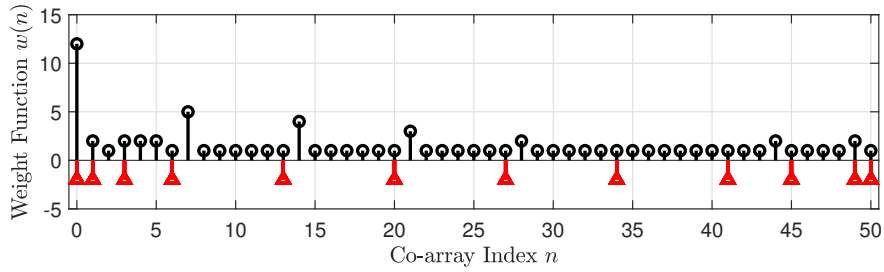
(a) NA with $N_1 = 6, N_2 = 6$ and $N = 12$ sensors.



(b) ENA with $N_1 = 6, N_2 = 6$ and $N = 12$ sensors.



(c) ENAMS array $N_1 = 6, N_2 = 6$ and $N = 12$ sensors.



(d) MRA array with $N = 12$ sensors.

Figure 3.4: Comparison of sparse linear array configurations and their corresponding coarray weight functions (only positive segment is shown in the view of $w(n) \in [0, 15]$).

Table 3.1: Comparison of achievable DOF of various sparse arrays

Array Type	Optimal, N_1	Achievable uDOF
NA	$\lfloor N/2 \rfloor$	$N^2/2 + N - 1$
ENA	$\lfloor N/2 \rfloor$	$N^2/2 + N + 1$
ENAMS	$\lfloor N/2 \rfloor$	$N^2/2 + 2N - 5$
MRA	—	—

3.4.2 MUSIC spectra of DOA estimation

In this example, we compare the MUSIC spectra $P(\bar{\theta})$ of DOA estimation of different sparse array configurations. Here, we consider SNR = 0 dB SNR, 500 snapshots and $K = 25$ uncorrelated sources, located at $\bar{\theta}_k = -0.2 + 0.5(k - 1)/24$ for $k \in [1, 25]$. Since all sparse arrays consist of $N = 12$, this is an underdetermined case where there are more sources than the number of sensors. Figure 3.5 depicts the SS-MUSIC spectra of different sparse linear arrays. As shown in Fig 3.5, the MRA and the proposed ENAMS were able to resolve all sources successfully. However, the NA and the ENA resolved some of the sources correctly. Besides, the SS-MUSIC spectra of the NA and the ENA exhibit spurious peaks, which can be attributed to the limited array aperture or DOF.

3.4.3 RMSE of DOA estimation

Lastly, we evaluate the performance of the arrays quantitatively using the root-mean-square-error (RMSE) of DOA estimation. The RMSE is expressed as in (3.8). First, we consider RMSE versus input SNR where the number of snapshots is 500, $K = 26$ located at $\bar{\theta}_k = -0.2 + 0.5(k - 1)/25$ for $k \in [1, 26]$ and $N = 16$. The SNR varies from -30 to 10 dB. Figure 3.6 (a) shows the plot of RMSE versus input SNR for different sparse arrays. As shown in Fig 3.6 (a), the proposed ENAMS array outperforms other sparse arrays except for MRA, mainly due to its large aperture.

Secondly, we examine the RMSE versus the number of snapshots for NA, ENA,

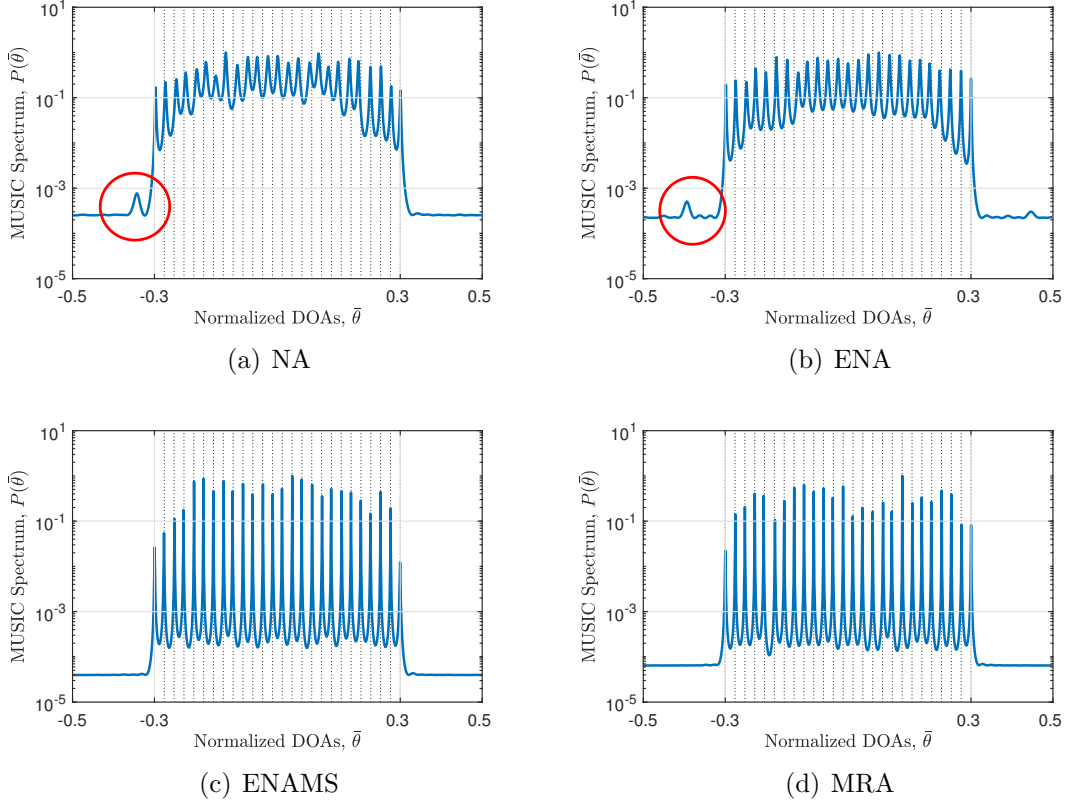


Figure 3.5: The SS-MUSIC spectra $P(\bar{\theta})$ for the NA, ENA, ENAMS and MRA when $N = 12$ and $K = 26$ normalized sources distributed in the range $-0.3 \leq \bar{\theta} \leq 0.3$. The SNR is 0 dB, while the number of snapshots is 500. The dotted lines on the x-axis denote the true DOAs.

ENAMS, and MRA. In this example, the SNR is 0 dB, $K = 26$ evenly located at $\bar{\theta}_k = -0.2 + 0.5(k-1)/25$ for $k \in [1, 26]$ and $N = 16$. Here, the number of snapshots varies from 100 to 1000. Figure 3.6 (b) depicts the plot of RMSE versus the number of snapshots for various sparse arrays. From Fig. 3.6 (b), it is evident that the ENAMS array performs better than NA and ENA but slightly lower than MRA.

Assuming the mutual coupling scenario, we consider examining the RMSE versus $|c_1|$ where SNR is 0 dB, the number of snapshots is 500, $K = 26$ evenly located at $\bar{\theta}_k = -0.2 + 0.5(k-1)/25$ for $k \in [1, 26]$, $N = 16$, and the mutual coupling parameters as $B = 100$ and $c_l = c_1 e^{j\pi(l-1)/8}/l$ for $l \in [1, B]$. This experiment aims to assess the robustness of various sparse arrays at different levels of mutual coupling effect. With

all parameters constant, we vary the coupling factor $|c_1|$ from 0 to 0.6. The plot of the RMSE versus $|c_1|$ for various sparse arrays is shown in Fig. 3.7 (a). As shown in Fig. 3.7 (a), the ENAMS is robust to the mutual coupling effect when $|c_1| < 0.18$ and degrades as $|c_1|$ increases. However, NA and ENA performance suffers within the same $|c_1|$ region.

Lastly, we evaluate the impact of the number of sources K on the RMSE performance of various sparse arrays. In this experiment, SNR is fixed at 0 dB, the number of snapshots is 500, and $N = 16$. The number of sources K varies from 10 to 50, all distributed in the range $\bar{\theta}_k = -0.3 + 0.6(k - 1)/(K - 1)$ for $k \in [1, K]$. Figure 3.7 (b) shows the plot of RMSE versus the number of sources for various sparse arrays. Notably, the RMSE performance degrades for all sparse arrays as the number of sensors increases. However, the ENAMS performs well than the NA and the ENA, except for MRA. Although MRA outperforms the ENAMS array, Fig. 3.7 (b) demonstrates the superiority of the proposed ENAMS array compared to its parent arrays, the NA and the ENA.

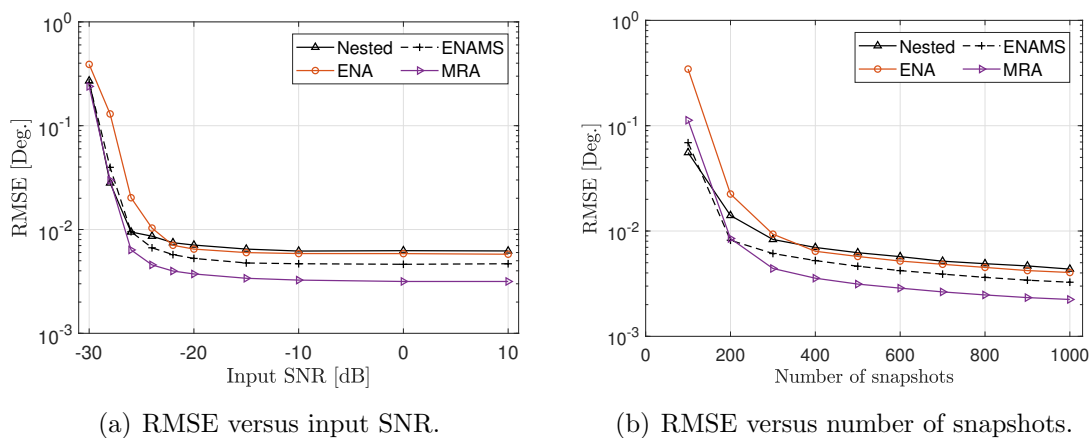


Figure 3.6: RMSE of DOA estimation performance for different sparse linear arrays where (a) SNR= $-30 \sim 10$ dB with 500 snapshots and (b) $100 \sim 1000$ snapshots with 0 dB SNR.

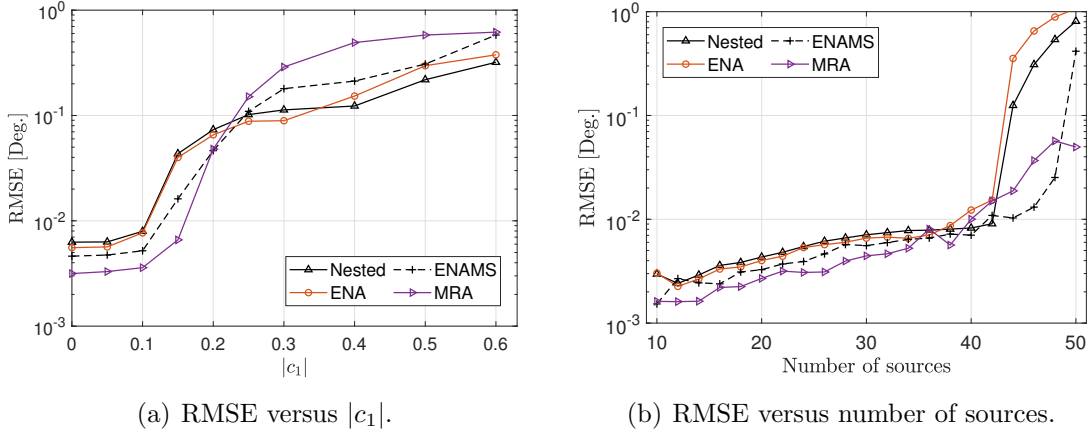


Figure 3.7: RMSE of DOA estimation performance for different sparse linear arrays where (a) $|c_1| = 0 \sim 0.6$ with 0 dB SNR, 500 snapshots and (b) $K = 10 \sim 50$ with 0 dB SNR, 500 snapshots.

3.5 Chapter summary

This chapter introduced a new extended nested array geometry with multiple subarrays (ENAMS) that provide enhanced DOF and a hole-free difference coarray. Using a 2D representation of a 1D sparse linear array approach, the ENAMS array is designed by relocating two sensors from the dense ULA of the NA and a sensor from the sparse ULA of the NA. The relocated three sensors are strategically allocated to the locations at begin of the sparse ULA and at the end of the same sparse ULA, thereby enhancing the overall aperture. Numerical examples demonstrate that the realized sparse array provides high-resolution DOA estimation compared to the conventional NA and other well-known sparse arrays.

Although the ENAMS array has demonstrated enhanced DOF and reduced weight functions, the ENAMS array is still limited in terms of achievable DOF and reduced mutual coupling compared to the state-of-the-art sparse linear array such as one/two sides extended nested array (OS/TS-ENA) [53], improved NA (INA) and sparse array via maximum interelement spacing (MISC). As a result, in the subsequent Chapters, we explore more advanced methods of extending the ENAMS array further and develop better sparse linear array configurations.

Flexible Extended Nested Array with Multiple Subarrays Achieving Improved Degrees of Freedom

4.1 Introduction

Over the decade, several modified nested arrays and coprime arrays have been proposed to enhance the degrees of freedom and reduce the mutual coupling effect [8]-[10], [44]-[72]. The well-known variants include the super nested array (SNA) [44], [72], generalized nested array (GNA) [45], generalized coprime array (GCA) [46], thinned coprime array (TCA) [47], augmented nested array (ANA) [48], enhanced nested array (ENA) [49], improved nested array (INA) [50], Iizuka NA [52], sparse array via maximum interelement spacing constraint (MISC) [51] and one/two-side extended nested array (OS/TS-ENA) [53]. Even so, some of them are not optimal. For instance, the SNA shares the same DOF with the parent NAs. Besides, the INA and ENA still retain the dense subarray of prototype NA, hence, suffer severe mutual coupling effect. Moreover, the DCAs of GCA and GNA are not hole-free. Therefore, their resulting degrees of freedom (DOF) are much more limited as compared to those of NA and CA¹.

In Chapter 3, we introduced an extended nested array with multiple subarrays (ENAMS) as an extension of NA. The ENAMS array is formed by relocating sensors from the dense and sparse subarrays of the NA to the far right side of it, thereby improving the overall DOF. Although ENAMS retains all the good properties of NA apart from enhanced DOF, the realized DOF is still limited compared to state-of-the-art sparse arrays such as OS/TS-ENA and MISC arrays [55]-[56]. This is due to

¹This chapter is based on S. Wandale and K. Ichige, “Flexible Extended Nested Array with Multiple Subarrays Achieving Improved Degrees of Freedom,” *2022 30th European Signal Processing Conference (EUSIPCO)*, Belgrade, Serbia, 2022, pp. 1931-1935, doi: [10.23919/EUSIPCO55093.2022.9909786](https://doi.org/10.23919/EUSIPCO55093.2022.9909786) and S. Wandale, and K. Ichige, “Flexible extended nested arrays for DOA estimation: Degrees of freedom perspective,” *Signal Processing*, vol. 201, no. 108710, 2022. ISSN 0165-1684, <https://doi.org/10.1016/j.sigpro.2022.108710>.

the fact that regardless of the number of sensors per configuration, only three sensors are relocated. Thus, there is still potential for further improvement of the ENAMS array either for DOF enhancement or MC effect reduction.

In this chapter, we extend the work in Chapter 3 [54], where an extended nested array with multiple subarrays (ENAMS) is derived and provides a flexible way to construct ENAMS-like arrays with enhanced DOF than other state-of-the-art sparse arrays. Thus, we propose a flexible extended nested with multiple subarrays (f-ENAMS) configurations with improved DOF. The f-ENAMS arrays are constructed by splitting the dense subarray of the NA into four subarrays and relocating them on either side of the NA configuration to maximize the DOF. More importantly, f-ENAMS arrays have a closed-form expression for sensor positions and corresponding achievable DOF. Furthermore, numerical examples are presented to demonstrate the merits of the f-ENAMS arrays in terms of achievable DOF, weight functions, and DOA estimation performance.

In summary, our main contributions in this chapter are as follows: i) We propose a flexible extended nested array with multiple subarrays geometries (f-ENAMS). The proposed f-ENAMS array geometries are in two forms: f-ENAMS type-I (f-ENAMS-I) and type-II (f-ENAMS-II). The proposed f-ENAMS arrays show improved DOF compared to other sparse linear arrays and retain a hole-free DCA; (b) Furthermore, we derive closed-form expressions for the determination of achievable DOF, the number of relocated sensors, and sensor positions of the entire f-ENAMS array configurations; and (c) present theoretical and numerical simulation examples to validate the superiority of the proposed f-ENAMS arrays in terms of the achievable DOF, weight functions, and DOA estimation performance.

The remainder of this chapter is organized as follows. The conventional sparse linear array is discussed in Section 4.2 as preliminaries to the proposed sparse linear array designs. Section 4.3 describes the proposed flexible extended nested array with multiple subarrays array designs. Numerical examples to demonstrate the superiority of the proposed sparse linear arrays are explored in Section 4.4. Finally, Section 4.5 concludes this work.

4.2 Conventional sparse linear arrays

The ENAMS array, as discussed in Chapter 3, consists of five subarrays where the dense ULA of the NA is split into three subarrays and the sparse ULA into two. Specifically,

$$\begin{aligned} \mathbb{S}_{enam} = & \langle 1, N_1 - 2 \rangle \cup (N_1 + 1) \cup 2N_2 + \langle 0, N_2 - 2 \rangle (N_1 + 1) \\ & \cup N_2(N_1 + 1) \cup N_2(N_1 + 1) + N_1 - 2, \end{aligned} \quad (4.1)$$

where $\langle \cdot \rangle$ denotes a range of integers. Even though the ENAMS array extends the aperture and DOF of the NA, a quick glance at (4.1) shows that only three sensors are relocated; two from the dense ULA and one from the sparse ULA. Consequently, the extended DOF is limited compared to other state-of-the-art arrays such as MISC [51] and OS/TS-ENA [53].

In the ANA [48], the NA's dense ULAs were grouped into right/left subarrays. Then, some sensors from the dense ULA were relocated to both sides of the sparse ULA of the NA, thereby increasing the overall DOF and reducing the mutual coupling effect concurrently [14]. In this work, inspired by the SNA [44] and ANA [48], we propose a flexible extended NA (f-ENAMS) configuration, which extends the NA by retaining the number of sensors in the sparse ULA of the NA and splitting the dense ULA into right/left subarrays like [48], [53]. Then, each of the right/left subarrays is split further into dense and sparse subarrays, thereby increasing the achievable DOF. As we shall see in the subsequent sections, the realized f-ENAMS array has improved DOF than the ENAMS array and other state-of-the-art sparse arrays.

4.3 Proposed flexible ENAMS array designs

This section discusses the proposed f-ENAMS arrays and their corresponding properties.

4.3.1 Flexible Extended NA with Multiple Subarrays-I

Definition 4.3.1. Given a pair of integers $N_1 \geq 10$ and $N_2 \geq 1$, the configuration of the f-ENAMS-I array can be expressed as

$$\mathbb{S} = \mathbb{S}_1 \cup \mathbb{S}_2 \cup \mathbb{S}_3 \cup \mathbb{S}_4 \cup \mathbb{S}_5, \quad (4.2)$$

$$\begin{cases} \mathbb{S}_1 = \{1 + (l_1 - 1) | 1 \leq l_1 \leq \mathcal{T} - 2\} \\ \mathbb{S}_2 = \{\mathcal{T}(l_2 + 1) + (l_2 - 2) | 1 \leq l_2 \leq 2\}, \\ \mathbb{S}_3 = \{(1 + l_3)(N_1 + 1) - 1 | 1 \leq l_3 \leq N_2\}, \\ \mathbb{S}_4 = \{N_2(N_1 + 1) + N_1 + l_4 \mathcal{T} | 1 \leq l_4 \leq 2\}, \\ \mathbb{S}_5 = \{N_2(N_1 + 1) + 2N_1 + 2 + l_5 | 1 \leq l_5 \leq \mathcal{T} - 2\}, \end{cases}$$

where $\mathcal{T} = \lfloor N_1/2 \rfloor$ and $\lfloor \cdot \rfloor$ is the floor operator.

The f-ENAMS-I array configuration, as defined in (4.2) consists of five subarrays. The dense ULA section of the NA is divided into four ULAs: \mathbb{S}_1 , \mathbb{S}_2 , \mathbb{S}_4 , and \mathbb{S}_5 . The sparse ULA section of the NA is retained as \mathbb{S}_3 with N_2 sensors. However, it starts from $2(N_1 + 1) - 1$ instead of $N_1 + 1$ as originally designed in the NA. As for \mathbb{S}_1 , it comprises of $\mathcal{T} - 2$ sensors placed at a unit spacing interval, whereas \mathbb{S}_2 consists of two sensors separated by a distance of $\mathcal{T} + 1$. With two sensors, \mathbb{S}_4 follows \mathbb{S}_3 , and \mathbb{S}_5 come after \mathbb{S}_4 with $\mathcal{T} - 2$ sensors separated by a unit spacing.

Figure 4.1 (c) shows the array configuration of the f-ENAMS-I array with $N_1 = 10$ and $N_2 = 2$. As shown in Fig. 4.1 (c), (4.2) renders $\mathbb{S}_1 = \{1, 2, 3\}$, $\mathbb{S}_2 = \{9, 15\}$, $\mathbb{S}_3 = \{21, 32\}$, $\mathbb{S}_4 = \{37, 42\}$ and $\mathbb{S}_5 = \{45, 46, 47\}$ thereby yielding a large array aperture than the NA (see Fig. 4.1 (a)) given the same number of sensors N . Note that \mathbb{S}_2 , \mathbb{S}_4 , and \mathbb{S}_5 are no longer limited to a single sensor but rather assume multiple sensors. These changes extend the array aperture further and enhance the achievable DOF. Also, the equal distribution of sensors from the dense subarray of the NA to \mathbb{S}_1 and \mathbb{S}_5 , along with the further relocation of sensors from \mathbb{S}_1 and \mathbb{S}_5 into \mathbb{S}_2 and \mathbb{S}_4 , helps to reduce the effect of sensors interacting with each other.

Accordingly, the following Lemma 4.3.2 holds for the f-ENAMS-I array.

Lemma 4.3.2. *Given $N_1 \geq 10$, $N_2 \geq 1$ and $N \geq 11$, the difference coarray of the f-ENAMS-I array is hole-free ULA, i.e., $\mathbb{D} = [-L_u, L_u]$ where $L_u = N_2(N_1 + 1) +$*

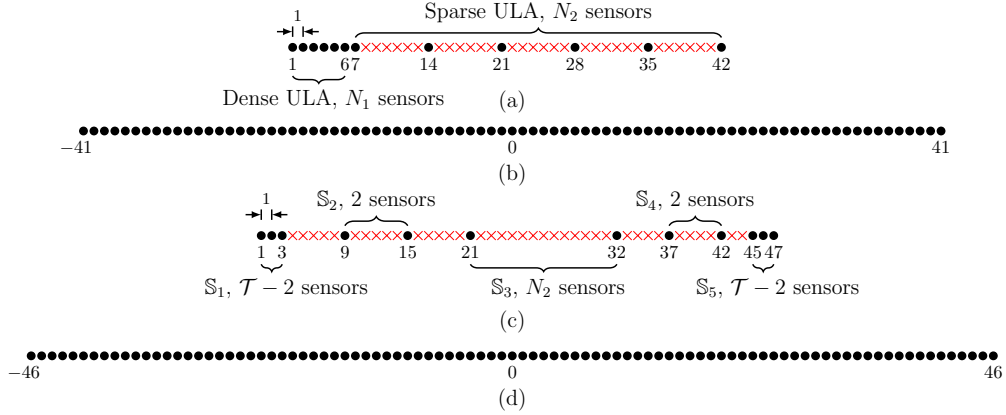


Figure 4.1: (a) Nested array configuration with $N_1 = N_2 = 6$, and $N = 12$, and (b) corresponding difference co-array. (c) f-ENAMS-I array configuration with $N_1 = 10$, $N_2 = 2$, and $N = 12$, and (d) corresponding difference co-array. The bullets denote physical sensors and the crosses represent empty spaces.

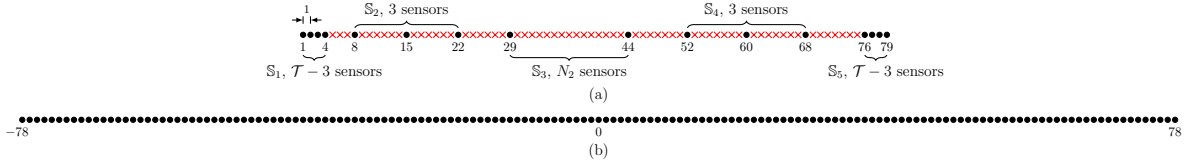


Figure 4.2: (a) an example of f-ENAMS-II array with $N_1 = 14$, $N_2 = 2$, and $N = 16$, and (b) corresponding difference co-array. The bullets denote physical sensors and the crosses represent empty spaces.

$$5N_1/2 - 1.$$

Proof. Refer to Appendix B (8.2). □

Following Lemma 4.3.2, it follows that

Property 4.3.3. For $N_1 \geq 10$, $N_2 \geq 1$ and $N \geq 11$, the f-ENAMS-I array yields a maximum uniform DOF of

$$\text{uDOF} = \begin{cases} N^2/2 + 3.5N - 28 & 11 \leq N \leq 14 \\ N^2/2 + 3.5N - 6 & 15 \leq N \leq 18 \\ N^2/2 + 3.5N - 1 & N \geq 19 \end{cases} \quad (4.3)$$

Proof. Refer to Appendix B (8.2). □

Moreover, based on Property 4.3.3, given the number of sensors N , the optimal parameters of N_1 should be an even number equivalent to

$$N_1 = \begin{cases} 2\lfloor(N+1)/4\rfloor + 4 & \text{if } 11 \leq N \leq 14, \\ 2\lfloor(N+1)/4\rfloor + 2 & \text{if } 15 \leq N \leq 18, \\ 2\lfloor(N+3)/4\rfloor & \text{if } N \geq 20. \end{cases} \quad (4.4)$$

and $N_2 = N - N_1$. For N_1 , we default to even numbers to ensure coarray continuity and improved DOF. In fact, the f-ENAMS-I array has enhanced DOF compared with the NA, ENA, INA, MISC, and the OS-ENA given the same number of sensors N . However, the f-ENAMS-I array shares the same uniform DOF as the TS-ENA array under certain optimal N_1 conditions. Therefore, in the subsequent section, we relocate extra sensors from the dense ULA section of the f-ENAMS-I array to improve further the overall array aperture [23].

4.3.2 Flexible extended NA with multiple subarrays-II

It is noteworthy that even though \mathbb{S}_2 and \mathbb{S}_4 in the f-ENAMS-I array no longer assume a single sensor, \mathbb{S}_2 and \mathbb{S}_4 are still restricted to two sensors each. Moreover, the f-ENAMS-I array shares the same uniform DOF as the TS-ENA array. As a result, we expanded the f-ENAMS-I array further to provide more flexibility and improve the overall achievable DOF.

Definition 4.3.4. Given a pair of integers $N_1 \geq 14$ and $N_2 \geq 1$, the f-ENAMS-II array configuration can be expressed as

$$\mathbb{S} = \mathbb{S}_1 \cup \mathbb{S}_2 \cup \mathbb{S}_3 \cup \mathbb{S}_4 \cup \mathbb{S}_5, \quad (4.5)$$

$$\begin{cases} \mathbb{S}_1 = \{1 + (l_1 - 1) | 1 \leq l_1 \leq \mathcal{T} - 3\}, \\ \mathbb{S}_2 = \{\mathcal{T}l_2 + 1 | 1 \leq l_2 \leq 3\}, \\ \mathbb{S}_3 = \{(1 + l_3)(N_1 + 1) - 1 | 1 \leq l_3 \leq N_2\}, \\ \mathbb{S}_4 = \{N_2(N_1 + 1) + N_1 + l_4(\mathcal{T} + 1) | 1 \leq l_4 \leq 3\}, \\ \mathbb{S}_5 = \{N_2(N_1 + 1) + 3N_1 + 3 + l_5 | 1 \leq l_5 \leq \mathcal{T} - 3\}, \end{cases}$$

where $\mathcal{T} = \lfloor N_1/2 \rfloor$.

Like the f-ENAMS-I array in (4.2), the f-ENAMS-II array consists of five sub-arrays, where the dense ULA section of the NA is divided into four ULAs: \mathbb{S}_1 , \mathbb{S}_2 , \mathbb{S}_4 , and \mathbb{S}_5 . Furthermore, the sparse ULA section of the NA is retained as \mathbb{S}_3 with N_2 sensors. Meanwhile, \mathbb{S}_1 and \mathbb{S}_5 are made up of $\mathcal{T} - 3$ sensors with a unit spacing. Unlike the f-ENAMS-I array, the number of sensors in \mathbb{S}_2 and \mathbb{S}_4 is not fixed to two but rather three sensors. Thus, bringing more flexibility to \mathbb{S}_2 and \mathbb{S}_4 . And this, coupled with a further reduction of sensors in \mathbb{S}_1 and \mathbb{S}_5 , extends the overall array aperture and eventually the achievable DOF. Figure 4.2 shows the array configuration of the f-ENAMS-II array with $N_1 = 14$ and $N_2 = 2$, where (4.5) yields $\mathbb{S}_1 = \{1, 2, 3, 4\}$, $\mathbb{S}_2 = \{8, 15, 22\}$, $\mathbb{S}_3 = \{29, 44\}$, $\mathbb{S}_4 = \{50, 60, 68\}$ and $\mathbb{S}_5 = \{76, 77, 78, 79\}$. As mentioned, it can be observed that the number of sensors in \mathbb{S}_2 and \mathbb{S}_4 are no longer fixed to two but three sensors.

And, according to (4.5), the following Lemma 4.3.5 holds for the f-ENAMS-II array,

Lemma 4.3.5. *Given $N_1 \geq 10$, $N_2 \geq 1$ and $N \geq 11$, the difference coarray of the f-ENAMS-II array is hole-free ULA, i.e., $\mathbb{D} = [-L_u, L_u]$ where $L_u = N_2(N_1 + 1) + 7N_1/2 - 1$.*

Proof. See Appendix B (8.2). □

Property 4.3.6. For $N_1 \geq 10$, $N_2 \geq 1$ and $N \geq 11$, the f-ENAMS-II array yields a maximum uniform DOF of

$$\text{uDOF} = \begin{cases} N^2/2 + 4.5N - 43 & 16 \leq N \leq 19 \\ N^2/2 + 4.5N - 13 & 20 \leq N \leq 23 \\ N^2/2 + 4.5N + 1 & N \geq 24 \end{cases} \quad (4.6)$$

Proof. See Appendix B (8.2). □

According to Property 4.3.6, optimal uniform DOF can be achieved by setting parameters N_1 and N_2 as

$$N_1 = \begin{cases} 2\lfloor N/4 \rfloor + 6 & \text{if } 16 \leq N \leq 19 \\ 2\lfloor N/4 \rfloor + 4 & \text{if } 20 \leq N \leq 23 \\ 2\lfloor N/4 \rfloor + 2 & \text{if } N \geq 24 \end{cases} \quad (4.7)$$

and $N_2 = N - N_1$ given the number of sensors N . Similarly, the value of N_1 is strategically fixed to even numbers to guarantee coarray continuity and enhanced DOF. Besides, compared to the f-ENAMS-I array, the f-ENAMS-II array has enhanced DOF than the NA, ENA, ANA, INA, MISC, and the TS-ENA given the same number of sensors N .

Remark 4.3.7. Note, to guarantee the continuity of the difference coarray, the extension requires $N_1 \geq 10$ for the f-ENAMS-I array and $N_1 \geq 14$ for the f-ENAMS-II array. And, if the value of N_1 for each array is less than the required value, the coarray becomes discontinuous. As for N_2 , both arrays hold when $N_2 \geq 1$, bringing the required minimum number of sensors to $N \geq 11$ for the f-ENAMS-I array and $N \geq 15$ for the f-ENAMS-II array. Moreover, the f-ENAMS-I array and the f-ENAMS-II array share the same array structure, as both array configurations consist of five subarrays. The difference between the two is in the number of sensors in the \mathbb{S}_2 and \mathbb{S}_4 subarrays, i.e., $n_{2,4}$. Specifically, in the f-ENAMS-I array $n_{2,4} = 2$, whereas in the f-ENAMS-II array $n_{2,4} = 3$.

Remark 4.3.8. Since $n_{2,4}$ corresponds to the number of sensors relocated from \mathbb{S}_1 and \mathbb{S}_5 , this means that the more the sensors are relocated from \mathbb{S}_1 and \mathbb{S}_5 into \mathbb{S}_2 and \mathbb{S}_4 , the larger the array aperture and overall achievable DOF. This phenomenon explains the differences in the achievable DOF by the f-ENAMS-I array and the f-ENAMS-II array. Furthermore, the same concept applies to the weight functions of each f-ENAMS array design. However, $n_{2,4}$ can be any number other than two or three, and further extension to such higher $n_{2,4}$ values is left as future work. In

the subsequent section, we evaluate the performance of the f-ENAMS array designs against other state-of-the-art sparse linear arrays.

4.4 Numerical examples

In this section, we present numerical examples to verify the performance of the f-ENAMS arrays in terms of weight functions, achievable DOF, and DOA estimation performance. Throughout the simulation examples, the ENAMS, improved NA, MISC, and TS-ENA arrays are used for comparison purposes. For the ENAMS and improved NA arrays, we choose parameters $N_1 = N_2 = 11$ and $N = 22$. For the f-ENAMS-I, f-ENAMS-II, MISC, and TS-ENA arrays, we set the parameters $(N_1 = 12, N_2 = 10)$, $(N_1 = 14, N_2 = 8)$, $(N = 22, P = 12)$, and $(N_1 = 14, N_2 = 7, N = 22)$, respectively. Note that all arrays contain 22 elements. Moreover, the spatial smoothing MUSIC algorithm [33], [34] is used for DOA estimation. The root-mean-square-error (RMSE) of estimated DOAs is adopted to evaluate DOA estimation performance. The RMSE computed over 1000 number of trials and is given as

$$\text{RMSE} = \sqrt{\frac{1}{1000K} \sum_{q=1}^{1000} \sum_{k=1}^K (\tilde{\theta}_k^q - \bar{\theta}_k)^2}, \quad (4.8)$$

where $\tilde{\theta}_k^q$ denotes the estimated normalized DOA of the true normalized DOA $\bar{\theta}_k$ in q -th trial.

4.4.1 Achievable degrees of freedom

In this section, we compare the DOF capacity of different kinds of nested arrays with the same number of elements N using the DOF ratio. Normally, the DOF ratio is defined as

$$\gamma(N) = N^2/L_u(N), \quad (4.9)$$

where N is the physical element number, and $L_u(N)$ is one-side of uniform DOF or size of aperture. Accordingly, the smaller the $\gamma(N)$, the higher the DOF capacity. Figure 4.3 shows the plot of the DOF ratio $\gamma(N)$ as a function of N . As shown in Fig. 4.3, out of the six sparse arrays, the ENAMS array has the highest values

Table 4.1: Achievable uniform DOF of different sparse linear arrays

Sparse array type	Optimal N_1	Optimal uniform DOF
NA	$N/2$	$N^2/2 + N - 1$
Enhanced NA	$N/2$	$N^2/2 + N + 1$
Improved Nested	$N/2$	$N^2/2 + 2N - 3$
ENAMS	$(N + 1)/2$	$N^2/2 + 2N - 9/2$
MISC	$2\lfloor N/4 \rfloor + 1$	$N^2/2 + 3N - 9$
f-ENAMS-I	$2\lfloor (N + 3)/4 \rfloor$	$N^2/2 + 3.5N - 1$
TS-ENA	$2\lfloor (N + 3)/4 \rfloor$	$N^2/2 + 3.5N - 1$
f-ENAMS-II	$2\lfloor N/4 \rfloor + 2$	$N^2/2 + 4.5N + 1$

of $\gamma(N)$, especially when $N < 50$, and improves as N increases. On the other hand, the f-ENAMS-II array has the lowest possible values except when $N < 20$. This is due to the restriction on the $N_1 = 14$ value as shown in (4.7) to guarantee a hole-free coarray. Hence, the achievable DOF of the f-ENAMS-II array when $N < 20$ is limited. However, as the value of N_1 becomes more flexible, the achievable DOF improves, particularly when $N \geq 20$. Meanwhile, the performance of the f-ENAMS-I array follows that of the f-ENAMS-II array, and shares almost similar values with the TS-ENA array under a certain value of N . Table 4.1 compares the maximum achievable DOF of various arrays using closed-form expressions. Clearly, the f-ENAMS-II array can achieve higher DOFs as compared to other state-of-the-art sparse arrays.

4.4.2 Weight functions

Figure 4.4 compares the weight functions for various sparse linear arrays with 22 sensors. As shown in Fig. 4.4, the INA and ENAMS arrays show the largest weight functions ($w(1) = 10, w(2) = 9, w(3) = 8$) and ($w(1) = 8, w(2) = 8, w(3) = 7$) respectively, owing to the existence of a dense ULA. Compared to the ENAMS and INA, the MISC array has the smallest weight functions ($w(1) = 1, w(2) = 8, w(3) = 1$). The TS-ENA and f-ENAMS-I arrays share the same weight functions

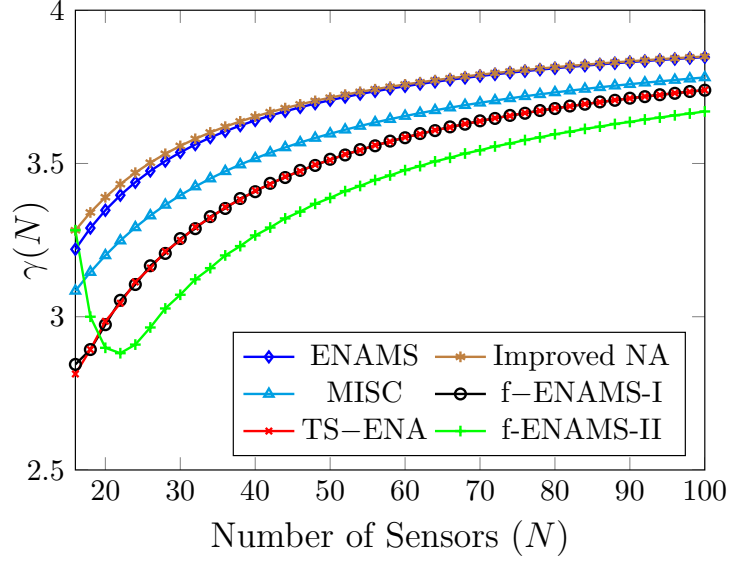


Figure 4.3: The DOF ratio $\gamma(N)$ versus the number of sensors N varying from 16 to 100.

($w(1) = 6, w(2) = 4, w(3) = 3$), whereas the weight functions of the f-ENAMS-II array are ($w(1) = 6, w(2) = 4, w(3) = 2$). The f-ENAMS-II array depends on a large value of N_1 to achieve a large aperture, and this is why it has higher weight functions. Although the weight functions of the f-ENAMS-II array are higher than those of the MISC and TS-ENA arrays, the f-ENAMS-II array has improved DOF, which ensures a better DOA estimation performance.

Remark 4.4.1. Concerning the mutual coupling effect, the f-ENAMS-I array has a weight function of $w(1) = N_1 - 6$ since (4.2) shows that 4 sensors are relocated from the dense ULA of the NA, and the remaining sensors are split into two. Similarly, the f-ENAMS-II array has $w(1) = 6$ as $N_1/2 + 1$ sensors are relocated from NA's dense ULA to realize the f-ENAMS-II array regardless of the number of sensors. The remaining sensors in the dense ULA are divided further into \mathbb{S}_1 and \mathbb{S}_5 . Therefore, the MC effect due to $w(1)$ is slightly stronger in the f-ENAMS-I array than in the MISC array but better than in the OS-ENA array. Moreover, the MC effect in the f-ENAMS-II array due to $w(1)$ is stronger than in the MISC and TS-ENA arrays but better than in the OS-ENA array.

4.4.3 DOA estimation in the absence of mutual coupling

In the second set of examples, we compare the DOA estimation performance among the ENAMS, improved NA, MISC, TS-ENA, f-ENAMS-I, and f-ENAMS-II arrays in the absence of a mutual coupling effect. All sparse arrays consist of 22 elements as described in Section 4.4.1.

MUSIC spectra of DOA estimation

Figure 4.5 compares the MUSIC spectra $P(\bar{\theta})$ of DOA estimation of the NA, improved nested array, MISC, TS-ENA, f-ENAMS-I and f-ENAMS-II array when $K = 32$ uncorrelated sources are located at $\bar{\theta}_k = -0.1 + 0.2(k - 1)/31$ for $1 \leq k \leq 32$ such that $\bar{\theta} = \sin(\theta)$. The input SNR is fixed at 0 dB, and the number of snapshots at 500. Figure 4.5 shows that all sparse arrays can resolve all 32 sources except for the ENAMS and improved NA arrays. The two show false peaks, and this is due to limited DOF. However, the proposed f-ENAMS-II array depicts all sources with well-delineated peaks followed by the TS-ENA, MISC, and f-ENAMS-I arrays. Therefore, the f-ENAMS-II array can provide a higher DOA estimation resolution than other sparse arrays.

RMSE of DOA estimation

In the following examples, we evaluate the RMSE performance versus the input SNR, the number of snapshots, and the number of sources. First, we compute the RMSE versus input SNR when $K = 50$ uncorrelated sources located at $\bar{\theta}_k = -0.3 + 0.6(k - 1)/49$ for $1 \leq k \leq 50$. The number of snapshots is fixed at 1000 whereas the input SNR varies from -30 to 10 dB. Second, with all other parameters fixed, we calculate the RMSE versus the number of snapshots when the input SNR = 0 dB, and the number of snapshots varies from 10 to 2000 . Lastly, we obtain the RMSE versus the number of sources where K sources are located at $\bar{\theta}_k = -0.3 + 0.6(k - 1)/(K - 1)$ for $1 \leq k \leq K$.

Figure 4.6 shows the RMSE of the normalized DOA estimates versus input SNR. It can be observed that the performance of all the sparse arrays improves as the SNR increases, and stabilizes when the SNR is higher than -10 dB. However, the

f-ENAMS-II array shows improved DOA estimation performance, followed by the TS-ENA, f-ENAMS-I, MISC, INA, and ENAMS arrays. Thus, the enhanced DOF of the f-ENAMS-II array improved the DOA estimation performance.

Figure 4.7 shows the RMSE of the normalized DOA estimates versus the number of snapshots. Like Fig. 4.6, the performance of all the sparse arrays improves as the number of snapshots increases. Moreover, the f-ENAMS-II array shows improved DOA estimation performance, followed by the TS-ENA, f-ENAMS-I, MISC, INA, and ENAMS arrays. Figure 4.8 shows the RMSE of the normalized DOA estimates versus the number of sources. Here, the performance of all sparse arrays degraded as the number of sources increased. However, the f-ENAMS-II array shows the lowest possible RMSE, and it is lower than those of the TS-ENA, f-ENAMS-I, MISC, INA, and ENAMS arrays. Thus, the enhanced DOF enables the f-ENAMS-II array to exhibit improved performance compared to other sparse arrays.

4.4.4 DOA estimation in the presence of mutual coupling

In the third example, we compare the DOA estimation performance of the ENAMS, improved NA, MISC array, TS-ENA, f-ENAMS-I, and f-ENAMS-II arrays in the presence of mutual coupling. As described in Section 4.4.1, 22 sensors were used for all array configurations.

For mutual coupling, the signal model in (2.5) is assumed. The parameters for the mutual coupling model were chosen as $c_1 = 0.2e^{j\pi/3}$, $B = 100$ and $c_\ell = c_1 e^{-j(\ell-1)/8}/\ell$ for $2 \leq \ell \leq B$. Firstly, we consider the RMSE of the normalized DOA estimation performance versus the input SNR and the absolute value of the mutual coupling coefficient $|c_1|$. The RMSE versus SNR was computed first with $K = 50$ uncorrelated sources located at $\bar{\theta}_k = -0.3 + 0.6(k-1)/49$ for $1 \leq k \leq 50$ and 1000 snapshots, and the SNR varies from -30 to 10 dB. Secondly, the RMSE versus $|c_1|$ was computed when SNR = 0 dB, number of snapshots $T = 1000$, $K = 50$ narrowband uncorrelated sources located at $\bar{\theta}_k = -0.3 + 0.6(k-1)/49$ for $1 \leq k \leq 50$, $c_1 = |c_1|e^{j\pi/3}$ such that $B = 100$ and $c_\ell = c_1 e^{-j(\ell-1)/8}/\ell$ for $2 \leq \ell \leq B$.

Figure 4.9 shows the RMSE of the normalized DOA estimates versus the input SNR. As shown in Fig. 4.9, although the mutual coupling of the f-ENAMS-II array is $w(1) = N_1 - 8$, the DOF of the f-ENAMS-II array is higher than those of the

MISC, TS-ENA, and f-ENAMS-I arrays. Hence, the f-ENAMS-II array obtains a better RMSE than the other sparse arrays. Moreover, the f-ENAMS-I array has almost the same RMSE as the TS-ENA array because the two share the same weight functions. Besides, the MISC array performs well than the f-ENAMS-I and TS-ENA arrays. Fig. 4.10 shows the RMSE of the normalized DOA estimates versus $|c_1|$. As shown in Fig. 4.10, the MISC array performs better than the f-ENAMS-I, f-ENAMS-II, and TS-ENA arrays because it has reduced mutual coupling compared to all other sparse arrays. However, the f-ENAMS-II array performs better when $|c_1| < 0.2$, and the performance degrades as $|c_1|$ increases.

4.5 Chapter summary

This chapter presented a new flexible extended nested array geometry with multiple subarrays (f-ENAMS) that provide enhanced DOFs and hole-free difference co-arrays. The proposed array configurations are designed to further distribute the NA's dense subarray sensors to the right side of the conventional NA to enhance the uniform DOF and reduce the mutual coupling effect. Simulation examples showed that the f-ENAMS arrays have enhanced DOF and provide high-resolution DOA estimation compared with other sparse linear arrays.

Although two f-ENAMS array designs (f-ENAMS-I and f-ENAMS-II) have been introduced, we limited our study to array designs in lower-level cases where \mathbb{S}_2 and \mathbb{S}_4 contain $n_{2,4} = 2$ and $n_{2,4} = 3$ sensors. Thus, the proposed f-ENAMS arrays are limited in terms of uniform DOF. Future work considers the expansion of the f-ENAMS arrays to a more generalized form featuring both low and high levels of $n_{2,4}$.

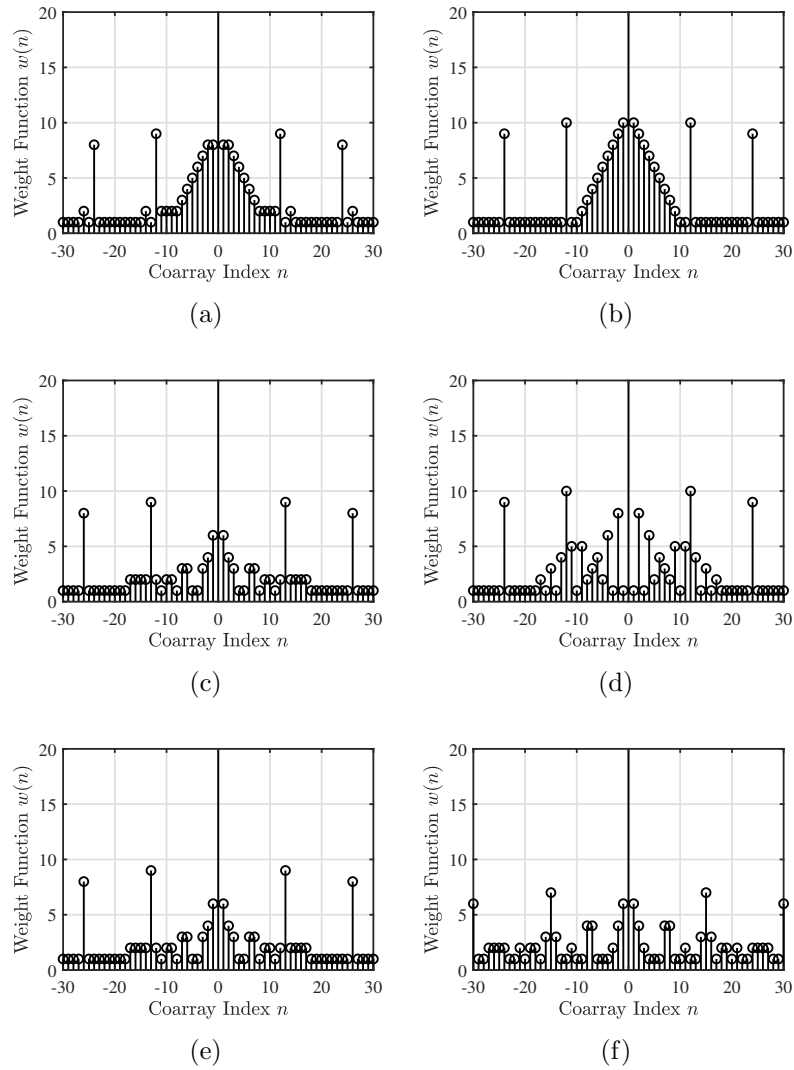


Figure 4.4: The weight functions for various sparse linear arrays with 22 sensors. (a) ENAMS, (b) Improved NA, (c) f-ENAMS-I, (d) MISC array, (e) TS-ENA, and (f) f-ENAMS-II.

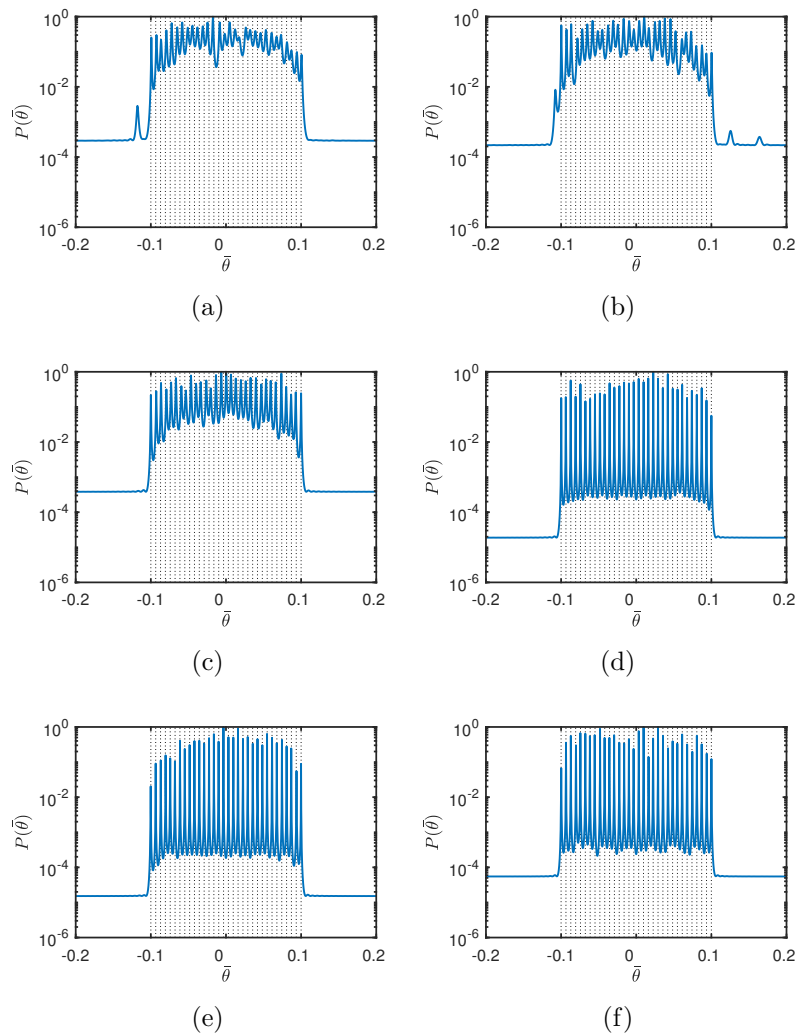


Figure 4.5: MUSIC spectra $P(\bar{\theta})$ comparison among (a) ENAMS, (b) Improved NA, (c) f-ENAMS-I, (d) MISC array, (e) TS-ENA and (f) f-ENAMS-II. The MUSIC spectra are computed using $N = 22$, SNR = 0 dB, 500 snapshots and $K = 32$ sources distributed in $\bar{\theta} = [-0.1, 0.1]$. Note, the dotted vertical lines on the $\bar{\theta}$ axis denote true DOAs.

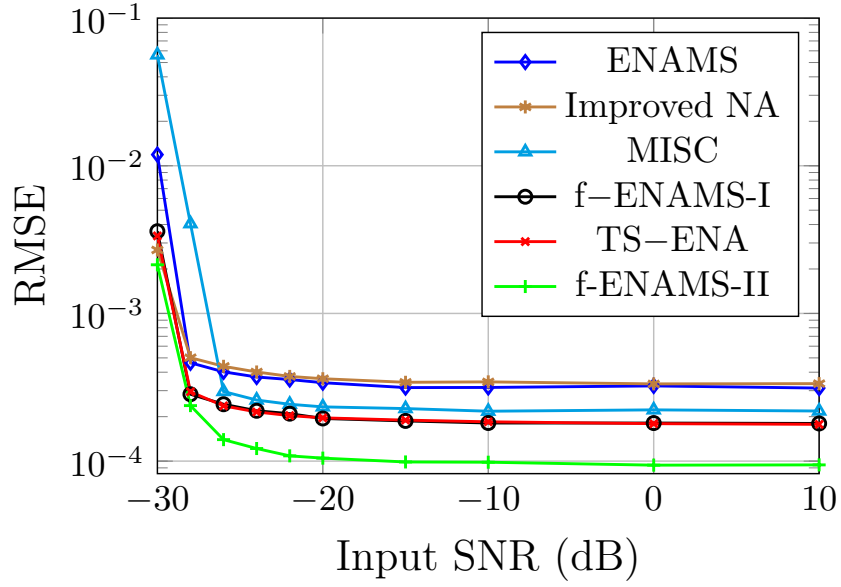


Figure 4.6: RMSE of the normalized DOA estimates versus the input SNR when $T = 1000$.

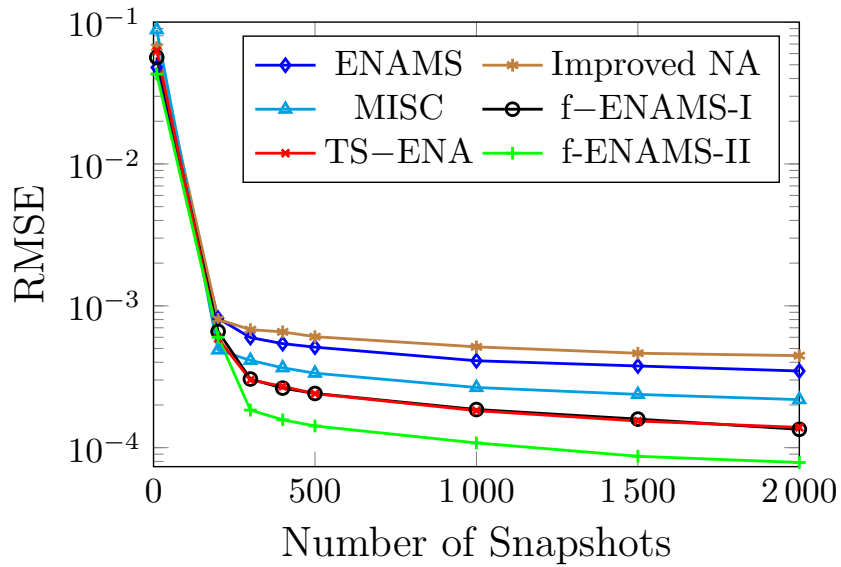


Figure 4.7: RMSE of the normalized DOA estimates versus the number of snapshots when SNR = 0 dB.

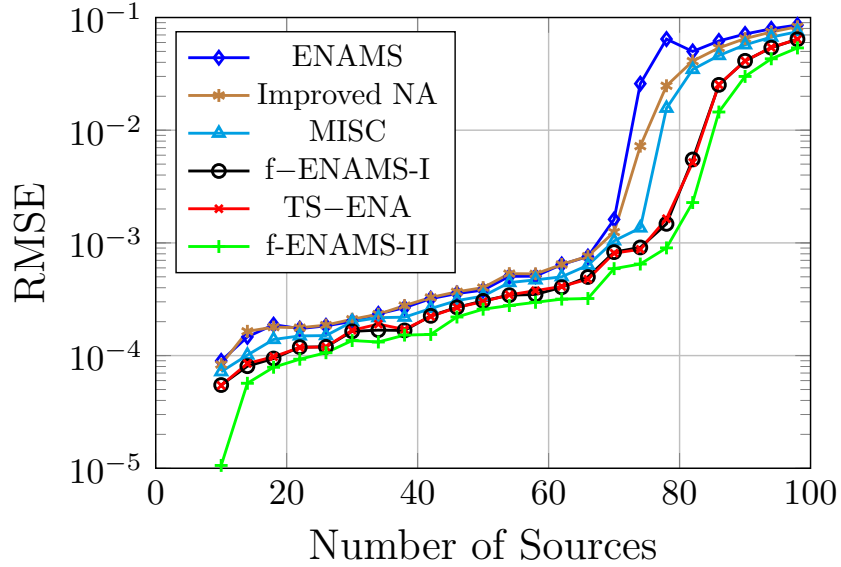


Figure 4.8: RMSE of the normalized DOA estimates versus the number of sources when SNR is 0 dB, $N = 22$, $T = 1000$ and K sources are located at $\bar{\theta}_k = -0.3 + 0.6(k - 1)/(K - 1)$ for $1 \leq k \leq K$.

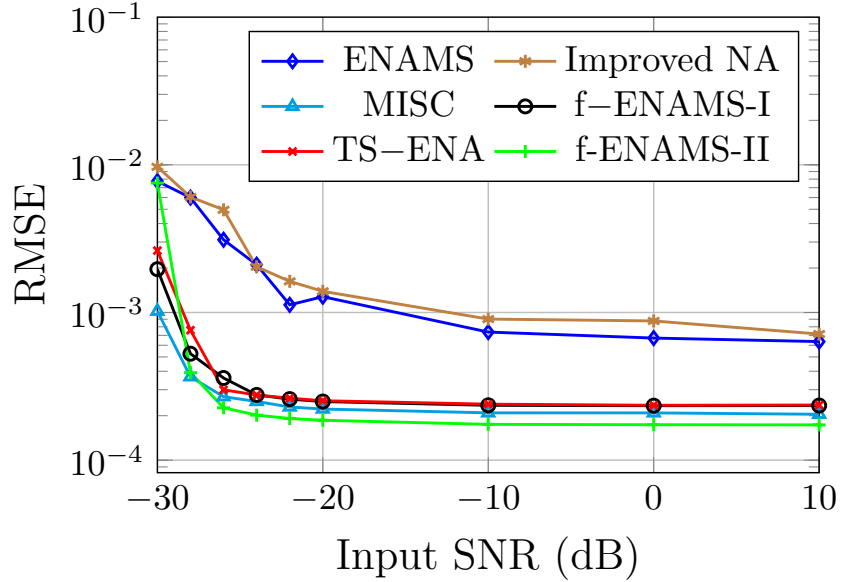


Figure 4.9: RMSE of the normalized DOA estimates versus the input SNR when the number of snapshots $T = 1000$, $N = 22$ and $K = 50$ sources are located at $\bar{\theta}_k = -0.3 + 0.6(k - 1)/49$ for $1 \leq k \leq 50$.

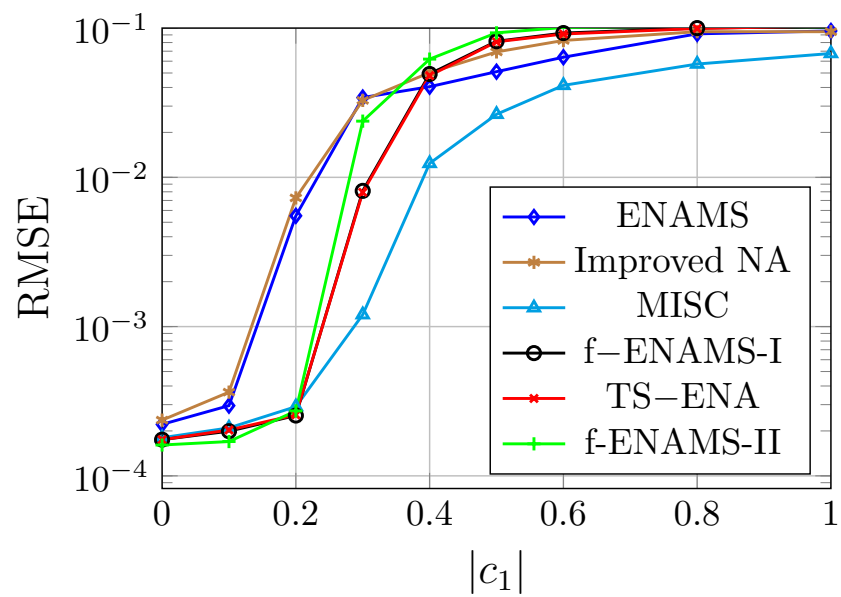


Figure 4.10: RMSE of the normalized DOA estimates versus $|c_1|$ when SNR is 0 dB, $N = 22$, $T = 1000$ and $K = 50$ sources are located at $\bar{\theta}_k = -0.3 + 0.6(k - 1)/49$ for $1 \leq k \leq 50$.

A Generalized Extended Nested Array Design via Maximum InterElement Spacing Criterion

5.1 Introduction

As discussed in Chapters 3-4, the sparse linear arrays (SLAs) such as the improved nested array (INA) [50], the extended nested array (ENA) [49], the extended nested array with multiple subarrays (ENAMS) [54], the augmented nested array (ANA) [48], the CA with displaced subarrays (CADiS) [62], the Iizuka NA (IINA) [52], the two-sides extended nested array (TS-ENA) [53], and the flexible extended nested array (f-ENAMS) [55]-[56], have been developed to improve the achievable degrees of freedom (DOF). On the contrary, the generalized non-redundant array (GNR) [58], the NA variants [61]-[63], and the CA variants [44], [72], [59]-[60] were designed with a focus on reduced mutual coupling (MC) effect. Thus, it is clear that the extension approaches above aim to reduce the mutual coupling or improve the degrees of freedom with little or no balance between the two determining factors.

Recently, a family of SLA structures based on the interelement spacing (IES) principle has been proposed [51], [64]-[65]. In this context, the IES criterion [64]-[65] is a method that uses a set of IES terms instead of integers to describe a sparse linear array. The IES approach saves space due to its compact form and captures the array sensor distribution pattern. Arrays such as the sparse array based on uniform linear array (ULA) fitting method with 4-layers (UF-4BL) [64], sparse array via maximum IES criterion (MISC) [51], and improved MISC array (IMISC) [65] are typical examples of IES-based SLAs. These IES-based arrays offer a relatively low MC effect and improved DOF, thereby yielding a good balance between the MC effect and achievable DOF [66]. Thus, the IES principle is one of the most promising array-designing approaches¹.

¹This chapter is based on S. Wandale and K. Ichige, "A Generalized Extended Nested Array Design via Maximum Inter-Element Spacing Criterion," *IEEE Signal Processing Letters*, vol. 30, pp. 31-35, 2023, doi: [10.1109/LSP.2023.3238912](https://doi.org/10.1109/LSP.2023.3238912).

Using the IES principle, this chapter explores the relationship and similarities between the previous chapter’s proposed f-ENAMS-II array and TS-ENA and presents a unified sparse linear array design. A generalized IES set pattern is derived by utilizing the IES set patterns of the two-sides extended nested array and the flexible extended nested array with multiple subarrays type-2. The generalized IES set is used to design the unified sparse array, which consists of six uniform linear arrays (ULAs). The proposed unified array is called the generalized extended nested array with multiple subarrays (GENAMS) array. Compared to other arrays, the GENAMS array has improved degrees of freedom and relatively less mutual coupling. Furthermore, the achievable DOF and the weight functions of the GENAMS array are derived and analyzed in detail. Finally, numerical examples are used to demonstrate the merits of the GENAMS array over other existing sparse arrays.

In summary, the main contributions in this chapter are as follows: i) We develop a generalized extended NA array structure with enhanced DOF via the array patterns of the TS-ENA and f-ENAMS-II arrays; ii) Deduce and analyze closed-form expressions of the GENAMS array for sensor locations, achievable DOF, and weight functions; and iii) Provide simulation examples to demonstrate exceptional performance of the GENAMS array in terms of DOA estimation performance, coupling leakage, and DOF ratio.

This chapter is organized as follows. First, the conventional sparse linear arrays from which the proposed sparse array design is drawn are reviewed in Section 5.2. Then, the proposed generalized sparse array design is discussed in Section 5.3. Next, section 5.4 examines different numerical examples to validate the performance of the proposed sparse array design. Lastly, concluding remarks are discussed in Section 5.5.

5.2 Conventional sparse linear arrays

In this section, we review the sensor distribution patterns of the TS-ENA and the f-ENAMS-2 array using the IES criterion, as demonstrated in [65], to understand the underlying IES array patterns of these two sparse linear arrays. Then, the closed-form expressions of the TS-ENA and the f-ENAMS-2 are reformulated and

represented in one unified framework, as proposed in [66]. Finally, following the unified framework, the IES array patterns are generalized into a single unified sparse linear array pattern.

5.2.1 Maximum interelement spacing constrained array

In [51], an interelement spacing criterion-based Maximum Interelement Spacing Constrained (MISC) array is introduced with enhanced degrees of freedom and reduced mutual coupling effect. The MISC array is controlled by an IES term Q , and an IES set \mathbb{A}_{misc} such that

$$\mathbb{A}_{misc} = \{1, Q - 3, Q^r, 2^z, 3, 2^z\}, \quad (5.1)$$

where $Q = 2\lfloor N/4 \rfloor + 2$, $r = N - Q$, and $z = (Q - 4)/2$, for $N \geq 5$. Note that in (5.1), the notation x^n denotes n repetitions of the term x [51], [65]-[66]. Namely, x denotes the interelement spacing term, and n is the number of times the term has been repeated within that particular section of the array.

Given the number of sensors $N \geq 5$, the MISC array achieves $\frac{N^2}{2} + 3N - 9$ uniform DOF, and the first three weight functions as $w(1) = 1$, $w(2) = 2\lfloor N/4 \rfloor - 2$ and $w(3) = 2$ [51]. Compared to other state-of-the-art sparse arrays like the ENAMS array, the MISC array yields higher uniform DOF and a reduced mutual coupling effect [56]. Figure 5.1 shows the MISC array with 12 sensors where $Q = 8$, $r = 4$, and $z = 2$.

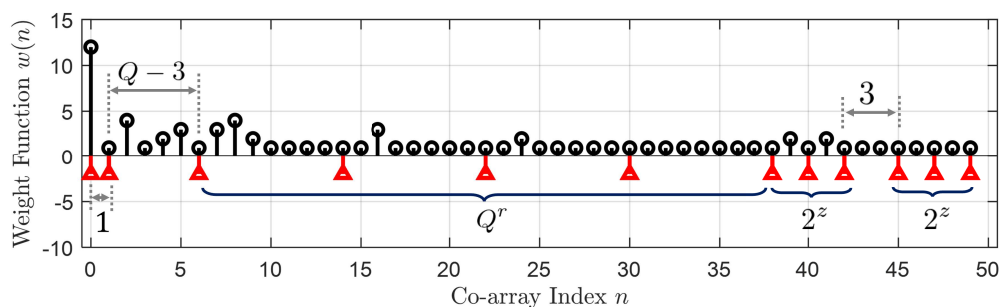


Figure 5.1: The MISC array configuration with $N = 12$ sensors ($Q = 8$, $r = 4$, $z = 2$) and corresponding coarray weight functions (only positive segment is shown in the view of $w(n) \in [0, 15]$). In the figure, the red stems denote physical sensors.

5.2.2 TS-ENA array via interelement spacing criterion

Independently, while attempting to improve further the DOF of the NA array, a two-sides extended nested array (TS-ENA) was introduced in [53] via the extended nested array (ENA) strategy. The ENA strategy [53], [54] holds on the basis that the virtual sensors in the difference co-array are located in the range

$$v = (N_1 + 1)(\ell_1 - 1) + (N_1 + 1 + \ell_2) \quad (5.2)$$

where $\ell_1 \in [1, N_2]$ and $\ell_2 \in [0, N_1]$. Thus, the ENA strategy is designed such that the left/right (\mathbb{L}/\mathbb{R}) subarrays are placed N_2 further than in ANA (the ANA array consists of three main subarrays in this order, the left (\mathbb{L}), middle (\mathbb{M}) and right (\mathbb{R}) subarrays). Thus, the strategy expands the distance between the ANA's \mathbb{L}/\mathbb{R} and \mathbb{M} subarrays, thereby enhancing the overall aperture and achievable DOF [48], [53].

Compared to the MISC array, the TS-ENA has improved DOF but a slightly more severe mutual coupling effect than the MISC array due to a large number of sensor pairs with separation one it inherits from the ANA array [53], [54]. According to [53], for $N \geq 12$, the TS-ENA can be expressed as

$$\mathbb{S}_{ts-ena} = \mathbb{L} \cup \mathbb{M} \cup \mathbb{R}, \quad (5.3)$$

$$\begin{cases} \mathbb{L} = (N_1 + 1) - l_1, & l_1 \in \mathbb{Q}_1 \\ \mathbb{M} = (N_1 + 1)l_2, & l_2 \in [1, N_2] \\ \mathbb{R} = l_3 - (N_1 + 1)(N_2 + 1), & l_3 \in \mathbb{Q}_2 \end{cases} \quad (5.4)$$

where $i = \lfloor N_1/2 \rfloor$, $\mathbb{Q}_1 = \{0, i, 2i, 2i + 3 : 3i\}$, $\mathbb{Q}_2 = \{0, i + 1, 2i + 2, 3i + 3 : 4i\}$, $N_1 = 2\lfloor (N + 3)/4 \rfloor$ and $N_2 = N - N_1 - 1$ [53]. Note, \mathbb{Q}_1 and \mathbb{Q}_2 are the relative sensor position vectors.

Figure 5.2 shows a typical example of a TS-ENA array with $N = 17$ sensors where $N_1 = 14$ and $N_2 = 2$. Given $N = 17$, $N_1 = 14$ and $N_2 = 2$, (5.3) yields $\mathbb{L} = \{0, 7, 14, 17, 18, 19, 20, 21\}$ and $\mathbb{R} = \{0, 8, 16, 24, 25, 26, 27, 28\}$. It can be observed in Fig. 5.2 that the TS-ENA array has a hole-free difference co-array and improved weight functions compared to those of NA. Besides, for $N \geq 12$, the TS-ENA yields $\frac{N^2}{2} + 3.5N - 1$ uniform DOF and the first three weight functions of $w(1) = N_1 - 4$,

$w(2) = N_1 - 6$ and $w(3) = N_1 - 7$ [53], [56]. Thus, TS-ENA has improved uniform DOF and reduced mutual coupling compared to other existing sparse arrays.

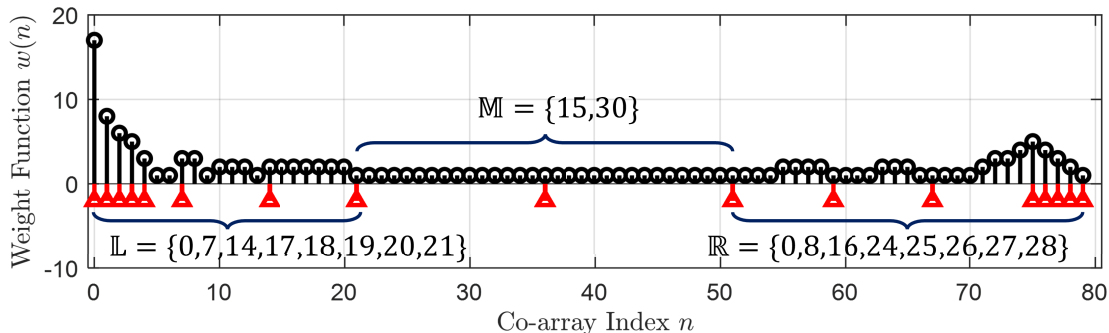


Figure 5.2: The TS-ENA array configuration with $N = 17$ sensors ($N_1 = 14$ and $N_2 = 2$) and corresponding coarray weight functions (only positive segment is shown in the view of $w(n) \in [0, 15]$). In the figure, the red stems denote physical sensors.

5.2.3 Flexible ENAMS array via IES principle

Following the TS-ENA array, without the knowledge of its underlying IES pattern, the flexible extended nested array with multiple subarray type-II (f-ENAMS-2) was proposed in [55]-[56] by extending the ANA array, where the sensors with a unit spacing in \mathbb{Q}_1 and \mathbb{Q}_2 subarrays were further distributed into the \mathbb{M} subarray thereby achieving an extended array aperture and the uniform DOF. Using exact sensor location information, the f-ENAMS-2 can be defined as

$$\mathbb{S}_{f-enams} = \mathbb{Z}_1^f \cup \mathbb{Z}_2^f \cup \mathbb{Z}_3^f \cup \mathbb{Z}_4^f \cup \mathbb{Z}_5^f, \quad (5.5)$$

$$\begin{cases} \mathbb{Z}_1^f = \{l_1 | 1 \leq l_1 \leq \mathcal{L} - 3\}, \\ \mathbb{Z}_2^f = \{\mathcal{L}l_2 + 1 | 1 \leq l_2 \leq 3\}, \\ \mathbb{Z}_3^f = \{(1 + l_3)(N_1 + 1) - 1 | 1 \leq l_3 \leq N_2\}, \\ \mathbb{Z}_4^f = \{N_2(N_1 + 1) + N_1 + l_4(\mathcal{L} + 1) | 1 \leq l_4 \leq 3\}, \\ \mathbb{Z}_5^f = \{N_2(N_1 + 1) + 3N_1 + 3 + l_5 | 1 \leq l_5 \leq \mathcal{L} - 3\}, \end{cases} \quad (5.6)$$

where $\mathcal{L} = \lfloor N_1/2 \rfloor$, $N_1 = 2\lfloor N/4 \rfloor + 2$ and $N_2 = N - N_1$ for $N \geq 15$ [55]. Besides, as discussed in Chapter 4, the f-ENAMS-2 yields $\frac{N^2}{2} + 4.5N - 1$ uniform DOF and

the first three weight functions of $w(1) = N_1 - 6$, $w(2) = N_1 - 8$ and $w(3) = N_1 - 9$. Although the f-ENAMS-2 has improved uniform DOF than the TS-ENA and the MISC, the mutual coupling effect in f-ENAMS-2 remains relatively higher than in the MISC array, as judged by the weight functions. Figure 5.3 depicts the f-ENAMS-2 array configurations with $N = 17$. From Fig. 5.3, the f-ENAMS-2 array exhibits hole-free difference co-array characteristics.

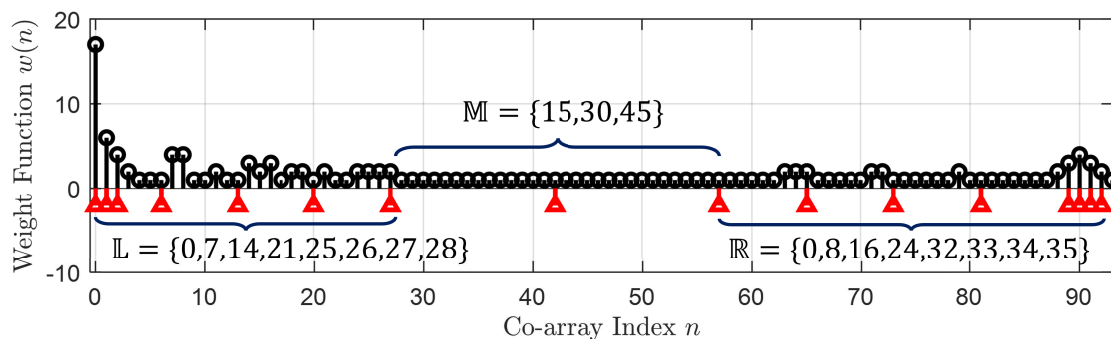


Figure 5.3: The f-ENAMS-2 array configuration with $N = 17$ sensors ($N_1 = 14$ and $N_2 = 2$) and corresponding coarray weight functions (only positive segment is shown in the view of $w(n) \in [0, 20]$). In the figure, the red stems denote physical sensors.

5.2.4 TS-ENA vs. flexible ENAMS array configuration

Lemma 5.2.1. *The TS-ENA and the f-ENAMS-2 share the same basic array structure and differ only in the number of sensors in the far left and right subarrays, i.e., the \mathbb{L} and \mathbb{R} subarrays.*

Proof. To demonstrate Lemma 5.2.1, let us consider definitions (5.3) and (5.5), and reformulate them in terms of the IES criterion [65]-[66], [51]. Without loss of generality, the TS-ENA array can be expressed using the interelement spacing term Q and set A_{ts-ena} as

$$A_{ts-ena} = \{1^{z-1}, (P+1)^3, Q^r, P^2, 3, 1^{z-1}\}, \quad (5.7)$$

where $Q = 2\lfloor(N+3)/4\rfloor + 1$, $r = N - Q$, $z = \lceil(Q+1)/4\rceil$ and $P = (Q-1)/2$.

Rearranging the terms in (5.7) yields

$$\mathbb{A}_{ts-ena} = \{1^{z-1}, 3, P^2, Q^r, (P+1)^3, 1^{z-1}\}. \quad (5.8)$$

Similarly, the f-ENAMS-2 array can be reformulated using the interelement spacing term Q , and set $\mathbb{A}_{f-enams}$ as

$$\mathbb{A}_{f-enams} = \{1^{z-1}, 4, P^3, Q^r, (P+1)^4, 1^{z-1}\}. \quad (5.9)$$

where $Q = 2\lfloor N/4 \rfloor + 3$, $r = N - Q$, $z = \lceil (Q+1)/4 \rceil$ and $P = (Q-1)/2$. Therefore, it follows from (5.8) and (5.9) that the TS-ENA and the f-ENAMS-2 array share the same basic array structure and differ only in the values of the second, third, and fifth terms, which are fixed regardless of the number of sensors N . \square

Lemma 5.2.2. *Suppose that the 2nd, 3rd and the 5th terms in (5.3) are given as z , P^{z-1} and $(P+1)^z$ where $z \in \mathbb{N}^+$. Then, the TS-ENA array can be mapped to any z -level array whose uniform DOF is N higher than the previous z -level.*

Proof. The Lemma 5.2.2 can be verified by comparing (5.8) and (5.9). Here, the fixed terms of the TS-ENA array and the f-ENAMS-2 array differ by 1, i.e., $\{3, P^2, (P+1)^3\}$ and $\{4, P^3, (P+1)^4\}$ for the TS-ENA array and the f-ENAMS-2 array, respectively. Hence, the f-ENAMS-2 array is a $z+1$ extension of the TS-ENA array. Besides, according to [53] and [66], the DCA of both (5.3) and (5.5) are hole-free ULAs. And, the maximum positions of the TS-ENA array and the f-ENAMS-2 array via (5.3) are $N_2(N_1+1) + 3.5N_1$ and $N_2(N_1+1) + 4.5N_1$, respectively, which leads to a uniform DOF difference of N considering that both TS-ENA and f-ENAMS-2 arrays are hole-free. Thus, every unit change in z -level increases the uniform DOF by N . \square

To quantitatively demonstrate Lemma 5.2.2, we compute the DOF capacity versus the number of sensors for different z -level array configurations. The DOF capacity is given by a DOF ratio as defined in (2.2.5) [48]. As you may recall, the smaller the $\gamma(N)$, the higher the DOF capacity [56]. Figure 5.4 shows the $\gamma(N)$ plot versus the number of sensors N . As shown in Fig. 5.4, the DOF capacity increases as the z -level level increases. However, the required minimum number of sensors becomes

higher. For instance, a 3-level array requires a minimum of 11 sensors, whereas a 4-level array requires 15. To resolve this, we generalize all z -level array configurations into a unified sparse array geometry and ultimately generalize the achievable DOF capacity (Fig. 5.4, dotted line).

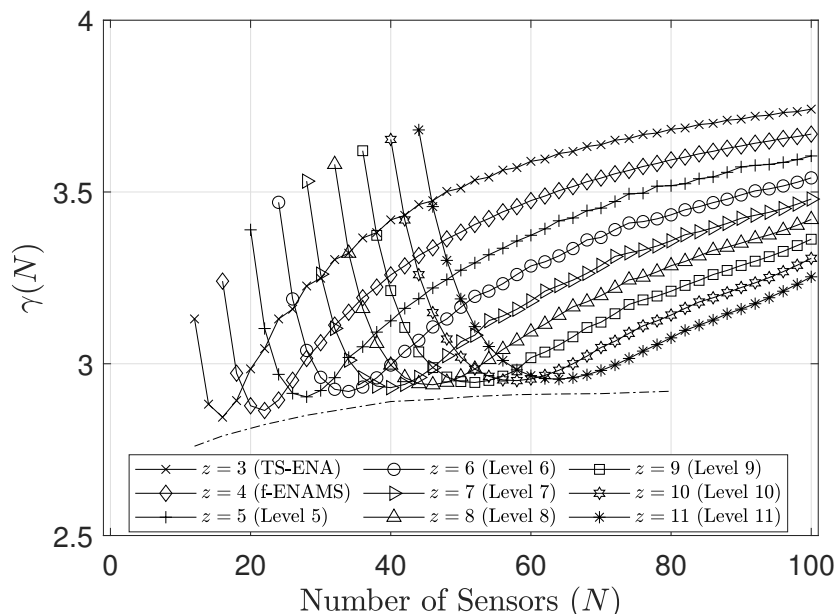


Figure 5.4: Comparison of the DOF ratio versus the number of sensors N for various z -level sparse arrays.

We unify the two sparse linear array geometries in the subsequent section, motivated by Lemma 5.2.1 and 5.2.2, by leveraging the three constant IES terms.

5.3 Proposed generalized ENAMS array design

Following Lemma 5.2.1 and 5.2.2 in Section 5.2, we propose a new generalized extended nested array with multiple subarrays (GENAMS) by generalizing the fixed (2nd, 3rd and 5th) terms of (5.8) and (5.9). The GENAMS array can be expressed using the IES term Q , and an IES set \mathbb{A}_{genams} as

$$\mathbb{A}_{genams} = \{1^{z-1}, z, P^{z-1}, Q^r, (P+1)^z, 1^{z-1}\}. \quad (5.10)$$

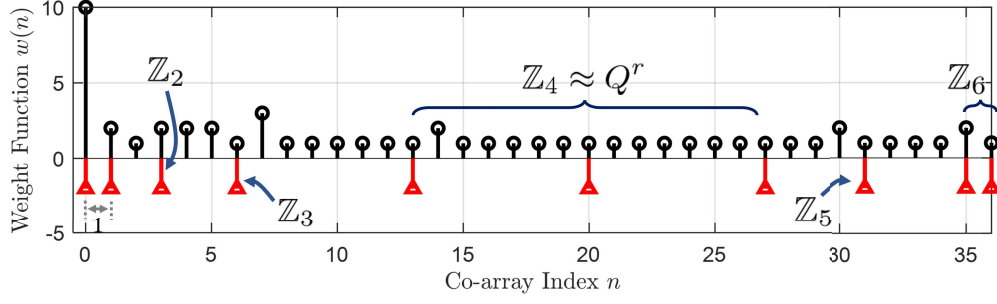


Figure 5.5: An example of the GENAMS array with $N = 10$ sensors ($Q = 7$, $r = 3$, $P = 3$ and $z = 2$) and corresponding coarray weight functions (only positive segment is shown in the view of $w(n) \in [0, 10]$). In the figure, the red stems denote physical sensors.

where $Q = 4\lfloor(N + 5)/6\rfloor - 1$, $r = N - Q$, $z = (Q + 1)/4$ and $P = (Q - 1)/2$. The corresponding exact sensor locations can be expressed as a union of six subsets

$$\left\{ \begin{array}{l} \mathbb{Z}_1 = \{0, 1, \dots, z - 1\}, \\ \mathbb{Z}_2 = 2z - 1, \\ \mathbb{Z}_3 = \{2P, 3P, \dots, zP\}, \\ \mathbb{Z}_4 = \{zP + Q, zP + 2Q, \dots, zP + Qr\}, \\ \mathbb{Z}_5 = zP + Qr + \{(P + 1), \dots, z(P + 1)\}, \\ \mathbb{Z}_6 = z(2P + 1) + Qr + \{0, 1, \dots, z - 1\}, \end{array} \right. \quad (5.11)$$

where each subset chronologically corresponds to a term in (5.10). The GENAMS array leverages changing values of the 2nd, 3rd, and 5th terms, otherwise fixed in TS-ENA and f-ENAMS-2, to realize a large array aperture. Figure 5.5 shows a GENAMS array with $N = 10$ sensors, $Q = 7$, $r = 3$, $P = 3$ and $z = 2$ where (5.10) yields $\mathbb{Z}_1 = \{0, 1\}$, $\mathbb{Z}_2 = \{3\}$, $\mathbb{Z}_3 = \{6\}$, $\mathbb{Z}_4 = \{13, 20, 27\}$, $\mathbb{Z}_5 = \{31\}$, and $\mathbb{Z}_6 = \{35, 36\}$. Thus, the sensor positions of the GENAMS array can be uniquely determined using (5.10) given any value of N . Hence, the GENAMS array has a closed-form expression for sensor positions. Also, the DCA of the GENAMS array is hole-free, as summarized in Lemma 5.3.1.

Lemma 5.3.1. *The difference co-array of the GENAMS array as defined in (5.10) is a hole-free ULA, i.e., $\mathbb{D}_g = [-L_u, L_u]$ with $L_u = Q(r + z) + z - 1$.*

Proof. See Appendix C (8.2). □

Following Lemma 5.3.1, we obtain the following properties.

Property 5.3.2. Given that $Q = 4\lfloor(N + 4)/6\rfloor - 1$, $r = N - Q$, $z = (Q + 1)/4$ and $P = (Q - 1)/2$. The uniform DOF of GENAMS array is $\frac{2N^2}{3} + \frac{2N}{3} - 1$ for any value of $N \geq 10$.

Proof. Refer to Appendix C (8.2). □

Therefore, the GENAMS array yields improved uniform DOF than the TS-ENA array ($N^2/2 + 3.5N - 1$) and f-ENAMS-2 array ($N^2/2 + 4.5N + 1$) given the same number of sensors N .

Property 5.3.3. According to (5.10), for $N \geq 10$ the first three weight functions of GENAMS array are

$$w(1) = 2z - 2, \quad w(2) = \begin{cases} 1, & 14 > N \geq 10 \\ 2z - 4, & N \geq 14. \end{cases} \quad (5.12)$$

$$w(3) = \begin{cases} 2, & 14 > N \geq 10 \\ 1, & 20 > N \geq 14 \\ 2z - 6, & N \geq 20. \end{cases} \quad (5.13)$$

Proof. See Appendix C (8.2). □

Comparing with weights of the TS-ENA and f-ENAMS-2 array, the weights in Property (5.3.3) are less than $w(1) = Q - 7$, $w(2) = Q - 9$, and $w(3) = Q - 10$ weight functions of the TS-ENA array as well as $w(1) = Q - 9$, $w(2) = Q - 11$, and $w(3) = Q - 13$ weights of the f-ENAMS-2 array. However, the weights are higher than those of the ICNA [59], IMISC [65], and UF-4BL array [64].

5.4 Numerical examples

This section examines the performance of the GENAMS array against other sparse linear arrays under different scenarios. The SS-MUSIC [33] is used for DOA es-

timization. The root-mean-square error (RMSE) of estimated DOA computed over 1000 trials is used as the performance metric. The following parameters are fixed throughout this section: $N = 30$ sensors for all arrays, the mutual coupling factors of $c_1 = 0.2e^{j\pi/3}$, and $c_g = c_1e^{-j(g-1)/8}/g$, $2 \leq g \leq 100$, and $T = 1000$ snapshots [57].

5.4.1 DOF capacity and coupling leakage analysis

First, we examine the uniform DOF capacity of various sparse linear arrays using the DOF ratio as $\gamma(N) = N^2/L_u(N)$ [48]. Remember, the higher the uniform DOF capacity, the smaller the $\gamma(N)$ value [57]. Figure 5.6 shows the DOF ratios of various sparse linear arrays. As shown in Fig. 5.6, the proposed GENAMS array has the highest uniform DOF among the existing sparse linear arrays, and NA has the least uniform DOF capacity. However, as N increases, the uniform DOF of the GENAMS array slightly degrades but still outperforms other arrays.

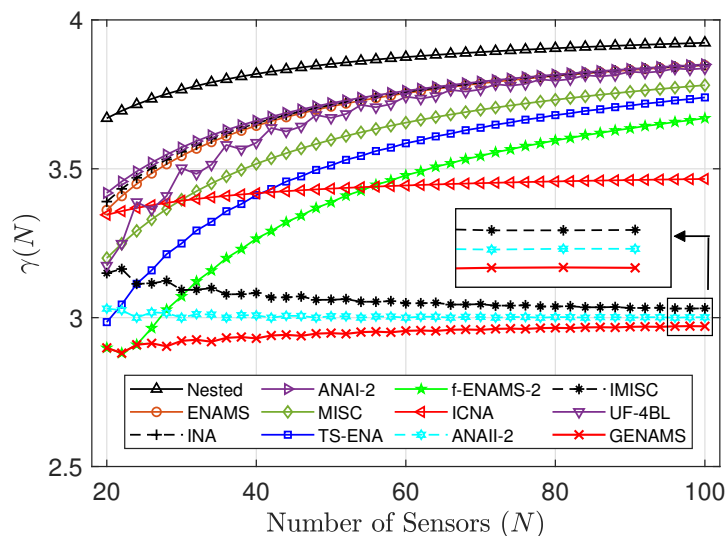


Figure 5.6: Comparison of DOF ratio $\gamma(N)$ versus the number of sensors N for various sparse linear arrays.

Next, we consider the coupling leakage of various sparse linear arrays as shown in Fig. 5.7. In this example, Fig. 5.7 shows that the coupling leakage of the GENAMS array is lower than those of the NA, INA, ENAMS, TS-ENA, and f-ENAMS-2 but higher than the selected few sparse linear arrays. However, the GENAMS array has

higher uniform DOF capacity than other sparse arrays, guaranteeing better DOA estimation performance [54]-[57].

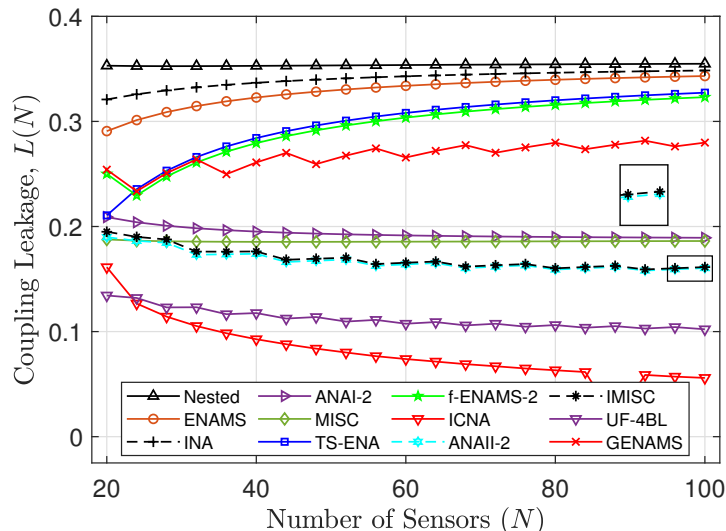


Figure 5.7: Comparison of coupling leakage $L(N)$ versus the number of sensors N for various sparse linear arrays.

5.4.2 RMSE of DOA estimation in the presence of MC

In this section, we demonstrate the DOA estimation performance of the proposed GENAMS array compared to other sparse linear arrays. The RMSE versus input SNR in the presence of a mutual coupling effect is examined first. In this example, 50 uncorrelated sources in the range $\bar{\theta}_m = -0.45 + 0.8(m - 1)/49$ for $m \in [1, 50]$ are used, and the input SNR is varied in the range $-30 \leq \text{SNR} \leq 10$ dB. Figure 5.8 shows the plot of RMSE versus input SNR for various sparse linear arrays. It is clear from Fig. 5.8 that the GENAMS array outperforms other sparse arrays because of its large uniform DOF and relatively low mutual coupling.

Finally, the RMSE versus $|c_1|$ is then evaluated. Here, with all other parameters constant, the SNR is fixed at 0 dB, and the $|c_1|$ ranges between 0 and 0.6. Figure 5.9 shows the plot of RMSE versus $|c_1|$ for various sparse linear arrays. As shown in Fig. 5.9, the GENAMS array performs well when $|c_1| < 0.25$; however, the ICNA and UF-4BL outperform the GENAMS array when $|c_1| > 0.3$. However, as we have observed

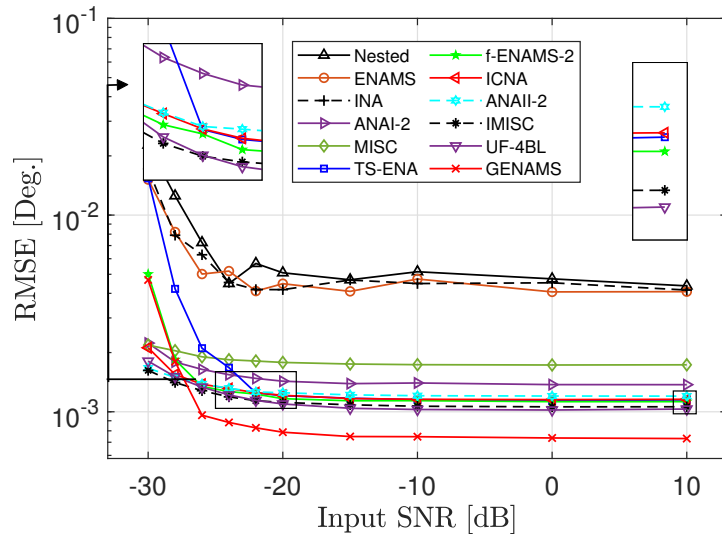


Figure 5.8: Comparison of RMSE versus input SNR for various sparse linear arrays.

in Fig. 5.8, in lower $|c_1|$ cases, the size of uniform DOF adds DOA estimation performance advantage to sparse arrays. Hence, balancing the two factors—mutual coupling and uniform DOF is paramount when designing a sparse linear array to ensure optimal DOA estimation performance.

5.5 Chapter summary

In this chapter, using the IES patterns of the TS-ENA and f-ENAMS-2 array, a new generalized ENAMS array has been proposed. The proposed GENAMS array has a closed-form expression for sensor position constrained by the IES term Q and N . Theoretical analysis demonstrates that the GENAMS array unifies the optimal segments of different sparse arrays as the number of sensors N increases. Furthermore, a detailed derivation of the GENAMS achievable uniform DOF and weight functions show that the proposed array achieves enhanced uniform DOF than existing ones with relatively low mutual coupling. Lastly, numerical examples verified that the GENAMS array offers improved uniform DOF and a high-resolution DOA estimation performance.

However, as observed in Fig. 5.8, a trade-off exists between the achievable uni-

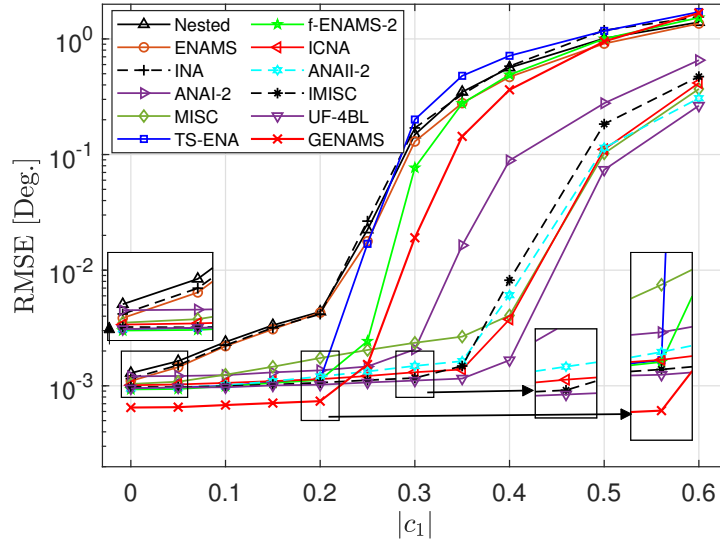


Figure 5.9: Comparison of RMSE versus $|c_1|$ for various sparse linear arrays.

form DOF and coupling leakage. Namely, as achievable uniform DOF increases, the coupling leakage tends to increase, although ideally, it was supposed to decrease due to the reduction of co-array redundancy. As such, researchers tend to focus on reducing mutual coupling or improving the achievable uniform DOF. Although the IES-based sparse linear arrays like MISC array and IMISC have managed to balance the two, there is still potential for such sparse arrays.

xMISC: Improved Sparse Linear Array via Maximum Inter-Element Spacing Concept

6.1 Introduction

So far, the design of sparse linear arrays has been approached from the perspective of enhanced degrees of freedom (DOF) for high-resolution DOA estimation. Although optimal DOF guarantees optimal DOA estimation performance, there is a limit at which the performance of sparse linear arrays deteriorates as the strength of mutual coupling (MC) increases. Eventually, the performance becomes dependent on the MC characteristics of the sparse linear array. Besides, as we have observed, in an effort to improve the uniform DOF, sparse linear arrays [48]-[57] were proposed, whereas as [59]-[66] have been developed to alleviate MC effects. Recently, a new family of sparse linear arrays [51], [64]-[66] that balance MC effects and DOF has been proposed via the maximum interelement spacing (MISC) criterion.

In Ref. [65], an enhanced version of MISC is introduced. This upgraded version comprises six ULA and offers better uniform DOF while minimizing mutual coupling effects. However, the difference co-array of the IMISC array still contains holes, making it less efficient. Therefore, in this study, we aim to improve IMISC by addressing the existing holes in its difference co-array. Here, we analyze the occurrence of these holes and present a simple strategy for recovering the missing virtual sensors without needing additional sensors. The proposed strategy involves manipulating the IES terms of the IMISC array [57], [65]-[66], [113], resulting in a new sparse array configuration herein called enhanced MISC array (xMISC)¹.

In this chapter, our main contributions include: i) We propose a new sparse linear array design called enhanced MISC array via a hole-filing strategy; ii) Derive detailed closed-form expressions for the xMISC array related to sensor locations, achievable

¹This chapter is based on S. Wandale and K. Ichige, “xMISC: Improved Sparse Linear Array via Maximum Inter-Element Spacing Concept,” *IEEE Signal Processing Letters*, vol. x, pp. xx-xx, 202x (under review).

DOF, and weight functions; iii) Finally, we provide numerical examples to illustrate the merits of the xMISC array in terms of achievable uDOF, coupling leakage, and accuracy of DOA estimation.

The remainder of this chapter is organized as follows. First, the conventional IMISC array from which the proposed xMISC array design is drawn is reviewed in Section 6.2. Then, the proposed hole-filling strategy and the proposed xMISC array design are discussed in Section 6.3 and 6.4, respectively. Next, section 6.5 examines different numerical examples to validate the performance of the proposed sparse array design. Lastly, concluding remarks are discussed in Section 6.6.

6.2 Conventional improved MISC array

In [65], a maximum interelement constrained (MISC) criterion-based sparse linear array called improved MISC (IMISC) was proposed. The improved MISC is expressed using an interelement spacing set \mathbb{Z}_i and a base term R that depends on the number of sensors N . Thus, the IMISC can be defined as

$$\mathbb{Z}_i = \left\{ \underbrace{2, \dots, 2}_{\frac{R}{4}-1}, 1, 1, \frac{R}{2} - 2, \underbrace{\frac{R}{2} - 1, \dots, \frac{R}{2} - 1}_{\frac{R}{4}-2}, \underbrace{R, \dots, R}_{N-R}, \frac{R}{2} + 1, \right. \\ \left. \underbrace{\frac{R}{2} + 1, \dots, \frac{R}{2} + 1}_{\frac{R}{4}-2}, \underbrace{2, 2, \dots, 2}_{\frac{R}{4}-1} \right\}, \quad (6.1)$$

where $R = 4\lfloor(N + 2)/6\rfloor$ for $N \geq 10$ [65]. The sensor location set corresponding to (6.1) is given as

$$\mathbb{Z}_i = \left\{ \begin{array}{l} \underbrace{0, \dots, \frac{R}{2} - 2}_{\mathbb{Z}_1}, \underbrace{\frac{R}{2} - 1, \frac{R}{2}}_{\mathbb{Z}_2}, \underbrace{R - 2, \dots, \frac{R^2}{8} - \frac{R}{4}}_{\mathbb{Z}_3}, \\ \underbrace{\frac{R^2}{8} + \frac{3R}{4}, \dots, NR - \frac{7R^2}{8} - \frac{R}{4}}_{\mathbb{Z}_4}, \\ \underbrace{NR - \frac{7R^2}{8} + \frac{3R}{4} + 1, \dots, NR - \frac{3R^2}{4} - \frac{R}{2} - 1}_{\mathbb{Z}_5}, \\ \underbrace{NR - \frac{3R^2}{4} - \frac{R}{2} + 1, \dots, NR - \frac{3R^2}{4} - 1}_{\mathbb{Z}_6}. \end{array} \right\}, \quad (6.2)$$

Compared to the MISC array [51], the IMISC array has enhanced uniform DOF and less mutual coupling effect [57], [64]-[66]. However, unlike the MISC array, the DCA of the IMISC array is incomplete due to the existence of holes or missing lags. Figure 6.1 (a)-(b), shows the array configuration of IMISC with $N = 10$ where $R = 8$, and its difference co-array. As shown in Fig. 6.1 (b), the difference co-array of the IMISC array contains holes at positions $\{30, -30\}$.

Furthermore, based on [65, Eq. 19], the DCA of the IMISC array is consecutive in the range

$$\left[-NR + \frac{3R^2}{4} + \frac{R}{2} - 1, NR - \frac{3R^2}{4} - \frac{R}{2} + 1\right]. \quad (6.3)$$

As such, compared to (6.1), the uniform DOF of the IMISC array has $(R - 4)$ fewer lags than its unique DOF, which is limiting considering that $(R - 4)$ grows as the number of sensors N increases. Inspired by this limitation, in the subsequent section, we analyze and identify the occurrences of holes in the IMISC array and derive a hole-filling strategy to recover the missing lags.

6.3 Hole analysis and filling strategy

This section first analyzes and identifies hole locations in the difference co-array of the IMISC array. Then, we develop a strategy to fill the holes by rearranging the interelement spacing terms of (6.1).

6.3.1 Hole Identification and Analysis

When comparing (6.1)-(6.3) with the DCA of the IMISC array [65, Appendix A], it becomes evident that the holes in the DCA of the IMISC array are located at specific positions of

$$\mathbb{H}_o = \pm\{NR - \frac{3R^2}{4} - \frac{R}{2} + i + 1 | 1 \leq i \leq \frac{R}{4} - 1\}, \quad (6.4)$$

where R is as defined in (6.1). Based on equation (6.4), it can be inferred that the holes in the DCA of the IMISC array are spaced at intervals of 2 starting from position $NR - \frac{3R^2}{4} - \frac{R}{2} + 2$. Additionally, it is worth noting that the total number of holes in the DCA of the IMISC array remains constant at $(R - 4)$, irrespective of the value of N .

6.3.2 Hole filling strategy

In accordance with [57], [64]-[66], we reformulated and summarized (6.1) into a more concise format for clarity and ease of understanding. Thus, \mathbb{M}_i can be expressed as

$$\mathbb{M}_i = \{2^{m-1}, 1^2, (\mathcal{T} - 2), (\mathcal{T} - 1)^{l-2}, R^v, (\mathcal{T} + 1)^{m-1}, 2^m\}, \quad (6.5)$$

where $R = 4\lfloor(N + 2)/6\rfloor$, $v = N - R$, $\mathcal{T} = R/2$ and $m = R/4$. In this new format, we can treat the IMISC array as a minimum redundancy array. When it comes to the MRA, it is possible to create a new configuration using (6.5) by either updating or reproducing the highest IES or the primary term [57], [65]-[66]. Another option is to modify the powers of the IES terms on each side of the primary term to achieve a new configuration [113].

Utilizing the conditions above, we eliminate one IES term from the second one. Then, we add the third to the fourth term to equalize the power between the fourth

and sixth terms. As a result, (6.5) is adjusted as

$$\mathbb{L}_e = \{2^{m-1}, 1, (\mathcal{T} - 1)^{m-1}, R^v, (\mathcal{T} + 1)^{m-1}, 2^m\}, \quad (6.6)$$

where R, \mathcal{T}, m and v are as expressed in (6.5) except that the total number of sensors is $N - 1$ instead of N . Moreover, the corresponding sensor locations set is given by

$$\begin{cases} \mathbb{L}_1 = \{2q_1 | 0 \leq q_1 \leq m - 1\} \\ \mathbb{L}_2 = 2m - 1 \\ \mathbb{L}_3 = \{2m + (\mathcal{T} - 1)q_2 - 1 | 1 \leq q_2 \leq m - 1\} \\ \mathbb{L}_4 = \{Ri + m(\mathcal{T} + 1) - \mathcal{T} | 1 \leq i \leq v\} \\ \mathbb{L}_5 = \{Rv + m(\mathcal{T} + 1) + (\mathcal{T} + 1)q_2 - \mathcal{T}\} \\ \mathbb{L}_6 = \{Rv + 2\mathcal{T}(m - 1) + 2m + 2q_3 - 1 | 1 \leq q_3 \leq m\}. \end{cases} \quad (6.7)$$

In the example illustrated in Figure 6.1 (c)-(d), an \mathbb{L}_e configuration is depicted with parameters $N = 10, R = 8, v = 2, \mathcal{T} = 4$, and $m = 2$. It is worth noting that despite the aperture remaining intact, four new holes have appeared at positions $\{-10, 10\}$ and $\{-18, 18\}$.

Next, based on (6.7) the holes in (6.6) are located at

$$\mathbb{H}_1 = \pm\{Rv + 2\mathcal{T}(m - 1) + 4m - 2i_1 | 1 \leq i_1 \leq m - 1\}, \quad (6.8)$$

and

$$\mathbb{H}_2 = \pm\{R(v - i_2) + \mathcal{T}(m - 1) + 3m | 1 \leq i_2 \leq v - 1\}, \quad (6.9)$$

As a result, similar to (6.4), the number of holes in \mathbb{H}_1 and \mathbb{H}_2 are determined by $m - 1$ and $v - 1$, respectively. By utilizing the extra sensor from (6.6) and positioning it at $d_m = Rv + 2\mathcal{T}(m - 1) + 4m$ in \mathbb{L}_e , we can effectively fill in the holes in \mathbb{H}_1 and \mathbb{H}_2 , i.e.,

$$d_m - d_{\mathbb{L}_1} = \{Rv + 2\mathcal{T}(m - 1) + 4m - 2i_1 | 1 \leq i_1 \leq m - 1\}, \quad (6.10)$$

and

$$d_m - d_{\mathbb{L}_4} = \{R(v - i_2) + \mathcal{T}(m - 1) + 3m | 1 \leq i_2 \leq v - 1\}. \quad (6.11)$$

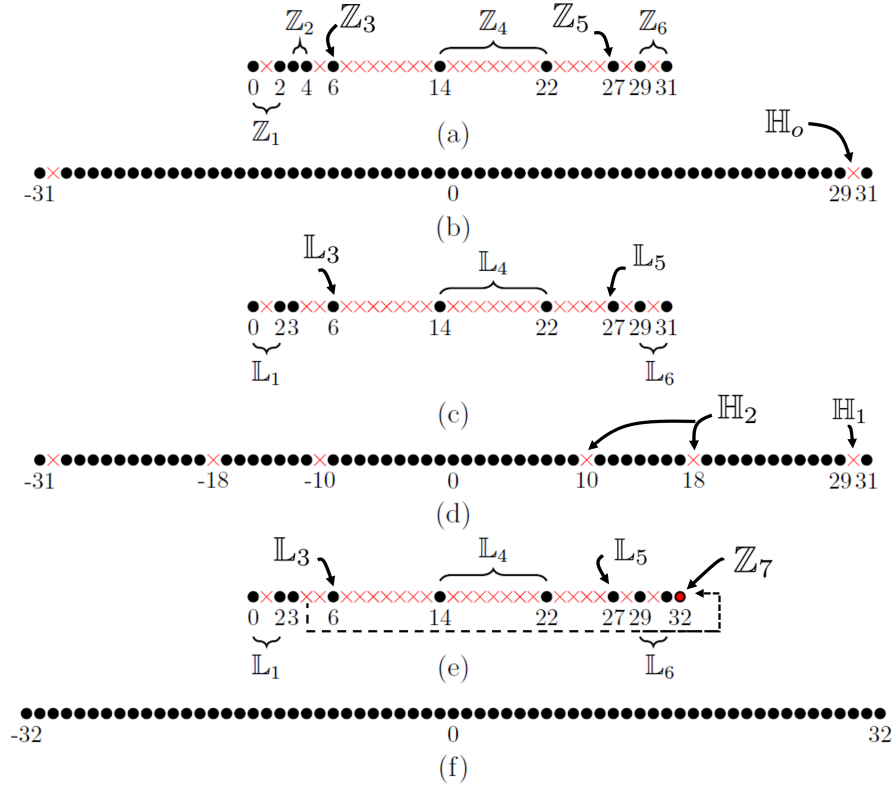


Figure 6.1: Comparison of sparse linear array configurations and their difference co-arrays. (a) Improved MISC array and (b) its difference co-arrays where \mathbb{H}_o is the location set of holes. (c) Relaxed IMISC and (d) its difference co-array where \mathbb{H}_1 and \mathbb{H}_2 denote the 1st and 2nd set of holes, respectively. Finally, (e) Enhanced MISC array where the dotted line represents sensor relocation and (f) its difference co-array.

6.4 Proposed enhanced MISC array design

Following the hole-filling strategy in Section 6.3.2, we propose an enhanced maximum interelement spacing constrained (xMISC) array. Like the IMISC and MISC array, the xMISC array is designed using an interelement spacing set \mathbb{L}_m and the maximum interelement spacing term Q . Specifically, the xMISC array can be expressed as

$$\mathbb{L}_m = \{2^{m-1}, 1, (\mathcal{T} - 1)^{m-1}, R^v, (\mathcal{T} + 1)^{m-1}, 2^m, 1\}, \quad (6.12)$$

where $R = 4\lfloor(N+2)/6\rfloor$, $v = N - R$, $\mathcal{T} = R/2$ and $m = R/4$. And the corresponding sensor locations can be given as

$$\begin{cases} \mathbb{L}_1 = \{2q_1 | 0 \leq q_1 \leq m - 1\}, \\ \mathbb{L}_2 = 2m - 1, \\ \mathbb{L}_3 = \{2m + (\mathcal{T} - 1)q_2 - 1 | 1 \leq q_2 \leq m - 1\}, \\ \mathbb{L}_4 = \{Ri + m(\mathcal{T} + 1) - \mathcal{T} | 1 \leq i \leq v\}, \\ \mathbb{L}_5 = \{Rv + m(\mathcal{T} + 1) + (\mathcal{T} + 1)q_2 - \mathcal{T}\}, \\ \mathbb{L}_6 = \{Rv + 2\mathcal{T}(m - 1) + 2m + 2q_3 - 1 | 1 \leq q_3 \leq m\} \\ \mathbb{L}_7 = Rv + 2\mathcal{T}(m - 1) + 4m. \end{cases} \quad (6.13)$$

where sets \mathbb{L}_i for $i \in [1, 7]$ chronologically correspond to the IES terms as expressed in (6.12).

Figure 6.1 (e)-(f) shows an example of xMISC array configuration with $N = 10$ sensors where $R = 8, v = 2, \mathcal{T} = 4$ and $m = 2$. As shown in Fig. 6.1 (f), the additional sensor at \mathbb{L}_7 filled the holes in \mathbb{H}_1 and \mathbb{H}_2 . Thus, the xMISC retains a hole-free DCA. In the following, we formally summarize the property of the xMISC array.

Property 6.4.1. Given $R = 4\lfloor(N+2)/6\rfloor$ for $N \geq 10$, the difference co-array of the xMISC array is a hole-free, i.e., $\mathbb{D} = [-L_u, L_u]$ such that $Rv + 2\mathcal{T}(m - 1) + 4m$.

Proof. See Appendix D (8.2). □

And, based on Property 6.4.1, we derive the following property.

Property 6.4.2. Given that $R = 4\lfloor(N+2)/6\rfloor$, $v = N - R$, $\mathcal{T} = R/2$, and $m = R/4$. The uniform DOF of the xMISC array is $(2N^2 - 5)/3$ for $N \geq 10$.

Proof. Utilizing Property 6.4.1 and (6.12), it follows that

$$\text{uDOF} = 2L_u + 1 \approx 2Rv + 4\mathcal{T}(m - 1) + 8m + 1, \quad (6.14)$$

Plugging in R , v and m as given in (6.12) into (8.13) returns

$$\text{uDOF} = 2RN - \frac{3R^2}{2} + 1 \approx \frac{2N^2 - 5}{3}, \quad (6.15)$$

and, therefore, completes the proof. \square

Concerning the weight functions, based on (6.12), the first three weight functions of the xMISC array are

$$w(1) = 2, \quad w(2) = \frac{R}{2} - 1, \quad w(3) = 2. \quad (6.16)$$

Obviously, these weights are closer to those of MISC [51] and IMISC [65] but higher than those of the ICNA [59], and SNA [44], [72].

6.5 Numerical examples

In this section, numerical examples are provided to verify the effectiveness of the xMISC array. The DOA estimation is conducted using SS-MUSIC [33], and the accuracy is measured by the root mean-square-error (RMSE) of the estimated DOA (averaged over 1000 trials). Here, these parameters remain constant: 28 sensors are used for all arrays, with mutual coupling factors of $c_1 = 0.2e^{j\pi/3}$, and $c_k = c_1 e^{-j(k-1)/8}/k$, where $k \in [2, 100]$. The number of snapshots is 1000, and the SNR ranges from -30 to 10 dB.

6.5.1 DOF capacity and mutual coupling analysis

Let us begin by comparing the DOF capacity of the xMISC array with other sparse arrays using the DOF ratio. As depicted in Fig. 6.2, the NA has the lowest DOF

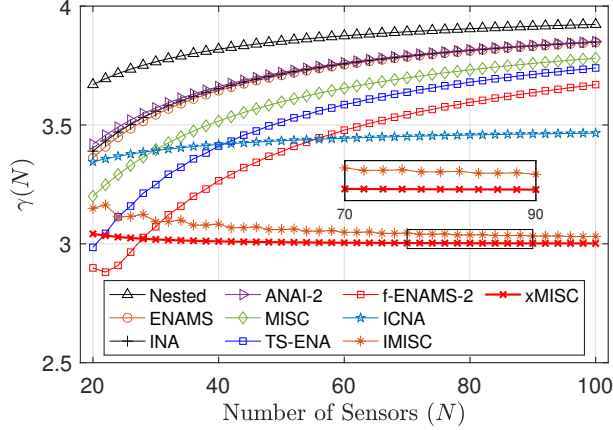


Figure 6.2: Performance of the xMISC array in terms of the DOF ratio $\gamma(N)$.

capacity, whereas the xMISC array has the highest, and above it, is the DOF ratio of the original IMISC array. In contrast, the $\gamma(N)$ values of other sparse arrays lie between those of the NA and the xMISC array. Moving on, the plot of coupling leakage against the number of sensors is shown in Fig. 6.3. The ICNA has the least coupling leakage values, followed by IMISC and xMISC. The IMISC and xMISC arrays retain $w(1) = 2$, so the overall coupling leakage values remain fairly consistent. However, the xMISC array achieves higher DOF than the IMISC array.

Alternatively, we can illustrate the performance of the xMISC array in joint DOF and reduced mutual coupling. Thus, we evaluate the DOF and mutual coupling leakage jointly. Accordingly, the optimal sparse linear array should satisfy (6.17), which forms a feasible region in the 2D plane as shown in Fig. 6.4, i.e.,

$$\gamma(N) \leq 3.25 \text{ and } L(N) \leq \frac{1}{3}. \quad (6.17)$$

As shown in Fig. 6.4, the DOF ratio and coupling leakage of the xMISC array is 0.2 and 0.13, respectively, and all are within the feasible region. On the contrary, However, other sparse linear arrays are not located in the feasible region except for the IMISC, TS-ENA, and f-ENAMS-2 array.

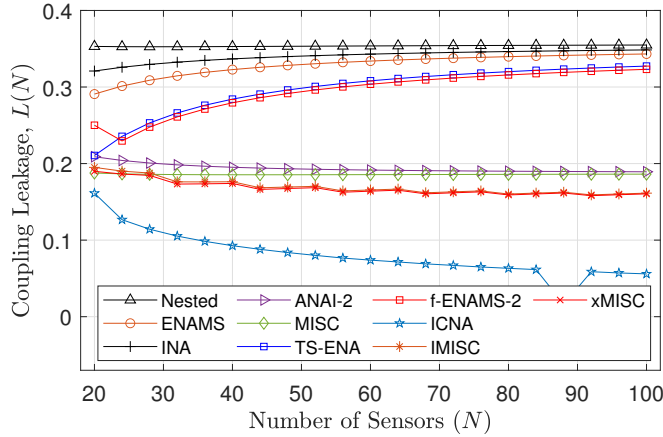


Figure 6.3: Performance of the xMISC array in terms of the coupling leakage $L(N)$.

6.5.2 RMSE of DOA estimation in the presence of MC

Finally, we evaluate the DOA estimation performance of the proposed XMISC array. The RMSE versus the input SNR is computed when $P = 40$ sources are located at $\bar{\theta}_p = -0.4 + 0.8(p - 1)/39$ for $p \in [1, 40]$. According to Fig. 6.5, NA performs poorly due to limited DOF. However, the performance of the xMISC array outperforms other sparse arrays. Thus, the enhanced DOF of the xMISC array improves its DOA estimation resolution. Next, we computed the RMSE versus mutual coupling coefficient $|c_1|$. In this example, with all parameters constant, we vary the value of $|c_1|$ from 0 to 0.6. The results are depicted in Fig. 6.6 as a plot of RMSE versus $|c_1|$. It is clear from Fig. 6.6 that the proposed xMISC array outperforms other sparse arrays when $c_1 \leq 0.4$. As $|c_1|$ increases, the performance of the xMISC array degrades. However, the performance is still better than those of the MISC, ICNA, and other sparse arrays.

6.6 Chapter summary

This chapter introduced an enhanced MISC array design via a hole-filling strategy (xMISC). This strategy manipulates the interelement spacing terms of the IMISC array, thereby eliminating the need for extra sensors. The proposed xMISC array has closed-form expressions for sensor positions and retains a hole-free DCA. Numerical

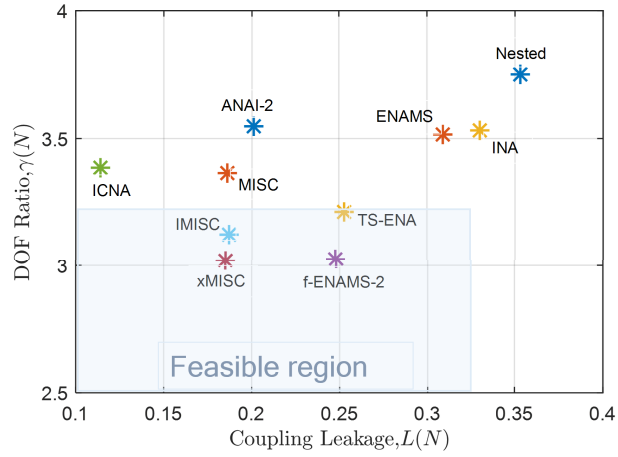


Figure 6.4: Comparison of the DOF ratio and coupling leakage for different arrays.

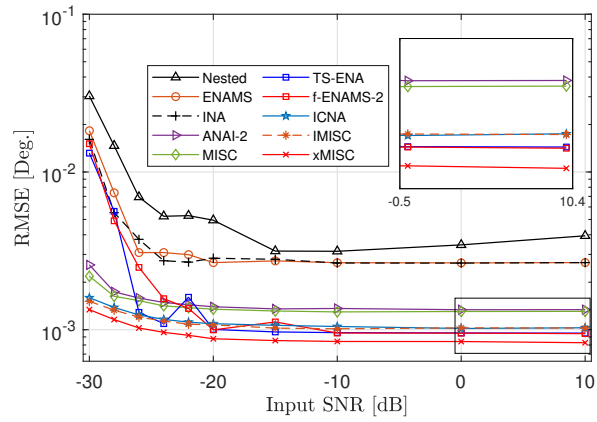


Figure 6.5: Performance of the xMISC array in terms of the RMSE versus SNR.

examples demonstrated that the xMISC array improves uniform DOF and high-resolution DOA estimation performance.

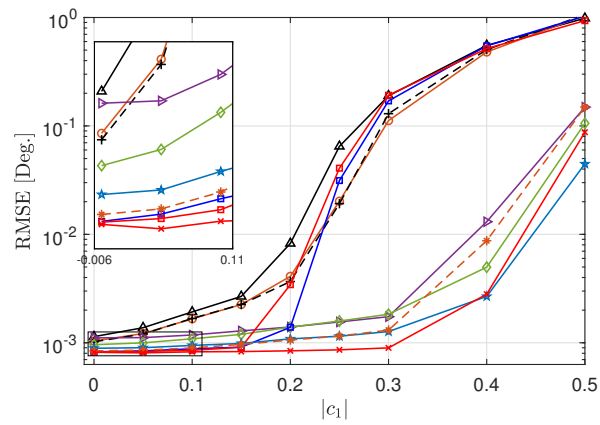


Figure 6.6: Performance of the xMISC array in terms of the RMSE versus $|c_1|$.

Sparse Array Design via Deep Learning: Trade-Offs Analysis

7.1 Introduction

Recently, antenna array design has witnessed a dynamic shift from traditional (ad-hoc, analytical, and heuristic) methods to cognitive machine learning-based approaches, especially regarding sparse arrays. As highlighted in previous chapters 3-6, sparse or non-uniform arrays offer many unique advantages, including reduced mutual coupling, enhanced resolution, and cost-effectiveness [42]-[72]. However, their optimal design remains challenging due to the vast solution space and complexity of achieving the desired performance characteristics such as reduced mutual coupling (MC) effect, hole-free difference co-array, reduced redundancy, trimmed sidelobe levels (SLLs), and many more [83]-[90]. Therefore, a successful design depends on the method used and the choice of the objective function or desired performance characteristics.

Concerning the sparse array design approaches, the ad-hoc methods are most recognized and are typically based on trial and error as well as prior experience (expert knowledge). As such, they might not guarantee optimal solutions but are usually easy to implement and understand. For example, one common ad-hoc approach is to manually adjust the antenna elements' positions until the desired performance is achieved. This is portrayed in the design of well-known sparse arrays like NA [9], CA [10], MISC [51], and many more [8], [15], [42]-[72]. Another limitation of ad-hoc approaches is that the method becomes infeasible as the array size increases due to the exponentially growing solution space [83]. Therefore, to work around this problem, closed-form expressions are used to generate any sparse array of that pattern given any number of sensors N [42]-[43], [48]¹.

¹This chapter is based on S. Wandale and K. Ichige, "Simulated annealing assisted sparse array selection utilizing deep learning," *IEEE Access*, vol. 9, pp. 156907-156914, 2021, doi:10.1109/ACCESS.2021.3129856.

On the other hand, heuristic methods leverage optimization algorithms to explore the solution space systematically [91]. One of the popular heuristic techniques is the simulated annealing (SA) algorithm, a probabilistic method for finding the global minimum of a function. The SA algorithm reasonably compromises computational efficiency and solution quality by avoiding local minimum traps. However, the SA algorithm still requires substantial computational resources and time, particularly for large-scale problems [83], [90]-[94].

In contrast to ad-hoc and heuristic methods, machine learning (ML) techniques have the potential to solve large-scale sparse array design problems more efficiently. Specifically, deep learning (DL) algorithms have shown promise due to their ability to model complex, non-linear relationships and handle high-dimensional data [107]-[109]. For example, one recent approach uses a two-stage DL-based sparse array selection method, comprising an initialization step using the SA algorithm to generate sparse array configurations for the construction of the dataset, then training a convolutional neural network (CNN) model on this data [91]. This approach offers the advantage of requiring fewer data samples to realize data labels, significantly reducing computational costs and time in the process. Moreover, the trained CNN model can provide optimal solutions with reduced computation time compared to the conventional SA-based optimization approach [83], [91]-[94]. Besides, it does so without needing an expert, as the ad-hoc method requires [42].

This chapter explores and elucidates the trade-offs between the heuristic and ML-based sparse array design approaches. Specifically, we consider the SA-based method proposed in [92]-[94] and the SA-assisted DL array design method demonstrated in [92]. The fundamental trade-offs of interest in this chapter involve the consideration of a balance between computational efficiency and solution quality when choosing a sparse array design method. In the context of DOA estimation, we explore the trade-off where the quality is evaluated in the form of accuracy or DOA estimation performance of a sparse array design by each method above.

This chapter is organized as follows: Section 7.2 introduces a sparse array design problem as an antenna selection or array thinning problem. Then, Section 7.3 discusses different sparse array design methods and their unique solutions. Next, Section 7.4 examines the trade-offs of the two techniques in light of the sparse arrays

designed. Finally, Section 7.5 concludes the chapter.

7.2 Antenna selection and sparse array design

Antenna selection and sparse array design are crucial aspects of wireless communication systems, focusing on antennas' optimal arrangement and utilization to maximize signal reception and transmission. However, these processes have to account for various elements such as signal strength, interference, power efficiency, and physical constraints, thereby increasing the complexity of the problem space [97]-[107]. In antenna selection, the main objective is to choose the best subset of antennas from a larger set to optimize system performance based on specific criteria, such as SNR, channel capacity, or energy efficiency. This selection problem can be expressed as

$$\mathbb{S}_{op} = \max_{\mathbb{S}_i \subseteq \{1, 2, \dots, N\}, |\mathbb{S}_i|=M} F(\mathbf{S}) \quad (7.1)$$

where $F(\mathbf{S})$ represents the objective function (e.g., SNR, channel capacity), N is the total number of antennas, \mathbb{S}_{op} is the selected subset, and M is the number of antennas to be selected. The complexity of this problem arises from its combinatorial nature; with a large number of potential combinations, i.e.,

$$\mathcal{Q} = \binom{N}{M} = \frac{N!}{M!(N-M)!}. \quad (7.2)$$

Therefore, identifying the optimal subset becomes computationally demanding and is often classified as an NP-hard problem, implying no known algorithm can solve it in polynomial time [83]-[91].

On the other hand, sparse array design pertains to the optimal arrangement of a limited number of antennas M in a larger space N to optimize specific performance metrics such as the array's directivity, SSLs, or spatial resolution. Thus, although not explicitly equivalent to antenna selection, the two are used interchangeably, yielding almost the same problem space, i.e., \mathcal{Q} combinations. The problem space here is massive due to the many ways antennas can be arranged, resulting in high computational complexity [13]-[16], [103].

As highlighted in Section 7.1, different techniques have been developed over the

decades to address these problems, ranging from classical ad-hoc [42]-[72], [108]-[113] to recently harnessed machine learning methods [85], [87]-[91], [106]-[109]. However, despite the pros and cons of these methods, these tasks (antenna selection and sparse array design) remain vital in developing and operating modern wireless communication systems [1]-[7]. Therefore, this chapter explores the pros and cons of these methods, especially the trade-off between computational complexity and accuracy, in order to foster balanced and informed decisions when selecting sparse array design methods. In the sections that follow, we briefly review two different sparse array design approaches: i) traditional heuristic methods [92]-[94]; and iii) contemporary ML techniques [90]-[91].

7.3 Review of sparse array design

In this section, we will be examining two distinct approaches to sparse array design that we plan to use for trade-off analysis. The third method, ad-hoc, since the computation complexity of the ad-hoc method cannot be accurately measured, we will be focusing our analysis on the ML-based method in Section (7.3.1) and the traditional heuristic methods in Section (7.3.2). To simplify matters, we will be using the SA method [92] and the SA-assisted DL-based method [91] as representatives of the heuristic and ML-based approaches, respectively.

7.3.1 Heuristic optimization methods

As discussed in Section 2.4, in [92]-[94], a simulated annealing-based planar array (SAPSA) was studied with the aim of reducing the mutual coupling in an hourglass array (HA) [95]. Starting with the HA with N sensors as an initial array, i.e., \mathcal{Z}_i , the SAPSA can be realized by solving the following problem

$$\begin{aligned} \mathbb{S}_{sa} = \operatorname{argmax}_{\mathbb{S}_i} & \sum_{i=1}^N \sum_{j=i+1}^N \frac{1}{\|n_i - n_j\|_2}, \\ \text{s.t.} & \|n_i - n_j\|_2 \leq B, \end{aligned} \tag{7.3}$$

where $n_{i,j} \in \mathcal{Z}_i$, N is the number of sensors and $\|\cdot\|_2$ is the l_2 -norm of a vector. Additionally, B is the upper-bound coefficient of mutual coupling [48], [92]. Thus, the problem in (7.3) aims at optimizing the sensor positions in \mathcal{Z}_i while minimizing the mutual coupling between sensors, i.e., $\sum_{i=1}^N \sum_{j=i+1}^N \frac{1}{\|n_i - n_j\|_2}$ [92].

In this context, the SA algorithm can realize a sparse array with desired aperture and well-distributed sensors while navigating around such a big problem space as \mathcal{Q} . Below, we summarize the optimization stages of the SA algorithm:

- (a) The initialization stage requires \mathcal{Z}_i the initial 2D array with N sensors, and other parameters, including initial temperature β_o , permitted number of holes in the DCA η , and objective function κ .
- (b) Then, at each iteration it perturbs the \mathcal{Z}_i while maintaining the number of permitted holes η in the DCA of \mathcal{Z}_{in} [92]. Therefore, using the current temperature β , the acceptance probability function $\rho(\Delta\kappa, \beta)$ of current solutions is given as

$$\rho(\Delta\kappa, \beta) = \begin{cases} e^{-\Delta\kappa/\beta}, & \text{if } \Delta\kappa > 0 \\ 1, & \text{otherwise} \end{cases} \quad (7.4)$$

where $\Delta\kappa = \kappa_n - \kappa_{n-1}$ such that κ_n and κ_{n-1} denote objective functions of the new and the previous solutions, respectively. Thus, the solution is accepted if the new κ is smaller than the preceding one. Otherwise, the temperature is decreased, discard poor solutions discarded, and the algorithm iterate.

Note that β is decreased using a cooling schedule which is determined by a coefficient α . Therefore, using β_o , at i -th iteration the temperature becomes

$$\beta = \beta_o \cdot \alpha^i. \quad (7.5)$$

The operation in (7.5) is repeated at each iteration until the algorithm converges to a global minimum. The smaller the $\Delta\kappa$, the higher the temperature. Furthermore, cooling down the temperature slowly slows down the convergence rate. Therefore, it is essential to select a higher value of β_o to escape from the local minimum and an optimal value of α to increase the chances of obtaining a global optimum [31], [92].

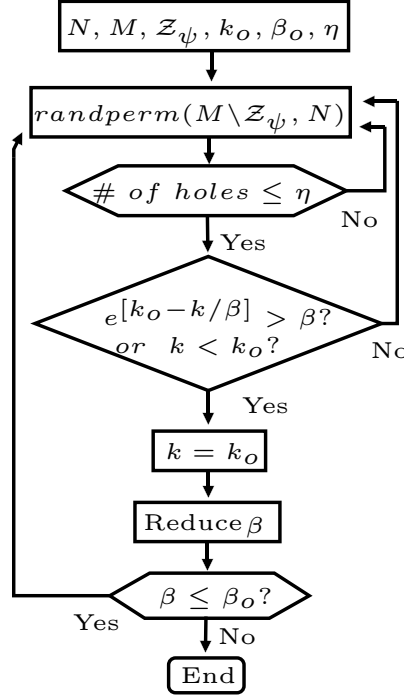


Figure 7.1: (a) The flow diagram of simulated annealing algorithm for optimization of HA.

Figure 7.1 summarizes the above stages in a generalized flow diagram [91]. Note that this SA algorithm can be extended to other 2D arrays other than HA.

7.3.2 Machine learning methods

Unlike heuristic methods, ML-based methods have become attractive due to their low computation complexity once online (after being trained offline and deployed). At this stage, the ML models require less time to converge to a near-optimal solution. Besides, they are robust to uncertainties and can transfer features between models or tasks, i.e., transfer learning. So far, different methods, such as support vector machines (SVM) and artificial neural networks (NN) [84], have been proposed to predict sparse linear array configurations. In addition, DL-based approaches have also been proposed to tackle the 2D array design problem in [85]-[88]. However, these problems depend on Q or its partial form to construct meaningful datasets and

ground truth, which is computationally costly and often yields biased representation. Hence, in [91], an SA-assisted DL-based model was proposed to circumvent the above problem. Overall, machine learning is a new and promising approach as far as sparse array design is concerned. In the next paragraph, we discuss the SA-assisted DL-based sparse array design approach to demonstrate the use of ML in sparse array design [91].

Performance criterion: Like any other optimization problem, knowing the objective function simplifies the design process of the algorithm. Here, the performance metric must be known to generate meaningful target or ground truth data for the ML model. For simplicity, we assume Cramer-Rao bound (CRB) as a metric [24]-[26], [85]. In what follows, we derive the closed-form expression of the CRB.

Utilizing (2.15) from Section 2.2.4, the partial derivative of $\mathbf{A}(\Theta)$ with respect to θ and ϕ can be expressed as $\mathbf{b}(\theta_k) = \frac{\partial}{\partial \theta_k} \mathbf{A}(\theta_k)$ and $\mathbf{b}(\phi_k) = \frac{\partial}{\partial \phi_k} \mathbf{A}(\phi_k)$ respectively for $k = 1, 2, \dots, K$ such that $\mathbf{B}_\theta = [\mathbf{b}(\theta_1), \mathbf{b}(\theta_2), \dots, \mathbf{b}(\theta_K)]$ and $\mathbf{B}_\phi = [\mathbf{b}(\phi_1), \mathbf{b}(\phi_2), \dots, \mathbf{b}(\phi_K)]$ respectively [85]. As such, the CRB with respect to θ and ϕ can be defined as

$$\mathcal{C}_\theta = \frac{\sigma_n^2}{2T} \Re \left[\mathcal{I}_\theta \odot (\mathbf{R}_s \mathbf{A}^H(\Theta) \mathbf{R}^{-1} \mathbf{A}(\Theta) \mathbf{R}_s)^T \right], \quad (7.6)$$

$$\mathcal{C}_\phi = \frac{\sigma_n^2}{2T} \Re \left[\mathcal{I}_\phi \odot (\mathbf{R}_s \mathbf{A}^H(\Theta) \mathbf{R}^{-1} \mathbf{A}(\Theta) \mathbf{R}_s)^T \right], \quad (7.7)$$

where

$$\mathcal{I}_\theta = \mathbf{B}_\theta^H \left[\mathbf{I} - \mathbf{A}(\Theta) (\mathbf{A}^H(\Theta) \mathbf{A}(\Theta))^{-1} \mathbf{A}^H(\Theta) \right] \mathbf{B}_\theta,$$

$$\mathcal{I}_\phi = \mathbf{B}_\phi^H \left[\mathbf{I} - \mathbf{A}(\Theta) (\mathbf{A}^H(\Theta) \mathbf{A}(\Theta))^{-1} \mathbf{A}^H(\Theta) \right] \mathbf{B}_\phi,$$

respectively [10], [17]. Combining (7.6) and (7.7) yields

$$\mathcal{C}(\Theta) = \frac{1}{\sqrt{2}} \left[\mathcal{C}_\theta^2 + \mathcal{C}_\phi^2 \right]^{\frac{1}{2}}, \quad (7.8)$$

assuming that the SNR is expressed as $10 \log_{10}(\sigma_s^2/\sigma_n^2)$ [85]. Therefore, using (7.8) the DOA estimation performance of a sparse array \mathbb{S}_i given that the signal information is known prior [84]-[91].

Ground truth construction: Next, given a range of DOA sources and (7.8),

conventional ML-based methods employ simple search methods to select subarrays with the best CRB values as ground truth for different subarrays depending on the DOAs. However, searching through \mathbf{Q} is computationally expensive. To work around this problem, in [91], two simple modifications were proposed as summarized in Fig. 7.1 as follows: i) a condition was added to maintain all corner sensors, i.e., \mathcal{Z}_ψ ; and ii) a loop was added after step (b) so that sparse arrays \mathbb{S}_t for $t \in T$, are generated for T trials. Therefore, the realized sample matrix \mathbf{T} is not only more manageable than \mathbf{Q} but also contains array samples with desired sparse array conditions [87], [90]-[91].

In this context, the simple search algorithm can be expressed as

$$\mathbf{U}_T = \underset{\mathbb{S}_t, t \in T}{\operatorname{argmin}} \mathcal{C}(\Theta, \mathbb{S}_t), \quad (7.9)$$

Accordingly, the resulting ground truth matrix \mathbf{U}_T is much smaller than \mathbf{U}_Q due to the similarities in array configurations and responses to various DOAs [84], [88].

Dataset construction: Now, having established the sample and the ground truth generation stages, in this section, we put together all the components into a single algorithm. Given the total number of sensors N , the number of sensors to be selected M , the number of snapshots \mathcal{T} , the number of different DOA angles K , the input SNR, and the sample array matrix \mathbf{T} . First, P signals are realized for different $|\mathbf{T}|$ arrays. Thus, the signals are used to construct covariance matrices, i.e., $\mathbf{R}_{xx,t}, \forall t \in T$ [95], [91].

Before we proceed, note that the input data is $N \times N \times 3$ real-valued matrices $\{\mathbf{H}\}_{i=1}^3$ whose (i, j) -th entry consists of $[\mathbf{H}_1]_{i,j} = \angle[\mathbf{R}]_{i,j}$, $[\mathbf{H}_2]_{i,j} = \operatorname{Re}[\mathbf{R}]_{i,j}$ and $[\mathbf{H}_3]_{i,j} = \operatorname{Im}[\mathbf{R}]_{i,j}$ denoting the phase, real and imaginary components of a sample covariance matrix $\mathbf{R}_{xx,t}$ [95], [88]. Next, in a parallel setup, (7.9) is applied to the realized covariance matrices to generate the ground truth data. Since the resulting data is used for training purposes, the SNR used in this process is denoted as $\operatorname{SNR}_{\text{TRAIN}}$. Lastly, the input-output data pairs (or input-target pairs) are computed as (\mathbf{H}_t, u_t) such that $u_t \in \mathbf{U}_t$ is the output label that represents the best subarray given $\mathbf{R}_{xx,t}$ as the input. The above steps are summarized in the Algorithm 1.

Deep learning model: For objective comparison, we adopt a general CNN structure consisting of 8 layers as in [85]. In general terms, the first layer (1st layer)

Algorithm 1 Proposed training dataset generation method

Input: Given N, M, T, K, P and $\text{SNR}_{\text{TRAIN}}$

Output: Training data $\mathcal{D}_{\text{TRAIN}}$

- 1: Generate \mathbf{T} as shown in Fig. 7.1 (b).
 - 2: Sample K DoA angles $\{\Theta_k\}_{k=1}^K$.
 - 3: Compute P different realizations of subarray output, $\{\mathbf{X}_k^i\}_{i=1}^P$ for $k \in [1, K]$
such that $\mathbf{X}_k^i = [\mathbf{x}_k^i(1), \mathbf{x}_k^i(2), \dots, \mathbf{x}_k^i(T)]$,
where $\mathbf{x}_k^i(t) = \mathbf{a}(k)\mathbf{s}^{(i)}(t) + \mathbf{n}^{(i)}(t)$, $\mathbf{s}^{(i)}(t) \sim \mathcal{CN}(0, \sigma_s^2 \mathbf{I})$ and $\mathbf{n}^{(i)}(t) \sim \mathcal{CN}(0, \sigma_n^2)$
 - 4: Calculate covariance matrix $\hat{\mathbf{R}}$ and $M \times M$ matrices $\mathbf{R}_t^{(i,k)}, \forall t \in \mathbf{T}$.
 - 5: Compute $\mathcal{C}(\Theta, \mathbf{S}_t) \forall t \in \mathbf{T}$ and select labels following (7.9).
 - 6: Create input-output data pairs as $(\hat{\mathbf{R}}^{(i,k)}, u_k^{(i)})$ for $k = 1, 2, \dots, K$ and for $i = 1, 2, \dots, P$.
 - 7: Connect the input-output pairs to form the training dataset as
$$\mathcal{D}_{\text{TRAIN}} = [(\hat{\mathbf{R}}^{(1,1)}, u_1^{(1)}), (\hat{\mathbf{R}}^{(2,1)}, u_1^{(2)}), \dots, (\hat{\mathbf{R}}^{(P,1)}, u_1^{(P)}), (\hat{\mathbf{R}}^{(1,2)}, u_2^{(1)}), \dots, (\mathbf{R}^{(P,K)}, u_K^P)]$$
where the size of the training dataset is $\mathcal{R} = PK$.
-

accepts the 2D input, and the last output layer (8th layer) is a classification layer with \mathbf{l} units where a softmax function is used to obtain the probability distribution of the classes [90]. The second (2nd layer) and the fourth (4th layer) layers are max-pooling layers with 2×2 kernel to reduce the dimension whereas the third (3rd layer) and the fifth (5th layer) layers are convolutional layers with 64 filters of size 2×2 .

Finally, the seventh (7th layer) and the eighth (8th layer) layers are fully connected layers with 1024 units. Note, the rectified linear units (ReLU) are used after each convolutional and fully connected layer such that $\text{ReLU}(x) = \max(x, 0)$ [11]. During the training phase: 90 % and 10 % of the data are allocated for training and validation purposes. The stochastic gradient descent with momentum (SGD) is used with a learning rate of 0.03 and a mini-batch of 500 for 50 epochs [91].

Implementation example: In this section, using a URA with 42 sensors, we generate two distinct training datasets using the conventional method [85] and the SA-assisted approach [91]. We randomly sample 10000 subarrays for the former and employ the SA-based optimization method for the latter. To realize classes \mathbf{T} using the SA-based algorithm, we assume the following parameters: $\eta = 0$, $\beta = 1000$, $\beta_o = 0.0001$ and κ_o is as in (7.3). We sample $K_\phi = 120$ DOAs uniformly within the range of $[0^\circ, 360^\circ)$ whereas K_θ was fixed at 90° . Furthermore, for each dataset, we

Table 7.1: Realized training data for various techniques

(N, M)	Sets	Data generation techniques	
		Conventional DL (\mathbf{Q})	SA-assisted DL (\mathbf{T})
(42, 16)	Samples	10000	4000
	Labels	34	37

assume 10 dB $\text{SNR}_{\text{TRAIN}}$ and 100 snapshots.

Table 7.1 summarizes the data samples and their corresponding ground truth. As shown in Table 7.1, the number of labels generated by the SA-assisted method almost tally with those realized using the conventional method despite using a small number of samples compared to the conventional approach. Thus, the proposed initialization step achieves large label samples from a small predefined generated dataset compared to the conventional method. Thus, the SA-assisted approach considerably reduces computation costs [91].

Next, using the generated dataset, we evaluate the trained CNN model in three ways. In example #1, we test the CNN model with the data generated using parameters shown in Table 7.2 to predict sparse 2D arrays. The predicted sparse array is depicted in Fig. 7.2. Specifically, Fig. 7.2 (a) shows the parent 42-element URA whereas Fig. 7.2 (b)–(c) show the predicted 16-element DL-based 2D sparse array using the conventional and SA-assisted method, respectively. As shown in Fig. 7.2, the SA-assisted method yields a 2D sparse array with a larger physical aperture compared to the conventional DL-based sparse array.

In the second example (example #2), we evaluate the sparse array design approaches in terms of RMSE performance of DOA estimation. For this experiment, we assume simulation parameters in the third column of Table 7.2. The realized sparse arrays from CNN are fed to a MUSIC algorithm [24]–[26] for DOA estimation purposes. In this scenario, the SNR_{TEST} is varied from -20 dB to 10 dB over 100 number of trials. The RMSE is calculated as,

$$\text{RMSE} = \sqrt{\frac{1}{\mathcal{T}K} \sum_{i=1}^{\mathcal{T}} \sum_{k=1}^K (\tilde{\phi}_k^i - \phi_k)^2}, \quad (7.10)$$

Table 7.2: Simulation parameters for estimation performance evaluation

Parameters	Simulation examples		
	Example #1	Example #2	Example #3
(N, M)	(42, 16)		
# of trials, \mathcal{T}	100		
$T_{\text{TEST}}, T_{\text{TRAIN}}$	100 snapshots		
$(K_\theta, K_\phi)_{\text{TRAIN}}$ [deg.]	120		
$(K_\theta, K_\phi)_{\text{TEST}}$ [deg.]	2		
$\text{SNR}_{\text{TRAIN}}$ [dB]	10		
SNR_{TEST} [dB]	5	-20 to 10	

where $\tilde{\phi}_k^i$ and ϕ_k denote the estimated and true k -th DOAs in the i -th trial, respectively.

Figure 7.3 shows the RMSE of DOA estimation as a function of SNR_{TEST} . In Fig. 7.3, the best subarray represents the subarray with the lowest CRB value or the ground truth. Thus, we compare the ground truth’s DOA estimation performance with the predicted arrays, i.e., CNN-generated sparse arrays by both the conventional and the SA-assisted method. As shown in Fig. 7.3, the SA-assisted method coincides quickly with the ground truth’s performance compared to the conventional method.

Finally, in example #3, we compare the antenna selection accuracy of the two DL-based methods. Here, we use the simulation parameters shown in the fourth column of Table 7.2. The realized sparse arrays from CNN are compared to the best subarrays or labels to evaluate the classification performance [85]. During the testing stage, the SNR_{TEST} is varied from -20 dB to 10 dB over 100 number of trials. Figure 7.4 shows the accuracy of sensor selection as a function of SNR_{TEST} , i.e.,

$$\text{Accuracy} = \frac{\mathcal{D}}{\mathcal{F}} \times 100 \%, \quad (7.11)$$

where \mathcal{D} is the total number of input data in which the model identifies the best subarray correctly \mathcal{F} times [85], [91]. From Fig. 7.4, it can be observed that the SA-assisted method has more than 90% accurate for $\text{SNR}_{\text{TEST}} \geq -8$ dB when the

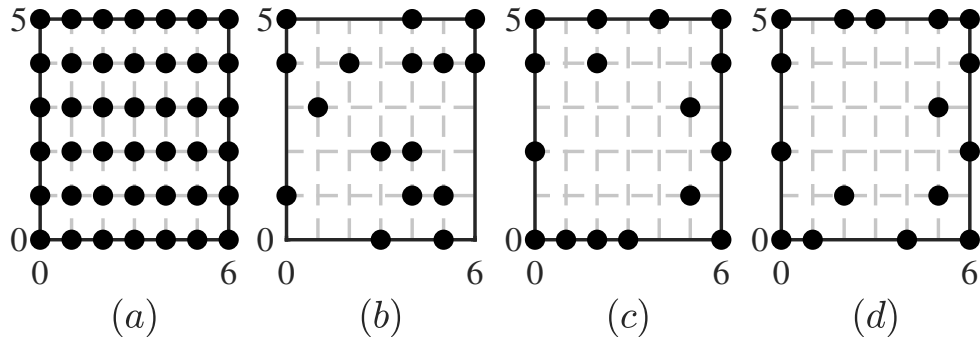


Figure 7.2: The array configurations of (a) parent 42–sensor URA, (b) the conventional DL-based array (16–sensors), (c) the conventional SA-based array (16–sensors) and (d) the proposed DL-based array (16–sensors). Note that the dots denote physical sensors.

network is trained by the dataset with $\text{SNR}_{\text{TRAIN}} \geq 10$ dB. Compared to the conventional method, it has less than 90% accuracy for $\text{SNR}_{\text{TEST}} \geq -8$ dB when the model is trained with the same parameters. Hence, the SA-assisted method performs better than the conventional method [91].

7.4 Trade-off analysis

In this section, we analyze the trade-off among different sparse array design methods in terms of i) computation complexity in Subsection 7.4.1 and ii) accuracy in Subsection 7.4.2. Since the computation complexity of the ad-hoc method can not be measured, the analysis focuses on the ML-based and traditional heuristic methods. Besides, for simplicity, we consider the SA method [93] and the SA-assisted DL-based method [92] as representative of the heuristic and ML-based methods, respectively. Moreover, *generalizability* and *specificity* are other important trade-offs that are beyond this chapter’s scope and can be considered as future work.

7.4.1 Computational complexity analysis

Here, we compare the computation complexity of the simulated annealing [93] and DL-based [92] methods to represent the heuristic and ML-based approaches, respec-

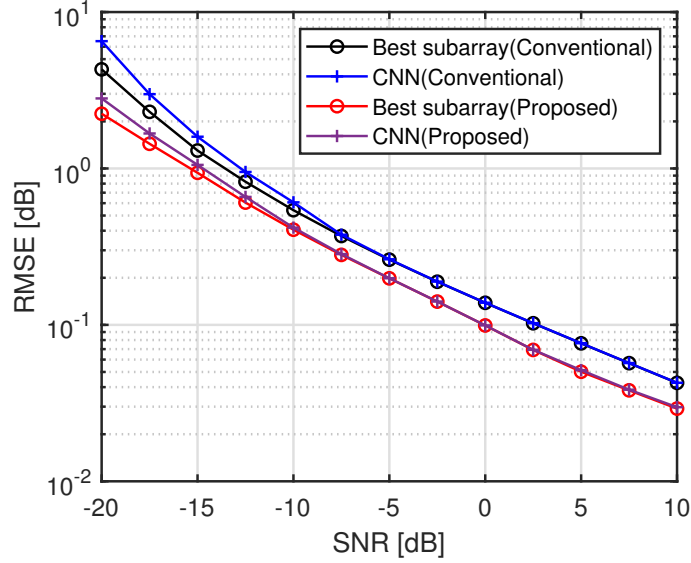


Figure 7.3: Comparison of DOA estimation of the conventional and proposed method for different array configurations.

tively. Firstly, the SA-based algorithm requires $\mathcal{O}(M)$ operations to realize a sparse array with M sensors. Then, approximately $\mathcal{O}(MN^2)$ operations are required to optimize the previously generated sparse subarray. Therefore, the computational complexity of the SA-based sparse array design method becomes

$$\mathcal{W}_{sa} = \mathcal{O}(MN^2 + M). \quad (7.12)$$

However, in the SA-assisted deep learning method [92], the SA-based algorithm was executed multiple times, specifically T times, to yield a considerable amount of subarrays to mimic conventional permutation or combination stages of the algorithm. Hence, multiplying that by the previously calculated \mathcal{W}_{sa} yields computation complexity of the SA-assisted stage as

$$\mathcal{W}_{dl} = \mathcal{O}(T(MN^2 + M)), \quad (7.13)$$

Table 7.3 summarizes the computational complexities of both methods [91]. A quick glance of (7.12) and (7.13), indicates that \mathcal{W}_{sa} is significantly lower by T as compared to \mathcal{W}_{dl} . However, as we shall see in the subsequent paragraphs, the DL-based

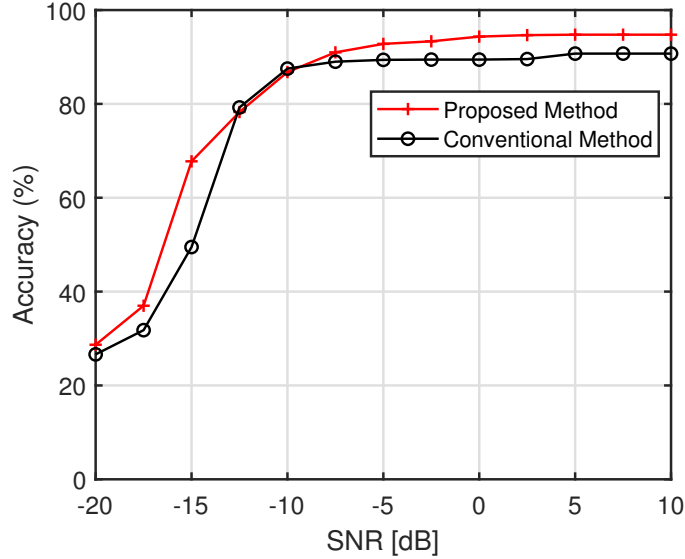


Figure 7.4: Performance of the conventional and SA-assisted method for different SNR_{TEST} values.

Table 7.3: Comparison of the computation complexity of the deep learning and SA-based sparse array design methods

Sparse array design method	Computational complexity
SA-based	$\mathcal{O}(MN^2 + M)$
DL-based	$\mathcal{O}(T(MN^2 + M))$

method requires less computation time to predict a sparse array once trained offline. manageable compared to the conventional method.

Next, we compare the computational time necessary for DL-and SA-based sparse array design methods. The methods were executed in MATLAB on a personal computer with Intel(R) Core (TM)-i5 processor operating at 2.60 GHz with 4GB of RAM. In this case, we consider the time to predict only for the DL-based approach and the time to optimize a single 2D sparse array under 100 iterations for the SA algorithm. Figure 7.5 shows the computation complexity of the sparse array design methods as a function of the array size. Unlike Table 7.3, which indicates that the SA-based method has less computation complexity than the DL-based method, Fig. 7.5 shows that the DL-based method required less time to predict a sparse 2D array once on-

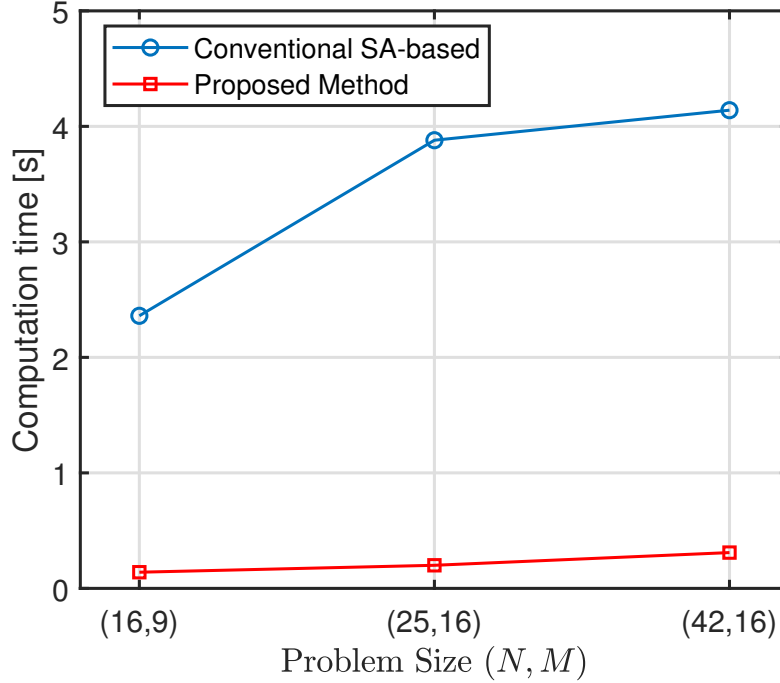


Figure 7.5: Comparison of computation time between the DL-based and traditional SA sparse array design techniques.

line [91]. Besides, the computation time does not increase with the problem size or space. On the other hand, the SA method can provide better solutions but at the cost of increased computational time and resources as the problem space increases. Meanwhile, the DL-based method offers a balance between these two extremes by providing high-quality solutions with reduced computational requirements.

7.4.2 Quality analysis: DOA estimation performance

Following the computation complexity analysis in Section 7.4.1, we examine the performance of 2D sparse arrays realized by the SA-assisted DL and SA-based methods as discussed in Section 7.3. In these numerical examples, all sparse arrays consist of 42 sensors, and conventional uniform rectangular arrays (URA) with 16 and 42 sensors are used for comparison purposes. In particular, we explore the behavior of the RMSE as a function of SNR and the number of snapshots. The RMSE is

calculated as

$$\text{RMSE} = \sqrt{\frac{1}{\mathcal{T}K} \sum_{i=1}^{\mathcal{T}} \sum_{k=1}^K [(\tilde{\phi}_k^i - \phi_k) + (\tilde{\theta}_k^i - \theta_k)]^2}, \quad (7.14)$$

where $\tilde{\phi}_k^i, \tilde{\theta}_k^i$ and ϕ_k, θ_k denote the estimated and true k -th DOAs in the i -th trial, respectively.

Besides, Table 7.4 summarizes the simulation parameters used to compute RMSE with respect to SNR (Example #1) and the number of snapshots (Example #2), respectively. Moreover, the 2D-ESPRIT algorithm is adopted as the default DOA estimator [95], [23]. However, if the difference co-array of the 2D sparse array generated via the SA algorithm is not hole-free, the resulting virtual 2D array becomes irregular. As such, the spatial-smoothing DOA estimation method such as 2D-ESPRIT cannot be applied since the 2D-ESPRIT algorithm requires a URA array structure for spatial smoothing pre-processes [23]. As a result, a nuclear norm minimization (NNM) approach is applied to fill the holes [93]-[95] and restore it to a standard 2D URA-like array.

Figure 7.6 shows the RMSE performance of different 2D sparse arrays as a function of input SNR. As shown in Fig. 7.6, the URA with 42 sensors has better performance overall due to its large effective aperture, whereas the URA with 16 sensors performed poorly than other methods. Thus, the URAs form the lower (URA with 42 sensors) and upper (URA with 16 sensors) performance bounds. In contrast, the DL-based sparse array performed better than the URA with 16 sensors and slightly lower than the URA with 42 sensors. Besides, the SA-based sparse array performs better next to the DL-based sparse array.

Figure 7.7 shows the RMSE versus the number of snapshots performance for various 2D sparse arrays. A similar trend is observed where the two URAs bound the performance of the SA-assisted DL and SA-based sparse arrays as the number of snapshots increases. The URA with 42 sensors has the lowest RMSE values, whereas the one with 16 has higher RMSE values than all other sparse arrays. Evidently, these examples demonstrate that the sparse array design methods can thin 2D arrays to a manageable size without considerable loss of DOA estimation resolution. More importantly, compared to the sparse array generated by the SA method, the sparse

Table 7.4: 2D DOA estimation simulation parameters

Parameters	Simulation examples	
	Example #1	Example #2
# of sources K	9	
# of trials, \mathcal{T}	1000	
# of snapshots	500	10 to 1000
SNR [dB]	-20 to 10	0
DOAs (θ, ϕ) [deg.]	(10, 255), (45, 300), (20, 345), (50, 210), (70, 0), (0, 30), (60, 165), (5, 120), (30, 79)	
Estimator	2D-ESPRIT	

array realized by the SA-assisted DL method exhibits enhanced DOA estimation performance.

7.5 Chapter summary

In this chapter, we evaluated two approaches to designing sparse arrays - heuristic and ML-based methods, using the example of the SA algorithm proposed in [92] and an SA-assisted DL sparse array design method [91]. The analysis focused on two parameters - the computational complexity of the method and the accuracy of DOA estimation performance of the resulting sparse arrays. Following the analysis, it is clear that while Ad-hoc methods may provide straightforward solutions, but they may not always be the most effective. On the other hand, heuristic methods utilize optimization algorithms which yield more efficient outcomes. However, for complex problems with intricate relationships and large amounts of data, especially high-dimensional data, machine learning, particularly deep learning, is the most suitable option.

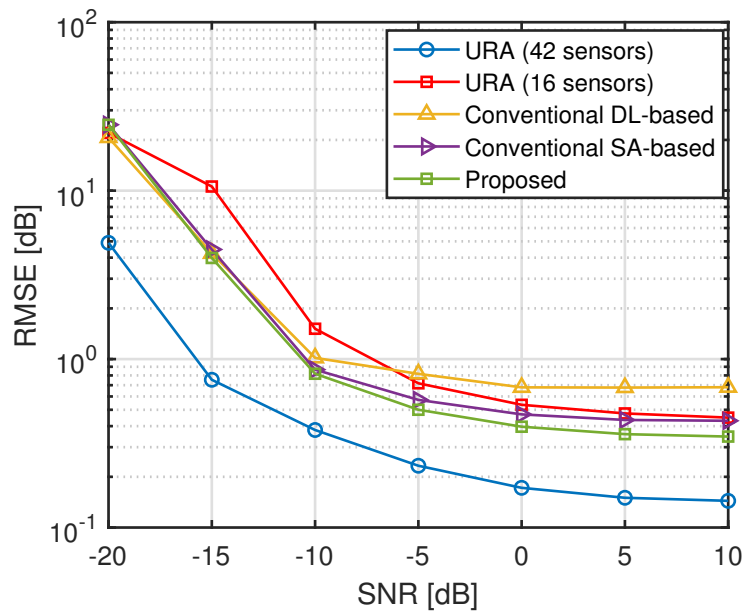


Figure 7.6: RMSE versus input SNR performance of different 2D sparse arrays.

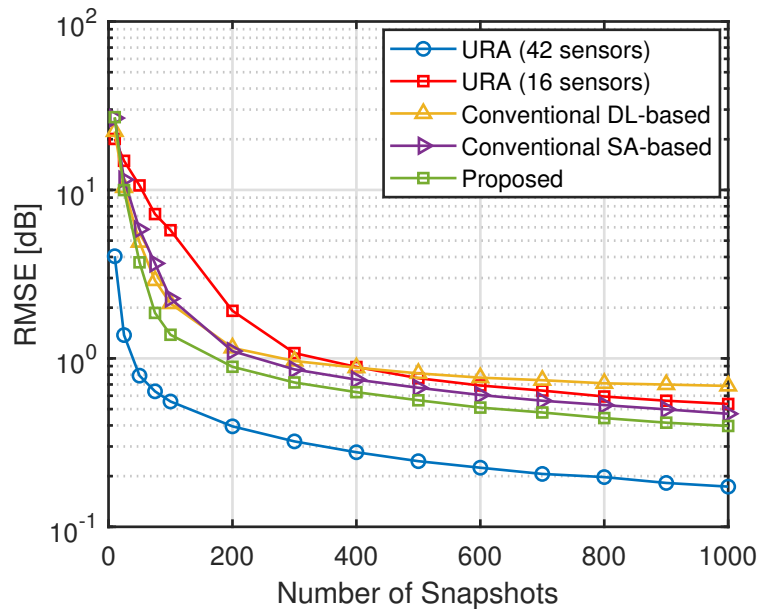


Figure 7.7: RMSE versus the number of snapshot performances of different 2D sparse arrays.

Concluding Remarks and Future Work

8.1 Concluding remarks

As reiterated throughout this dissertation, traditional uniform linear arrays (ULA) are limited when dealing with i) undetermined DOA estimation problems where there are more sensors than the number of sources or ii) when faced with a resolution dilemma given a restrictive array antenna mounting platform. Thanks to the concept of difference co-array, the larger interelement spacing in sparse arrays can be exploited to generate virtual sensors or lags and, therefore, improve the degrees of freedom (DOF) from $\mathcal{O}(N)$ to $\mathcal{O}(N^2)$ given N sensors only [8]-[10], [42]-[72]. The generated virtual array is used for DOA estimation with the help of co-array-based subspace estimators such as spatial smoothing MUSIC [33]-[34] and other similar methods [35]-[40]. As discussed in Chapter 2, prior sparse samplers or arrays include MHA [43], MRA [42], nested arrays [9], and coprime arrays [10]. These conventional arrays have shortfalls ranging from the lack of closed-form expression for sensor positions to limited DOF due to missing virtual sensors or holes, which ultimately reduce the usable or effective virtual array aperture [42]-[72]. It is these limitations that have motivated researchers to seek other sparse array designs with some or all of the following characteristics:

- a) The sparse array with closed-form expression for sensor positions [48].
- b) The sparse array with hole-free or near-hole-free difference co-array to maintain the optimal DOF [8], [13]-[16].
- c) The sparse array with a minimal sensor pairs with unit spacing to reduce the mutual coupling effect between sensors [44], [72].

Inspired by the limitations of conventional sparse arrays, especially nested arrays, a new sparse linear array known as extended nested array with multiple subarrays (ENAMS) is introduced in Chapter 3 [52]. The ENAMS array retains all the good properties of the nested array and attains improved DOF and a relatively reduced

mutual coupling effect compared to the nested array. Numerical examples demonstrate that the ENAMS array achieves high-resolution DOA estimation performance compared to a nested array given the same number of sensors. However, compared to other state-of-the-art sparse arrays such as TS-ENA [53] and MISC [51], the ENAMS array's DOF is limited.

To further improve the uniform DOF of the ENAMS array, flexible ENAMS arrays (type-I and type-II) are proposed in Chapter 4 [55]-[56]. The flexible ENAMS arrays are formed by relocating sensors from the dense subarrays (left and right subarrays) of TS-ENA into its sparse section (middle subarray), thereby enlarging the available array aperture while maintaining all the good properties of TS-ENA. Compared to MISC and TS-ENA arrays, the f-ENAMS arrays have enhanced DOF and relatively reduced mutual coupling. However, the TS-ENA array can relocate $n_{1,2} = 2$ sensors only and $n_{1,2} = 3$ sensors for the f-ENAMS-2 array against the observation that $n_{1,2}$ can attain any value in the range of $[1, \infty)$ [57]. Based on this observation and the IES criterion, the array patterns of the TS-ENA and f-ENAMS-2 arrays are unified, and a unified ENAMS array geometry called Generalized ENAMS (GENAMS) is proposed in Chapter 5. The GENAMS array leverages the variation of $n_{1,2}$ as N increases to construct an optimal sparse linear array [57]. Besides retaining all the properties of the TS-ENA array, the GENAMS array achieves improved DOF and exhibits high-resolution DOA estimation performance compared to other sparse arrays.

Thus, the critical contributions of this dissertation are the ENAMS, f-ENAMS, and GENAMS sparse array designs, which can be valuable in array signal processing for DOA estimation, even when the mutual coupling is present.

8.2 Future work

As for future work, designing sparse linear arrays with reduced mutual coupling effect is one of the possible research directions. In this work, the development of sparse linear arrays has been studied from the perspective of enhanced degrees of freedom for high-resolution DOA estimation. Although ultra-high array aperture or improved degrees of freedom guarantee optimal DOA estimation performance, as we

have witnessed in the case of the GENAMS array in Chapter 5, the performance of sparse arrays deteriorates as the strength of mutual coupling increases to the extent that the DOA estimation performance no longer depends of available DOF but rather the mutual coupling effect.

Furthermore, despite the effort by the researcher to balance the two factors - available DOF and mutual coupling effect, the design of sparse linear arrays with higher DOF and reduced MC effect remains one of the hot topics in array signal processing, especially at the time undetermined array signal processing problems are more attractive. On the other hand, it is worth noting that tremendous effort and achievement have been made in developing sparse linear arrays for the past seven years, and less to 2D or planar arrays for array signal processing applications. Therefore, extending such efforts on 2D sparse arrays with enhanced DOF and less mutual coupling is another promising research direction for sparse array design [91]-[96], [99]-[104].

Bibliography

- [1] N. Kshetri, “5G in E-Commerce Activities,” *IT Professional*, vol. 20, no. 4, pp. 73-77, Jul./Aug. 2018, doi: [10.1109/MITP.2018.043141672](https://doi.org/10.1109/MITP.2018.043141672).
- [2] B. P. S. Sahoo, C. -C. Chou, C. -W. Weng and H. -Y. Wei, “Enabling Millimeter-Wave 5G Networks for Massive IoT Applications: A Closer Look at the Issues Impacting Millimeter-Waves in Consumer Devices Under the 5G Framework,” *IEEE Consumer Electronics Magazine*, vol. 8, no. 1, pp. 49-54, Jan. 2019, doi: [10.1109/MCE.2018.2868111](https://doi.org/10.1109/MCE.2018.2868111).
- [3] Y. Yifei and Z. Longming, “Application scenarios and enabling technologies of 5G,” *China Communications*, vol. 11, no. 11, pp. 69-79, Nov. 2014, doi: [10.1109/CC.2014.7004525](https://doi.org/10.1109/CC.2014.7004525).
- [4] R. Müller and M. Landmann, “Potential of THz Broadband Systems for Joint Communication, Radar, and Sensing Applications in 6G,” *Shaping Future 6G Networks: Needs, Impacts, and Technologies*, *IEEE*, 2022, pp.89-99, doi:[10.1002/9781119765554.ch7](https://doi.org/10.1002/9781119765554.ch7).
- [5] M. Kantardzic and J. Zurada, “Data Projection Techniques and Their Application in Sensor Array Data Processing,” *Next Generation of Data-Mining Applications*, *IEEE*, 2005, pp.57-77, doi: [10.1109/9780471696650.ch3](https://doi.org/10.1109/9780471696650.ch3).
- [6] H. Hallil and C. Dejous, “Microwave Chemical Sensors,” *Smart Sensors for Environmental and Medical Applications*, *IEEE*, 2020, pp.193-216, doi: [10.1002/9781119587422.ch10](https://doi.org/10.1002/9781119587422.ch10).
- [7] A. Shastri et al., “A Review of Millimeter Wave Device-Based Localization and Device-Free Sensing Technologies and Applications,” *IEEE Communications Surveys and Tutorials*, vol. 24, no. 3, pp. 1708-1749, third quarter 2022, doi: [10.1109/COMST.2022.3177305](https://doi.org/10.1109/COMST.2022.3177305).

- [8] C. Liu, “Sparse Array Signal Processing: New Array Geometries, Parameter Estimation, and Theoretical Analysis,” *PhD Thesis*, California Institute of Technology, 2018.
- [9] P. Pal and P. P. Vaidyanathan, “Nested Arrays: A Novel Approach to Array Processing With Enhanced Degrees of Freedom,” *IEEE Transactions on Signal Processing*, vol. 58, no. 8, pp. 4167–4181, Aug. 2010, doi: [10.1109/TSP.2010.2049264](https://doi.org/10.1109/TSP.2010.2049264).
- [10] P. P. Vaidyanathan and P. Pal, “Sparse Sensing with Co-prime Samplers and Arrays,” *IEEE Trans. Signal Process.*, vol. 59, no. 2, pp. 573–586, Feb. 2011, issn:1053-587X. doi: [10.1109/TSP.2010.2089682](https://doi.org/10.1109/TSP.2010.2089682).
- [11] D. D. Ariananda and G. Leus, “Compressive wideband power spectrum estimation,” *IEEE Trans. Signal Process.*, vol. 60, no. 9, pp. 4775–4789, Sep. 2012, issn: 1053-587X. doi: [10.1109/TSP.2012.2201153](https://doi.org/10.1109/TSP.2012.2201153).
- [12] Y. Chen, Y. Chi, and A. J. Goldsmith, “Exact and stable covariance estimation from quadratic sampling via convex programming,” *IEEE Trans. Inf. Theory*, vol. 61, no. 7, pp. 4034–4059, Jul. 2015, issn: 0018-9448. doi: [10.1109/TIT.2015.2429594](https://doi.org/10.1109/TIT.2015.2429594).
- [13] T. E. Tuncer and B. Friedlander, “Classical and modern direction of arrival estimation,” *Academic Press*, 2009.
- [14] H. L. Van Trees, “Optimum array processing, detection, estimation and modulation Part IV,” *John Wiley and Sons*, 2002.
- [15] A. Jafri, “Array Signal Processing Based on Traditional and Sparse Arrays,” *PhD thesis*, University of Sheffield, 2019.
- [16] D. H. Johnson and D. E. Dudgeon, “Array signal processing: Concepts and techniques,” *Addison-Wesley Pub Co Inc*, Feb. 11, 1993, 512 pp., isbn: 0130485136.
- [17] M. S. Bartlett, “Smoothing periodograms from time-series with continuous spectra,” *Nature*, vol. 161, pp. 686–687, May 1948. doi: [10.1038/161686a0](https://doi.org/10.1038/161686a0).

- [18] J. Capon, “High-resolution frequency-wavenumber spectrum analysis,” *Proc. IEEE*, vol. 57, no. 8, pp. 1408–1418, Aug. 1969, issn: 0018-9219. doi: [10.1109/PROC.1969.7278](https://doi.org/10.1109/PROC.1969.7278).
- [19] V. F. Pisarenko, “The retrieval of harmonics from a covariance function,” *Geophys. J. R. astr. Soc.*, vol. 33, pp. 347–366, 1973. doi: [10.1111/j.1365-246X.1973.tb03424.x](https://doi.org/10.1111/j.1365-246X.1973.tb03424.x).
- [20] G. Bienvenu and L. Kopp, “Optimality of high resolution array processing using the eigensystem approach,” *IEEE Trans. Acoust., Speech, Signal Process.*, vol. 31, no. 5, pp. 1235–1248, Oct. 1983, issn: 0096-3518. doi: [10.1109/TASSP.1983.1164185](https://doi.org/10.1109/TASSP.1983.1164185).
- [21] J. Singer, “A theorem in finite projective geometry and some applications to number theory,” *Trans. Amer. Math. Soc.*, vol. 43, pp. 377–385, 1938. doi: [10.1090/S0002-9947-1938-1501951-4](https://doi.org/10.1090/S0002-9947-1938-1501951-4).
- [22] R. Kumaresan and D.W. Tufts, “Estimating the angles of arrival of multiple plane waves,” *IEEE Trans. Aerosp. Electron. Syst.*, vol. AES-19, no. 1, pp. 134–139, Jan. 1983, issn: 0018-9251. doi: [10.1109/TAES.1983.309427](https://doi.org/10.1109/TAES.1983.309427).
- [23] R. Roy and T. Kailath, “ESPRIT-estimation of signal parameters via rotational invariance techniques,” *IEEE Trans. Acoust., Speech, Signal Process.*, vol. 37, no. 7, pp. 984–995, Jul. 1989, issn: 0096-3518. doi: [10.1109/29.32276](https://doi.org/10.1109/29.32276).
- [24] P. Stoica and A. Nehorai, “MUSIC, maximum likelihood, and Cramer-Rao bound,” *IEEE Trans. Acoust., Speech, Signal Process.*, vol. 37, no. 5, pp. 720–741, May 1989, issn: 0096-3518. doi: [10.1109/29.17564](https://doi.org/10.1109/29.17564).
- [25] P. Stoica and A. Nehorai, “Performance study of conditional and unconditional direction-of-arrival estimation,” *IEEE Trans. Acoust., Speech, Signal Process.*, vol. 38, no. 10, pp. 1783–1795, Oct. 1990, issn: 0096-3518. doi: [10.1109/29.60109](https://doi.org/10.1109/29.60109).
- [26] P. Stoica and K. C. Sharman, “Maximum likelihood methods for direction-of-arrival estimation,” *IEEE Trans. Acoust., Speech, Signal Process.*, vol. 38, no. 7, pp. 1132–1143, Jul. 1990, issn: 0096-3518. doi: [10.1109/29.57542](https://doi.org/10.1109/29.57542).

- [27] R. Krummenauer, M. Cazarotto, A. Lopes, P. Larzabal, P. Forster, “Improving the threshold performance of maximum likelihood estimation of direction of arrival,” *Signal Processing*, vol.90, no.5, pp.1582, 2010.
- [28] C. Qian, L. Huang, M. Cao, J. Xie and H. C. So, “PUMA: An Improved Realization of MODE for DOA Estimation,” *IEEE Transactions on Aerospace and Electronic Systems*, vol. 53, no. 5, pp. 2128-2139, Oct. 2017, doi: [10.1109/TAES.2017.2683598](https://doi.org/10.1109/TAES.2017.2683598).
- [29] L. Xie, Z. He and J. Tong, “A Fast Gridless Method for High Order Motion Parameter Estimation Based on PUMA,” *2020 15th IEEE International Conference on Signal Processing (ICSP)*, Beijing, China, 2020, pp. 610-615, doi: [10.1109/ICSP48669.2020.9321018](https://doi.org/10.1109/ICSP48669.2020.9321018).
- [30] S. Hamada and K. Ichige, “Modified MODE for increasing the maximum number of sources in DOA estimation,” *IEICE Communications Express*, vol.10, no.7, pp.391, 2021, doi: <https://doi.org/10.1587/comex.2021XBL0085>.
- [31] B. Fuchs, “Antenna Selection for Array Synthesis Problems,” *IEEE Antennas and Wireless Propagation Letters*, vol. 16, pp. 868-871, 2017, doi: [10.1109/LAWP.2016.2612762](https://doi.org/10.1109/LAWP.2016.2612762).
- [32] Y. Abramovich, D. Gray, A. Gorokhov, and N. Spencer, “Positive-definite Toeplitz completion in DOA estimation for nonuniform linear antenna arrays—Part I: Fully augmentable arrays,” *IEEE Trans. Signal Process.*, vol. 46, no. 9, pp. 2458–2471, Sep. 1998, issn: 1053-587X. doi: [10.1109/78.709534](https://doi.org/10.1109/78.709534).
- [33] C.-L. Liu and P. P. Vaidyanathan, “Remarks on the spatial smoothing step in coarray MUSIC,” *IEEE Signal Process. Lett.*, vol. 22, no. 9, pp. 1438–1442, Sep. 2015. doi: [10.1109/LSP.2015.2409153](https://doi.org/10.1109/LSP.2015.2409153).
- [34] P. Pal and P. P. Vaidyanathan, “Coprime sampling and the MUSIC algorithm,” *Proc. IEEE Dig. Signal Process. Signal Process. Educ. Workshop*, Sedona, AZ, USA, Jan. 2011, pp. 289–294. doi: [10.1109/DSP-SPE.2011.5739227](https://doi.org/10.1109/DSP-SPE.2011.5739227).
- [35] C.-L. Liu, P. P. Vaidyanathan, and P. Pal, “Coprime coarray interpolation for DOA estimation via nuclear norm minimization,” *Proc. IEEE Int.*

- Symp. Circuits and Syst.*, Montreal, Canada, May 2016, pp. 2639–2642. doi: [10.1109/ISCAS.2016.7539135](https://doi.org/10.1109/ISCAS.2016.7539135).
- [36] T. E. Tuncer, T. K. Yasar, and B. Friedlander, “Direction of arrival estimation for non-uniform linear arrays by using array interpolation,” *Radio Science*, vol. 42, no. 4, Aug. 2007, issn: 1944-799X. doi: [10.1029/2007RS003641](https://doi.org/10.1029/2007RS003641).
- [37] W.-K. Ma, T.-H. Hsieh, and C.-Y. Chi, “DOA estimation of quasi-stationary signals via Khatri-Rao subspace,” *Proc. IEEE Int. Conf. Acoust., Speech, and Sig. Proc.*, Taipei, Taiwan, Apr. 2009, pp. 2165–2168. doi: [10.1109/ICASSP.2009.4960046](https://doi.org/10.1109/ICASSP.2009.4960046).
- [38] W.-K. Ma, T.-H. Hsieh, and C.-Y. Chi, “DOA estimation of quasi-stationary signals with less sensors than sources and unknown spatial noise covariance: A Khatri-Rao subspace approach,” *IEEE Trans. Signal Process.*, vol. 58, no. 4, pp. 2168–2180, Apr. 2010, issn: 1053-587X. doi: [10.1109/TSP.2009.2034935](https://doi.org/10.1109/TSP.2009.2034935).
- [39] Ka-Kit Lee, Wing-Kin Ma, Xiao Fu, Tsung-Han Chan, Chong-Yung Chi, “A Khatri-Rao subspace approach to blind identification of mixtures of quasi-stationary sources,” *Signal Processing*, vol.93, no.12, pp.3515, 2013.
- [40] M. Inoue, K. Hayashi, H. Mori and T. Nabetani, “A DOA Estimation Method With Kronecker Subspace for Coherent Signals,” *IEEE Communications Letters*, vol. 22, no. 11, pp. 2306-2309, Nov. 2018, doi: [10.1109/LCOMM.2018.2870824](https://doi.org/10.1109/LCOMM.2018.2870824).
- [41] P. Chevalier, L. Albera, A. Ferrol, P. Comon, “On the virtual array concept for higher order array processing,” *IEEE Trans. Signal Processing*, vol. 53, no.4, pp. 1254-1271, Sep. 2005.
- [42] A. Moffet, “Minimum-redundancy linear arrays,” *IEEE Trans. Antennas Propagation*, vol. 16, no. 2, pp. 172-175, Mar. 1968.
- [43] E. Vertatschitsch and S. Haykin, “Non-redundancy arrays,” *Proc. in IEEE*, vol. 74, no.1, pp. 217-217, Jan. 1986.

- [44] C. Liu and P. P. Vaidyanathan, "Super nested arrays: Linear sparse arrays with reduced mutual coupling-Part I: Fundamentals," *IEEE Trans. Signal Processing*, vol. 64, no. 15, pp.3997-4014, Aug. 2016.
- [45] J. Shi, G. Hu, X. Zhang and H. Zhou, "Generalized Nested Array: Optimization for Degrees of Freedom and Mutual Coupling," *IEEE Communications Letters*, vol. 22, no. 6, pp. 1208-1211, Jun. 2018.
- [46] S. Qin, Y. D. Zhang and M. G. Amin, "Generalized Coprime Array Configurations for Direction-of-Arrival Estimation," *IEEE Transactions on Signal Processing*, vol. 63, no. 6, pp. 1377-1390, Mar. 2015.
- [47] A. Raza, W. Liu and Q. Shen, "Thinned coprime arrays for DOA estimation," *Proc. of 2017 25th European Signal Processing Conference (EUSIPCO)*, pp. 395-399, 2017.
- [48] J. Liu, Y. Zhang, Y. Lu, S. Ren and S. Cao, "Augmented nested arrays with enhanced DOF and reduced mutual coupling," *IEEE Transactions on Signal Processing*, vol. 65, no. 21, pp. 5549-5563, Nov. 2017.
- [49] P. Zhao, G. Hu, Z. Qu and L. Wang, "Enhanced Nested Array Configuration With Hole-Free Co-Array and Increasing Degrees of Freedom for DOA Estimation," *IEEE Communications Letters*, vol. 23, no. 12, pp. 2224-2228, Dec. 2019.
- [50] M. Yang, L. Sun, X. Yuan and B. Chen, "Improved nested array with hole-free DCA and more degrees of freedom," *Electronics Letters*, vol. 52, no. 25, p. 2068 – 2070, Dec. 2016.
- [51] Z. Zheng, W. Wang, Y. Kong and Y. D. Zhang, "MISC Array: A New Sparse Array Design Achieving Increased Degrees of Freedom and Reduced Mutual Coupling Effect," *IEEE Transactions on Signal Processing*, vol. 67, no. 7, pp. 1728-1741, Apr. 2019
- [52] Y. Iizuka and K. Ichige, "Extension of Nested Array for Large Aperture and High Degree of Freedom," *IEICE Communication Express*, vol. 6, no. 6, pp. 381-386, Jun. 2017.

- [53] S. Ren, W. Dong, X. Li, W. Wang and X. Li, “Extended Nested Arrays for Consecutive Virtual Aperture Enhancement,” *IEEE Signal Processing Letters*, vol. 27, pp. 575-579, 2020.
- [54] S. Wandale and K. Ichige, “A Nested Array Geometry with Enhanced Degrees of Freedom and Hole- Free Difference Coarray,” 2021 29th European Signal Processing Conference (EUSIPCO), Dublin, Ireland, 2021, pp. 1905-1909, doi: [10.23919/EUSIPCO54536.2021.9616342](https://doi.org/10.23919/EUSIPCO54536.2021.9616342).
- [55] S. Wandale and K. Ichige, “Flexible Extended Nested Array with Multiple Sub-arrays Achieving Improved Degrees of Freedom,” 2022 30th European Signal Processing Conference (EUSIPCO), Belgrade, Serbia, 2022, pp. 1931-1935, doi: [10.23919/EUSIPCO55093.2022.9909786](https://doi.org/10.23919/EUSIPCO55093.2022.9909786).
- [56] S. Wandale, and K. Ichige, “Flexible extended nested arrays for DOA estimation: Degrees of freedom perspective,” *Signal Processing*, vol. 201, no. 108710, 2022. ISSN 0165-1684, <https://doi.org/10.1016/j.sigpro.2022.108710>.
- [57] S. Wandale and K. Ichige, “A Generalized Extended Nested Array Design via Maximum Inter-Element Spacing Criterion,” in *IEEE Signal Processing Letters*, vol. 30, pp. 31-35, 2023, doi: [10.1109/LSP.2023.3238912](https://doi.org/10.1109/LSP.2023.3238912).
- [58] A. Ahmed and Y. D. Zhang, “Generalized Non-Redundant Sparse Array Designs,” *IEEE Transactions on Signal Processing*, vol. 69, pp. 4580-4594, 2021.
- [59] Z. Peng, Y. Ding, S. Ren, H. Wu and W. Wang, “Coprime Nested Arrays for DOA Estimation: Exploiting the Nesting Property of Coprime Array,” *IEEE Signal Processing Letters*, vol. 29, pp. 444-448, 2022.
- [60] A. M. A. Shaalan, J. Du and Y. H. Tu, “Dilated Nested Arrays With More Degrees of Freedom (DOFs) and Less Mutual Coupling—Part I: The Fundamental Geometry,” *IEEE Transactions on Signal Processing*, vol. 70, pp. 2518-2531, 2022.
- [61] R. K. Patra and A. S. Dhar, “A Novel k -times Extended Coprime Array for DOA Estimation With Increased Degrees of Freedom,” *IEEE Signal Processing Letters*, vol. 29, pp. 1402-1406, 2022.

- [62] W. Zheng, X. Zhang, Y. Wang, J. Shen, and B. Champagne, “Padded Coprime Arrays for Improved DOA Estimation: Exploiting Hole Representation and Filling Strategies,” *IEEE Transactions on Signal Processing*, vol. 68, pp. 4597-4611, 2020.
- [63] N. Mohsen, A. Hawbani, M. Agrawal, S. Alsamhi and L. Zhao, “A New Coprime-Array-based Configuration with Augmented Degrees of Freedom and Reduced Mutual Coupling,” ’2022 IEEE International Conference on Acoustics, Speech and Signal Processing (ICASSP 2022), pp. 5033-5037, 2022.
- [64] W. Shi, S. A. Vorobyov and Y. Li, “ULA Fitting for Sparse Array Design,” *IEEE Transactions on Signal Processing*, vol. 69, pp. 6431-6447, 2021.
- [65] W. Shi, Y. Li and R. C. de Lamare, “Novel Sparse Array Design Based on the Maximum Inter-Element Spacing Criterion,” *IEEE Signal Processing Letters*, vol. 29, pp. 1754-1758, 2022.
- [66] S. Zhang, Z. Zhou, G. Cui, X. Tang, and P. Fan. “A New Low-Redundancy Restricted Array with Reduced Mutual Coupling.” *arXiv preprint [arXiv:2208.05263\(2022\)](https://arxiv.org/abs/2208.05263)*.
- [67] A. Kedar, “Realization of Low Sidelobe Level Sparse Array Antennas Using Fractal Structures,” *2022 IEEE Wireless Antenna and Microwave Symposium (WAMS)*, Rourkela, India, 2022, pp. 1-4, doi: [10.1109/WAMS54719.2022.9848204](https://doi.org/10.1109/WAMS54719.2022.9848204).
- [68] P. Ma, J. Li, J. Pan, X. Zhang and R. Gil-Pita, “Enhanced DOA Estimation With Augmented CADiS by Exploiting Array Motion Strategies,” *IEEE Transactions on Vehicular Technology*, vol. 72, no. 4, pp. 4713-4727, April 2023, doi: [10.1109/TVT.2022.3224908](https://doi.org/10.1109/TVT.2022.3224908).
- [69] P. Zhao, Q. Wu, Z. Chen, G. Hu, L. Wang and L. Wan, “Generalized Nested Array Configuration Family for Direction-of-Arrival Estimation,” *IEEE Transactions on Vehicular Technology*, doi: [10.1109/TVT.2023.3260196](https://doi.org/10.1109/TVT.2023.3260196).
- [70] H. Xiao, B. Zhou, Y. Zhang and G. Xiao, “On the Foundation of Sparsity Constrained Sensing (Part II): Diophantine Sampling with Arbitrary Temporal

- and Spatial Sparsity,” *IEEE Transactions on Signal Processing*, vol. 71, pp. 1277-1292, 2023, doi: [10.1109/TSP.2023.3248493](https://doi.org/10.1109/TSP.2023.3248493).
- [71] J. Shi, F. Wen, Y. Liu, Z. Liu and P. Hu, “Enhanced and Generalized Coprime Array for Direction of Arrival Estimation,” *IEEE Transactions on Aerospace and Electronic Systems*, vol. 59, no. 2, pp. 1327-1339, April 2023, doi: [10.1109/TAES.2022.3200929](https://doi.org/10.1109/TAES.2022.3200929).
- [72] C. Liu and P. P. Vaidyanathan, “Super Nested Arrays: Linear Sparse Arrays With Reduced Mutual Coupling—Part II: High-Order Extensions,” *IEEE Transactions on Signal Processing*, vol. 64, no. 16, pp. 4203-4217, Aug. 2016
- [73] P. Pal and P. P. Vaidyanathan, “Nested arrays in two dimensions, Part II: Application in two dimensional array processing,” *IEEE Trans. Signal Process.*, vol. 60, no. 9, pp. 4706–4718, Sep. 2012.
- [74] S. K. Yadav and N. V. George, “Fast Direction-of-Arrival Estimation via Coarray Interpolation Based on Truncated Nuclear Norm Regularization,” *IEEE Transactions on Circuits and Systems II: Express Briefs*, vol. 68, no. 4, pp. 1522-1526, April 2021, doi: [10.1109/TCSII.2020.3025629](https://doi.org/10.1109/TCSII.2020.3025629).
- [75] C. Zhou, Z. Shi, Y. Gu and Y. D. Zhang, “Coarray Interpolation-Based Coprime Array Doa Estimation Via Covariance Matrix Reconstruction,” *2018 IEEE International Conference on Acoustics, Speech and Signal Processing (ICASSP)*, Calgary, AB, Canada, 2018, pp. 3479-3483, doi: [10.1109/ICASSP.2018.8461721](https://doi.org/10.1109/ICASSP.2018.8461721).
- [76] S. K. Yadav and N. V. George, “Underdetermined DOA Estimation Using Arbitrary Planar Arrays via Coarray Manifold Separation,” *IEEE Transactions on Vehicular Technology*, vol. 71, no. 11, pp. 11959-11971, Nov. 2022, doi: [10.1109/TVT.2022.3194409](https://doi.org/10.1109/TVT.2022.3194409).
- [77] Q. Fan, Y. Liu, T. Yang and H. Peng, “Fast and Accurate Spectrum Estimation via Virtual Coarray Interpolation Based on Truncated Nuclear Norm Regularization,” *IEEE Signal Processing Letters*, vol. 29, pp. 169-173, 2022, doi: [10.1109/LSP.2021.3130018](https://doi.org/10.1109/LSP.2021.3130018).

- [78] Donghe Liu, Yongbo Zhao, Tingxiao Zhang, “Sparsity-Based Two-Dimensional DOA Estimation for Co-Prime Planar Array via Enhanced Matrix Completion,” *Remote Sensing*, vol.14, no.19, pp.4690, 2022.
- [79] P. Sarangi, M. C. Hücümenoğlu and P. Pal, “Single-Snapshot Nested Virtual Array Completion: Necessary and Sufficient Conditions,” *IEEE Signal Processing Letters*, vol. 29, pp. 2113-2117, 2022, doi: [10.1109/LSP.2022.3213140](https://doi.org/10.1109/LSP.2022.3213140).
- [80] P. Sarangi, M. C. Hücümenoğlu and P. Pal, “Beyond Coarray MUSIC: Harnessing the Difference Sets of Nested Arrays With Limited Snapshots,” *IEEE Signal Processing Letters*, vol. 28, pp. 2172-2176, 2021, doi: [10.1109/LSP.2021.3120939](https://doi.org/10.1109/LSP.2021.3120939).
- [81] Z. Zheng, Y. Huang, W. -Q. Wang and H. C. So, “Direction-of-Arrival Estimation of Coherent Signals via Coprime Array Interpolation,” *IEEE Signal Processing Letters*, vol. 27, pp. 585-589, 2020, doi: [10.1109/LSP.2020.2982769](https://doi.org/10.1109/LSP.2020.2982769).
- [82] G. Doblinger, “Optimized design of interpolated array and sparse array wideband beamformers,” *Proc. of 16th European Signal Processing Conference (EU-SIPCO)*, pp. 1520-614, Aug. 2008.
- [83] X. Wang, E. A. Aboutanios and M. G. Amin, “Adaptive Array Thinning for Enhanced DOA estimation,” *IEEE Signal Processing Letters*, vol. 22, no. 7, pp. 799-803, July 2015.
- [84] X. wand, P. Wang, and X. Wang, “Adaptive sparse array reconfiguration based on machine learning algorithms,” *Proc. of IEEE International Conference on Acoustics, Speech and Signal Processing (ICASSP)*, pp. 1159-1163, 2018.
- [85] A. M. Elbir, K. V. Mishra and Y. C. Eldar, “Cognitive radar antenna selection via deep learning,” *IET Radar, Sonar & Navigation*, vol. 13, no. 6, pp. 871-880, 2019.
- [86] K. Aghababaiyan, R. G. Zefreh and V. Shah-Mansouri, “3D-OMP and 3D-FOMP algorithms for DOA estimation,” *Physical Communication*, vol. 31, pp. 87-95, Dec. 2018.

- [87] A. M. Elbir, S. Mulleti, R. Cohen, R. Fu and Y. C. Eldar, “Deep-sparse array cognitive radar,” *Proc. of IEEE International Conference on Sampling Theory and Application*, pp. 1-5, 2019.
- [88] A. M. Elbir and K. V. Mishra, “Sparse Array Selection Across Arbitrary Sensor Geometries With Deep Transfer Learning,” *IEEE Transactions on Cognitive Communications and Networking*, vol. 7, no. 1, pp. 255-264, Mar. 2021.
- [89] S. Wandale and K. Ichige, “On the DOA Estimation Performance of Optimum Arrays Based on Deep Learning,” *Proc. of 2020 IEEE 11th Sensor Array and Multichannel Signal Processing Workshop (SAM)*, pp. 1-5, 2020.
- [90] S. Wandale and K. Ichige, “Design of Sparse Arrays via Deep Learning for Enhanced DOA Estimation,” *EURASIP Journal of Advances in Signal Processing* 2021, 17 (2021).
- [91] S. Wandale and K. Ichige, “Simulated Annealing Assisted Sparse Array Selection Utilizing Deep Learning,” *IEEE Access*, vol. 9, pp. 156907-156914, 2021, [doi: 10.1109/ACCESS.2021.3129856](https://doi.org/10.1109/ACCESS.2021.3129856).
- [92] S. Nakamura, S. Iwazaki and K. Ichige, “An Optimum 2D Sparse Array Configuration with Reduced Mutual Coupling,” *Proc. of 2018 International Symposium on Antennas and Propagation (ISAP)*, pp. 617-618, 2018.
- [93] S. Nakamura, S. Iwazaki and K. Ichige, “Optimum 2D Sparse Array and its Interpolation via Nuclear Norm Minimization,” *Proc. of 2019 IEEE International Symposium on Circuits and Systems (ISCAS)*, pp. 1-5, 2019.
- [94] S. Nakamura, S. Iwazaki and K. Ichige, “Optimization and Hole Interpolation of 2-D Sparse Arrays for Accurate Direction-of-Arrival Estimation,” *IEICE Trans. Communications*, vol. E104-B, no. 4, Apr. 2021.
- [95] C. Liu and P. P. Vaidyanathan, “Hourglass Arrays and Other Novel 2-D Sparse Arrays With Reduced Mutual Coupling,” *IEEE Transactions on Signal Processing*, vol. 65, no. 13, pp. 3369-3383, July 2017.

- [96] I. Aboumahmoud, A. Muqaibel, M. Alhassoun and S. Alawsh, "A Review of Sparse Sensor Arrays for Two-Dimensional Direction-of-Arrival Estimation," *IEEE Access*, vol. 9, pp. 92999-93017, 2021, [doi:10.1109/ACCESS.2021.3092529](https://doi.org/10.1109/ACCESS.2021.3092529).
- [97] A. Ishimaru, "Theory of unequally-spaced arrays," *Transactions on Antennas and Propagation*, vol. 10, no. 6, pp. 691-702, Nov. 1962.
- [98] L. F. Yepes, D. H. Covarrubias, M. A. Alonso and R. Ferrús, "Hybrid Sparse Linear Array Synthesis Applied to Phased Antenna Arrays," *IEEE Antennas and Wireless Propagation Letters*, vol. 13, pp. 185-188, 2014.
- [99] C. Yan, P. Yang, Z. Xing and S. Y. Huang, "Synthesis of Planar Sparse Arrays With Minimum Spacing Constraint," *IEEE Antennas and Wireless Propagation Letters*, vol. 17, no. 6, pp. 1095-1098, June 2018.
- [100] K. Chen, X. Yun, Z. He and C. Han, "Synthesis of Sparse Planar Arrays Using Modified Real Genetic Algorithm," *IEEE Transactions on Antennas and Propagation*, vol. 55, no. 4, pp. 1067-1073, Apr. 2007.
- [101] X. Wang, E. A. Aboutanios and M. G. Amin, "Adaptive Array Thinning for Enhanced DOA estimation," *IEEE Signal Processing Letters*, vol. 22, no. 7, pp. 799-803. July 2015.
- [102] J. F. Hopperstad and S. Holm, "The coarray of sparse arrays with minimum sidelobe level," *Proc. of 3rd IEEE Nordic Signal Processing Symposium (NOR-SIG'98)*, Denmark, pp. 137-140, Jun. 1998.
- [103] H. Liu, H. Zhao, W. Li and B. Liu, "Synthesis of Sparse Planar Arrays Using Matrix Mapping and Differential Evolution," *IEEE Antennas and Wireless Propagation Letters*, vol. 15, pp. 1905-1908, 2016.
- [104] C. R. Greene and R. C. Wood, "Sparse array performance," *J. Acoust. Soc. Amer.*, vol. 63, no. 6, pp. 1866-1872, 1978.

- [105] R. Hoctor and S. Kassam, “The unifying role of the coarray in aperture synthesis for coherent and incoherent imaging,” *Proc. IEEE*, vol. 78, no. 4, pp. 735–752, Apr. 1990.
- [106] J. Tabrikian, O. Isaacs and I. Bilik, “Cognitive antenna selection for DOA estimation in automotive radar,” *Proc. of IEEE Radar Conference (RadarConf)*, Philadelphia, PA, pp. 1-5, 2016.
- [107] O. Isaacs, J. Tabrikian and I. Bilik, “Cognitive antenna selection for optimal source localization,” *Proc. of 6th IEEE International Workshop on Computational Advances in Multi-Sensor Adaptive Processing (CAMSAP)*, Cancun, pp. 341-344, 2015.
- [108] A. M. Elbir, “DeepMUSIC: Multiple Signal Classification via Deep Learning,” *IEEE Sensors Letters*, vol. 4, no. 4, pp. 1-4, Apr. 2020.
- [109] J. Joung, “Machine Learning-Based Antenna Selection in Wireless Communications,” *IEEE Communications Letters*, vol. 20, no. 11, pp. 2241-2244, Nov. 2016
- [110] C. Liu and P. P. Vaidyanathan, “Robustness of difference coarrays of sparse arrays to sensor failures—Part I: A theory motivated by coarray MUSIC,” *IEEE Transactions on Signal Processing*, vol. 67, no. 12, pp. 3213-3226, June 2019.
- [111] C. Liu and P. P. Vaidyanathan, “Robustness of difference coarrays of sparse arrays to sensor failures—Part II: Array geometries,” *IEEE Transactions on Signal Processing*, vol. 67, no. 12, pp. 3227-3242, June 2019.
- [112] C. -L. Liu, “Optimal Coarray Combinations Robust to Sensor Failures on Sparse Arrays,” in *IEEE Signal Processing Letters*, vol. 29, pp. 1784-1788, 2022, doi: 10.1109/LSP.2022.3196600.
- [113] D. A. Linebarger, “A fast method for computing the coarray of sparse linear arrays,” *IEEE Transactions on Antennas and Propagation*, vol. 40, no. 9, pp. 1109-1112, Sept. 1992.

Appendix A

Proof of Lemma 3.3.1

Based on (5.5), the difference co-array of ENAMS array spans the range $[-N_2(N_1+) - N_1 + 3, N_2(N_1+) + N_1 - 3]$ for $N \geq 6$. Furthermore, due to the symmetric structure of the DCA, the following statements hold— i) if $p \in \mathbb{U}, \mathbb{U} \subseteq \mathbb{D}$, then $-p \in \mathbb{U}, \mathbb{U} \subseteq \mathbb{D}$, and ii) the first sensor or self-difference of one of the physical sensors contributes to lag $p = 0$. As such, we only need to show that there exists a lag p in the range $1 \leq p \leq N_2(N_1+) + N_1 - 3$. Thus, we consider the following cases:

- a) The lags in the range $1 \leq p \leq N_1 + 1$, can be realized by a difference set between \mathbb{Z}_2 and \mathbb{Z}_1 , i.e., $\text{diff}(\mathbb{Z}_2, \mathbb{Z}_1)$. Namely,

$$\text{diff}(\mathbb{S}_2, \mathbb{S}_1) = \{0, 1, \dots, N_1\}. \quad (8.1)$$

- b) On the other hand, the majority of the lags in the range $N_1 + 1 \leq p \leq N_2(N_1 + 1) - 2$, can be covered by

$$\text{diff}(\mathbb{S}_3, \mathbb{S}_1) = \{2N_1 + i(N_1 + 1) - j \mid i \in [0, N_2 - 2], j \in [1, N_1 - 2]\}. \quad (8.2)$$

And other few holes can be easily filled by the following sets: $\text{diff}(\mathbb{S}_3, \mathbb{S}_2)$, $(\mathbb{S}_4, \mathbb{S}_3)$, $(\mathbb{S}_5, \mathbb{S}_3)$, $(\mathbb{S}_4, \mathbb{S}_2)$ and $(\mathbb{S}_5, \mathbb{S}_2)$.

- c) Next, the difference set $\text{diff}(\mathbb{S}_4, \mathbb{S}_1)$ cover up the lags in the range of $N_2(N_1 + 1) - 2 \leq p \leq N_2(N_1 + 1) - 1$, i.e.,

$$\text{diff}(\mathbb{S}_4, \mathbb{S}_1) = \{N_2(N_1 + 1) - i \mid i \in [1, N_1 - 2]\}. \quad (8.3)$$

- d) Lastly, the lags in the final segment of range $N_2(N_1 + 1) \leq p \leq N_2(N_1 + 1) +$

$N_1 - 3$, can be realized by

$$\text{diff}(\mathbb{S}_5, \mathbb{S}_1) = \{N_2(N_1 + 1) + N_1 - 2 - i | i \in [1, N - 1]\}. \quad (8.4)$$

Thus, cases $a) - d)$ collectively cover the lags in the range $1 \leq p \leq N_2(N_1 + 1) + N_2 - 3$; therefore, the ENAMS array's difference co-array is hole-free.

Proof of Property 3.3.3

To prove Property 3.3.3, we consider checking the self-difference and the cross-difference sets of the ENAMS array.

For the self-difference sets, the sets $\text{diff}(\mathbb{S}_2, \mathbb{S}_2)$, $\text{diff}(\mathbb{S}_4, \mathbb{S}_4)$ and $\text{diff}(\mathbb{S}_5, \mathbb{S}_5)$ do not include sensors with separation 1, 2, 3 and so on, as they contain a single sensor only. Besides, $\text{diff}(\mathbb{S}_3, \mathbb{S}_3)$ yields $\pm(N_1 + 1)$, $\pm 2(N_1 + 1)$, up to $\pm(N_2 - 2)(N_1 + 1)$. It is only $\text{diff}(\mathbb{S}_1, \mathbb{S}_1)$ that include 0, ± 1 , ± 2 , ± 3 and so on. That's we have

$$(N_1 - 3), (N_1 - 4) \text{ and } (N_1 - 5), \quad (8.5)$$

sensor pairs with separations 1, 2, and 3, respectively. As for the cross-difference sets, the sets of interest are $\text{diff}(\mathbb{S}_2, \mathbb{S}_1)$, $\text{diff}(\mathbb{S}_4, \mathbb{S}_3)$, and $\text{diff}(\mathbb{S}_5, \mathbb{S}_4)$. Thus, examining the minimum elements of $\text{diff}(\mathbb{S}_2, \mathbb{S}_1)$ leads to

$$\min \text{diff}(\mathbb{S}_2, \mathbb{S}_1) = (N_1 + 1) - (N_1 - 2) = 3, \quad (8.6)$$

while evaluating the minimum elements of $\text{diff}(\mathbb{S}_4, \mathbb{S}_3)$ yields

$$\min \text{diff}(\mathbb{S}_4, \mathbb{S}_3) = N_2(N_1 + 1) - (N_2(N_1 + 1) - 2) = 2. \quad (8.7)$$

And, evaluating the minimum elements of $\text{diff}(\mathbb{S}_5, \mathbb{S}_4)$ leads to

$$\min \text{diff}(\mathbb{S}_5, \mathbb{S}_4) = N_2(N_1 + 1) + N_1 - 2 - N_2(N_1 + 1) = N_1 - 2, \quad (8.8)$$

which contributes to weights $w(n)$ for $n \leq 3$ if $N_1 \leq 5$. Thus, combining (8.15)-(8.8) add up to $w(1) = w(2) = N_1 - 3$ and $w(3) = N_1 - 4$.

Appendix B

Proof of Lemma 4.3.2

The proposition that the DCA of the f-ENAMS-I array has a \mathbb{U} in $\langle -N_u + 5N_1/2 - 1, N_u + 5N_1/2 - 1 \rangle$ where $N_u = N_2(N_1 + 1)$ is equivalent to the argument that for $m \in \mathbb{U}$, there is at least one pair of sensors that leads to it, and since DCA is a symmetric set, then it suffices to show that $0 \leq n \leq N_u + 5N_1/2 - 1$. To that end, we consider the following cases:

- a) The lags in $\langle 0, 3\mathcal{T} - 1 \rangle$ can be realized by considering the following sets

$$\text{diff}(\mathbb{S}_2, \mathbb{S}_1) = \{\mathcal{T}\langle 1, \mathcal{T} - 2 \rangle\} \cup \{3\mathcal{T} - \langle 1, \mathcal{T} - 2 \rangle\},$$

$$\text{diff}(\mathbb{S}_5, \mathbb{S}_4) = \langle \mathcal{T} - 3, \mathcal{T} \rangle \cup \langle \mathcal{T} + 1, 2\mathcal{T} - 2 \rangle,$$

except for holes at $\mathbb{H}_1 = \langle 0, \mathcal{T} - 3 \rangle$ and $\mathbb{H}_2 = (N_1 + 1)i$ for $0 \leq i \leq N_2 - 1$ which can be easily filled by $\text{diff}(\mathbb{S}_1, \mathbb{S}_1)$ and $\text{diff}(\mathbb{S}_3, \mathbb{S}_3)$, respectively.

- b) Regarding the lags in $\langle 3\mathcal{T}, N_u + N_1 - 1 \rangle$, we can consider the union of the following sets

$$\text{diff}(\mathbb{S}_3, \mathbb{S}_1) = \{N_u - \langle 1, \mathcal{T} - 2 \rangle\} \cup \{N_u + N_1 - \langle 1, \mathcal{T} - 2 \rangle\},$$

$$\text{diff}(\mathbb{S}_3, \mathbb{S}_2) = (\mathcal{T} + 1)\langle 1, N_2 \rangle \cup \langle 3\mathcal{T} + (\mathcal{T} + 1)\langle 0, N_2 - 1 \rangle + 2,$$

$$\text{diff}(\mathbb{S}_3, \mathbb{S}_4) = \mathcal{T}\langle 1, N_2 \rangle \cup (N_1 + 1)\langle 0, N_2 - 1 \rangle + N_1,$$

$$\text{diff}(\mathbb{S}_3, \mathbb{S}_5) = \{3\mathcal{T} - \langle 0, \mathcal{T} - 3 \rangle\} \cup \{N_u + \mathcal{T} - \langle 0, \mathcal{T} - 3 \rangle\}.$$

and

$$\text{diff}(\mathbb{S}_4, \mathbb{S}_2) = \{N_u + (\mathcal{T} + 1)\langle 0, N_2 - 1 \rangle + 1\} \cup \{N_u + N_1 + 1 - \mathcal{T}\langle 0, N_2 - 1 \rangle\}.$$

Thus, collectively these sets cover $\langle 3\mathcal{T}, N_u + N_1 - 1 \rangle$.

c) Finally, the lags in the range $\langle N_u + N_1, N_u + 5N_1/2 - 1 \rangle$ can be attributed to the following sets

$$\begin{aligned}\text{diff}(\mathbb{S}_5, \mathbb{S}_2) &= \{N_u + 3N_1/2 + 1 - \langle 0, \mathcal{T} - 3 \rangle\} \cup \{N_u + N_1 - \langle 0, \mathcal{T} - 3 \rangle\}, \\ \text{diff}(\mathbb{S}_4, \mathbb{S}_1) &= \{N_u + 3N_1/2 - \langle 1, \mathcal{T} - 2 \rangle\} \cup \{N_u + 2N_1 - \langle 1, \mathcal{T} - 2 \rangle\}, \\ \text{diff}(\mathbb{S}_5, \mathbb{S}_1) &= \langle 0, \mathcal{T} - 3 \rangle \cup \langle N_u + N_2, N_u + 5N_1/2 - 1 \rangle.\end{aligned}$$

Thus, combining these with fragments from $\xi(\mathbb{S}_4, \mathbb{S}_2)$ covers $\langle N_u + N_1, N_u + 5N_1/2 - 1 \rangle$.

In general, the union of cases (a)-(c) and their counter sets cover the consecutive integers in $\langle -N_u - 5N_1/2 + 1, N_u + 5N_1/2 - 1 \rangle$, i.e., the DCA of the f-ENAMS-I array is hole-free.

Proof of Property 4.3.3

According to Lemma 4.3.2, the L_u of the f-ENAMS-I array is $[0, N_2(N_1 + 1) + 5N_1/2 - 1]$, and assuming that $\lfloor N_1/2 \rfloor$, $\lfloor (N + 1)/4 \rfloor$ and $\lfloor (N + 3)/4 \rfloor$ are $N_1/2$, $(N + 1)/4$ and $(N + 3)/4$, respectively. The uniform DOF $|\mathbb{U}|$ of the f-ENAMS-I array can be expressed as

$$\text{uDOF} = 2L_u + 1 \approx 2N_2(N_1 + 1) + 5N_1 - 1 \quad (8.9)$$

As such, substituting the values of N_1 , and $N_2 = N - N_1$ while maximizing the uDOF under the constraint of $N = N_1 + N_2$ yields $N^2/2 + 3.5N - 28$, $N^2/2 + 3.5N - 6$ and $N^2/2 + 3.5N - 1$ given that $2\lfloor (N + 1)/4 \rfloor + 4$ when $\leq N \leq 14$, $2\lfloor (N + 1)/4 \rfloor + 2$ when $\leq N \leq 18$ and $2\lfloor (N + 3)/4 \rfloor$ when $N \geq 19$. Hence, Property 4.3.3 is proved.

Proof of Lemma 4.3.5

The proposition that the DCA of the f-ENAMS-II array has a \mathbb{U} in the range $[-N_2(N_1 + 1) + 7N_1/2 - 1, N_2(N_1 + 1) + 7N_1/2 - 1]$ is equivalent to the argument that for $m \in \mathbb{U}$, there is at least one pair of sensors that leads to it, and since DCA

is a symmetric set, then it suffices to show that $0 \leq n \leq N_2(N_1 + 1) + 7N_1/2 - 1$. To that end, we consider the following sections:

- a) The lags in the range $\langle 0, 3\mathcal{T} - 1 \rangle$ can be realized by taking the union of $\text{diff}(\mathbb{S}_2, \mathbb{S}_1)$ and $\text{diff}(\mathbb{S}_5, \mathbb{S}_4)$, i.e,

$$\text{diff}(\mathbb{S}_2, \mathbb{S}_1) = \langle 0, \mathcal{T} \rangle \cup \langle \mathcal{T} - 3, 2\mathcal{T} \rangle \cup \langle 3\mathcal{T} - 4, 3\mathcal{T} \rangle$$

and,

$$\text{diff}(\mathbb{S}_5, \mathbb{S}_4) = \langle \mathcal{T} + 1, 2\mathcal{T} - 3 \rangle \cup \langle 2\mathcal{T} + 2, 3\mathcal{T} - 3 \rangle \cup \langle 3\mathcal{T} + 3, N_u - 1 \rangle,$$

except for holes at $\mathbb{I} = (N_1 + 1)i$ which can be filled by $\text{diff}(\mathbb{S}_3, \mathbb{S}_3)$ which accounts for all lags $(N_1 + 1)i$ for $0 \leq i \leq N_2 - 1$.

- b) The lags in the range $\langle 3\mathcal{T}, N_u + N_1 - 1 \rangle$ can be realized by taking the union of $\text{diff}(\mathbb{S}_3, \mathbb{S}_1)$, $\text{diff}(\mathbb{S}_3, \mathbb{S}_2)$, $\text{diff}(\mathbb{S}_3, \mathbb{S}_4)$, $\text{diff}(\mathbb{S}_3, \mathbb{S}_5)$ and $\text{diff}(\mathbb{S}_4, \mathbb{S}_2)$, such that

$$\begin{aligned} \text{diff}(\mathbb{S}_3, \mathbb{S}_1) &= \{1 + \langle 1, N_2 \rangle\}(N_1 + 1) - 1\} - \langle 1, \mathcal{T} - 3 \rangle \\ &\approx \{N_u - \langle 1, \mathcal{T} - 4 \rangle\} \cup \{N_u + N_1 - \langle 1, \mathcal{T} - 3 \rangle\}, \end{aligned}$$

$$\begin{aligned} \text{diff}(\mathbb{S}_3, \mathbb{S}_2) &= \{1 + \langle 1, N_2 \rangle\}(N_1 + 1) - 1\} - \{\mathcal{T}\langle 1, 3 \rangle + 1\} \\ &\approx \{3\mathcal{T} + \langle 0, N_2 - 1 \rangle\} \cup \{N_u + \mathcal{T}\langle 0, N_2 - 1 \rangle - 1\}, \end{aligned}$$

$$\begin{aligned} \text{diff}(\mathbb{S}_3, \mathbb{S}_4) &= \{1 + \langle 1, N_2 \rangle\}(N_1 + 1) - 1\} - \{N_u + N_1 + (\mathcal{T} + 1)\langle 1, 3 \rangle\} \\ &\approx \{3\mathcal{T} + \langle 2, \mathcal{T} - 2 \rangle\} \cup \{N_u + (\mathcal{T} + 1)\langle 0, N_2 - 1 \rangle + 1\}, \end{aligned}$$

$$\begin{aligned} \text{diff}(\mathbb{S}_3, \mathbb{S}_5) &= \{(1 + \langle 1, N_2 \rangle\}(N_1 + 1) - 1\} - \{N_u + 3N_1 + \langle 1, \mathcal{T} - 3 \rangle + 3\} \\ &\approx \{N_u + \langle 2, \mathcal{T} - 2 \rangle\} \cup \{N_u + N_1 + 1\langle 1, \mathcal{T} - 3 \rangle\}, \end{aligned}$$

$$\begin{aligned} \text{diff}(\mathbb{S}_4, \mathbb{S}_2) &= \{N_u + N_1 + (\mathcal{T} + 1)\langle 1, 3 \rangle\} - \{\mathcal{T}\langle 1, 3 \rangle + 1\} \\ &\approx \{N_u + \mathcal{T} + \langle 1, 2 \rangle\} \cup \{N_u + N_1 + \langle 1, 3 \rangle\} \cup \{N_u + 3\mathcal{T} + \langle 1, 2 \rangle\} \cup \{N_u\langle 1, 2 \rangle\}. \end{aligned}$$

Thus, these sets cover the lags between the end of \mathbb{S}_2 to \mathbb{S}_3 .

- c) Considering the lags in $\langle N_u + N_1, N_u + 7N_1/2 - 1 \rangle$, this section can be filled

by the union of the following sets

$$\begin{aligned}\text{diff}(\mathbb{S}_4, \mathbb{S}_1) &= \{N_u + N_1 + (\mathcal{T} + 1)\langle 1, 3 \rangle\} - \langle 1, \mathcal{T} - 3 \rangle \\ &\approx \{N_u + 3N_1/2 - \langle 0, \mathcal{T} - 4 \rangle\} \cup \{N_u + 2N_1 + 2 - \langle 1, \mathcal{T} - 3 \rangle\} \\ &\quad \cup \{N_u + 5N_1/2 + 3 - \langle 1, \mathcal{T} - 3 \rangle\}.\end{aligned}$$

$$\begin{aligned}\text{diff}(\mathbb{S}_5, \mathbb{S}_2) &= \{N_u + 3N_1 + 3 + \langle 1, \mathcal{T} - 3 \rangle\} - \{\mathcal{T}\langle 1, 3 \rangle + 1\} \\ &\approx \{N_u + 2N_1 - \langle 1, \mathcal{T} - 3 \rangle\} \cup \{N_u + 5N_1/2 - \langle 1, \mathcal{T} - 3 \rangle\} \cup \{N_u + 3N_1 - \langle 1, \mathcal{T} - 3 \rangle\}.\end{aligned}$$

$$\begin{aligned}\text{diff}(\mathbb{S}_5, \mathbb{S}_1) &= \{N_u + 3N_1 + 3 + \langle 1, \mathcal{T} - 3 \rangle\} - \langle 1, \mathcal{T} - 3 \rangle \\ &\approx \langle 0, \mathcal{T} - 4 \rangle \cup \langle N_u + 3N_1, N_u + 7N_1/2 - 1 \rangle.\end{aligned}$$

Therefore, combining these sets with segments from $\text{diff}(\mathbb{S}_4, \mathbb{S}_2)$ accounts for the lags in $\langle N_u + N_1, N_u + 7N_1/2 - 1 \rangle$.

In general, the union of cases (a)-(c) cover the consecutive integers in $\langle 0, N_u + 7N_1/2 - 1 \rangle$, i.e., the DCA of the f-ENAMS-II array is hole-free.

Proof of Property 4.3.6

Following Lemma 4.3.5, the L_u of the f-ENAMS-II array is $N_2(N_1 + 1) + 7N_1/2 - 1$, and assuming that $\lfloor N_1/2 \rfloor$ and $\lfloor N/4 \rfloor$ are $N_1/2$ and $N/4$, respectively. The uniform DOF of the f-ENAMS-II array can be expressed as

$$\text{uDOF} = 2L_u + 1 \approx 2N_2(N_1 + 1) + 7N_1 - 1. \quad (8.10)$$

Therefore, substituting the values of N_1 and $N_2 = N - N_1$ whilst maximizing the uniform DOF under the constraint of $N = N_1 + N_2$ yields $N^2/2 + 4.5N - 43$ when $16 \leq N \leq 19$, $N^2/2 + 4.5N - 13$ when $20 \leq N \leq 23$ and $N^2/2 + 4.5N + 1$ when $N \geq 24$ given that $2\lfloor N/4 \rfloor + 6$, $2\lfloor N/4 \rfloor + 4$ and $2\lfloor N/4 \rfloor + 2$, respectively. Therefore, Property 4.3.6 is proved.

Appendix C

Proof of Lemma 5.3.1

The maximum position according to (5.11) is $Q(r + z) + z - 1$, and since \mathbb{D}_g is symmetric about position zero. Then, it suffices to show that the positive part of the consecutive set \mathbb{U} , $\mathbb{U}^+ = [1, 2, \dots, Q(r + z) + z - 1]$. Accordingly, based on (8.20)-(8.12), the DCA sets $\mathbb{D}_{1,2}$, $\mathbb{D}_{1,2}$, $\mathbb{D}_{1,2}$, $\mathbb{D}_{1,2}$ and $\mathbb{D}_{1,2}$ cover the range $[1, zP - 1]$. And, the sets $\mathbb{D}_{1,2}$, $\mathbb{D}_{1,2}$, $\mathbb{D}_{1,2}$, $\mathbb{D}_{1,2}$, $\mathbb{D}_{1,2}$, $\mathbb{D}_{1,2}$ and $\mathbb{D}_{1,2}$ generates the consecutive range $[zP, zP + Qr]$. Finally, the sets $\mathbb{D}_{1,2}$, $\mathbb{D}_{1,2}$, $\mathbb{D}_{1,2}$ and $\mathbb{D}_{1,2}$ generates the consecutive range $[zP + Qr + 1, Q(r + z) + z - 1]$. Thus, the three sections collectively generate the consecutive range $[1, Q(r + z) + z - 1]$, completing the proof.

$$\begin{cases} \mathbb{D}_{1,1} = \{0, 1, \dots, z - 1\}, \mathbb{D}_{1,2} = \{z, z + 1, \dots, 2z - 1\} \\ \mathbb{D}_{1,3} = \{(2 + i)P - j | i = j, i = 0 \leq i \leq z - 1\}, \\ \mathbb{D}_{1,4} = \{zP + Q(1 + i) - j | i = j, 0 \leq i \leq z - 1\}, \end{cases} \quad (8.11)$$

$$\left\{ \begin{array}{l}
\mathbb{D}_{1,5} = \{P(z+1) + Qr + i(P+1) - j | 1 \leq i \leq z, 0 \leq j \leq z-1\} \\
\mathbb{D}_{1,6} = \{2zP + Qr + z + i - j | i = j, 0 \leq i \leq z-1\}, \\
\mathbb{D}_{2,3} = \{(2+i)P - (2z+1) | 0 \leq i \leq z-1\}, \\
\mathbb{D}_{2,4} = \{zP + Qi - (2z+1) | 1 \leq i \leq r\}, \\
\mathbb{D}_{2,5} = \{zP + Qr + P + i(P+1) - (2z+1) | 1 \leq i \leq z\}, \\
\mathbb{D}_{2,6} = \{2zP + Qr + z + i - (2z+1) | 0 \leq i \leq z-1\}, \\
\mathbb{D}_{3,4} = \{zP + Qi - j | 1 \leq i \leq r, 2P \leq j \leq zP\}, \\
\mathbb{D}_{3,5} = \{zP + Qr + P + i(P+1) - j | 1 \leq i \leq z, 2P \leq j \leq zP\}, \\
\mathbb{D}_{3,6} = \{2zP + Qr + z + i - j | 1 \leq i \leq z-1, 2P \leq j \leq zP\}, \\
\mathbb{D}_{4,5} = \{Qr + i(P+1) - Qj | 1 \leq i \leq z-1, 1 \leq j \leq r\}, \\
\mathbb{D}_{4,6} = \{zP + Qr + z - (P+i) - Qj | 1 \leq i \leq z-1, 1 \leq j \leq r\}, \\
\mathbb{D}_{5,6} = \{P(z-1) + z + i - j(P+1) | 1 \leq i \leq z-1, 1 \leq j \leq z\}.
\end{array} \right. \tag{8.12}$$

Proof of Property 5.3.2

According to (5.10), and Lemma 5.3.1, it follows that

$$\text{uDOF} = 2L_u + 1 = 2Q(r+z) + 2z - 1. \tag{8.13}$$

Substituting the values of Q , r and z as defined in (5.10) into (8.13) yields

$$\text{uDOF} = \frac{2N^2}{3} + \frac{2N}{3} - 1, \tag{8.14}$$

and, therefore, completes the proof.

Proof of Property 5.3.3

Given the closed-form expression of the GENAMS array in (5.11), Property 5.3.3 can be proved by analyzing the self-difference and the cross-difference sets of the GENAMS array. Specifically, we consider set \mathbb{Z}_1 to \mathbb{Z}_6 as expressed in (5.11), and evaluate the sets containing sensor pairs with separation of 1, 2, and 3 as the main

contributors of weight functions $w(1)$, $w(2)$ and $w(3)$.

Beginning with the self-difference sets, the set $\text{diff}(\mathbb{Z}_4, \mathbb{Z}_4)$ generates lags with separation $0, \pm Q, \pm 2Q, \dots, \pm(r-1)Q$ whereas $\text{diff}(\mathbb{Z}_3, \mathbb{Z}_3)$ and $\text{diff}(\mathbb{Z}_5, \mathbb{Z}_5)$ do not include sensors with separation 1, 2, 3 and so on, as they contain lags with spacing $0, \pm P, \pm 2P, \dots, \pm(z-2)P$ and $0, \pm(P+1), \pm 2(P+1), \dots, \pm(z-1)(P+1)$, respectively. Besides, $\text{diff}(\mathbb{Z}_2, \mathbb{Z}_2)$ contains a single sensor only at location z . It is only $\text{diff}(\mathbb{Z}_1, \mathbb{Z}_1)$ and $\text{diff}(\mathbb{Z}_6, \mathbb{Z}_6)$ which include $0, \pm 1, \pm 2, \pm 3$ and so on. That's we have

$$2(z-1), \quad 2(z-2) \quad \text{and} \quad 2(z-3), \quad (8.15)$$

sensor pairs with separations 1, 2, and 3, respectively.

Concerning the cross-difference sets, the sets of interest are $\text{diff}(\mathbb{Z}_2, \mathbb{Z}_1)$ and $\text{diff}(\mathbb{Z}_3, \mathbb{Z}_2)$. Thus, examining the minimum elements of $\text{diff}(\mathbb{S}_2, \mathbb{S}_1)$ leads to

$$\min \text{diff}(\mathbb{S}_2, \mathbb{S}_1) = (2z-1) - (z-1) = z, \quad (8.16)$$

while evaluating the minimum elements of $\text{diff}(\mathbb{Z}_3, \mathbb{Z}_2)$ yields

$$\min \text{diff}(\mathbb{S}_4, \mathbb{S}_3) = 2P - (2z-1) = P, \quad (8.17)$$

which contributes to weights $w(n)$ for $2 \leq n \leq 3$ if $Q = 7$. Thus, combining (8.15)-(8.17) add up to $w(1) = 2z - 2$, $w(2) = 2z - 4$ and $w(3) = 2z - 6$. And therefore, complete the proof for Property 5.3.3.

Appendix D

Proof of Property 6.4.1

Given that the maximum aperture is $Rv + 2\mathcal{T}(m - 1) + 4m$, and the fact that the DCA \mathcal{D} is symmetric at the zeroth position. It is sufficient to demonstrate that the positive part of the consecutive ULA segment $\mathbb{U}^+ = [1, 2, \dots, Rv + 2\mathcal{T}(m - 1) + 4m]$. Therefore, for clarity, we construct the range $[1, Rv + 2\mathcal{T}(m - 1) + 4m]$ using three cases. Also, throughout this section, we assume that $q_1 \in [0, m - 1]$, $q_2 \in [1, m - 1]$ and $q_3 \in [1, m]$ as defined in (6.6):

- a) Using (6.6), the lags in the range $[1, m(\mathcal{T} + 1) - \mathcal{T}]$ can be determined by the difference sets $\mathcal{D}_{7,1}$, $\mathcal{D}_{5,6}$, and $\mathcal{D}_{5,7}$, besides $\mathcal{D}_{2,1}$, $\mathcal{D}_{3,1}$ and $\mathcal{D}_{3,2}$, which are also contributing lags in the same arnge. Namely,

$$\left\{ \begin{array}{l} \mathcal{D}_{2,1} = \{2(m - q_1) - 1\}, \\ \mathcal{D}_{3,1} = \{(\mathcal{T} - 1)q_2 + 2(m - q_1) - 1\}, \\ \mathcal{D}_{3,2} = (\mathcal{T} - 1)q_2 \\ \mathcal{D}_{6,5} = \{(m + q_2)(\mathcal{T} + 1) + 2q_3 - \mathcal{T} - 1 | i \in [1, v]\} \\ \mathcal{D}_{7,5} = \{(m - q_2)(\mathcal{T} + 1) + \mathcal{T}\}. \end{array} \right. \quad (8.18)$$

- b) Moreover, the lags in the range $[m(\mathcal{T} + 1) - \mathcal{T} - 1, Rv + m(\mathcal{T} + 1) - \mathcal{T} - 1]$

can be uniquely filled difference sets $\mathcal{D}_{5,4}$, $\mathcal{D}_{7,4}$, $\mathcal{D}_{5,3}$, $\mathcal{D}_{4,3}$, $\mathcal{D}_{4,1}$ and $\mathcal{D}_{4,2}$, i.e.,

$$\left\{ \begin{array}{l} \mathcal{D}_{4,1} = \{Ri - 2q_1 + m(\mathcal{T} + 1) - \mathcal{T} | i \in [1, v]\}, \\ \mathcal{D}_{4,2} = \{Ri + m(\mathcal{T} + 1) - 2\mathcal{T} + 1 | i \in [1, v]\} \\ \mathcal{D}_{4,3} = \{Rv + m(\mathcal{T} - 1) - \mathcal{T} - (\mathcal{T} - 1)q_2 + 1\} \\ \mathcal{D}_{5,3} = \{Rv + m(\mathcal{T} - 1) + 2q_2 - \mathcal{T} + 1\} \\ \mathcal{D}_{5,4} = \{R(v - i) + m(\mathcal{T} + 1)q_2 | i \in [1, v]\} \\ \mathcal{D}_{6,4} = \{R(v - i) + m(\mathcal{T} + 1) + 2q_3 - \mathcal{T} - 1 | i \in [1, v]\} \\ \mathcal{D}_{7,4} = \{R(v - i) + m(\mathcal{T} + 1) + \mathcal{T} | i \in [1, v]\}. \end{array} \right. \quad (8.19)$$

c) Finally, the difference sets $\mathcal{D}_{5,1}$, $\mathcal{D}_{6,1}$, $\mathcal{D}_{7,1}$, $\mathcal{D}_{5,2}$, $\mathcal{D}_{6,2}$, $\mathcal{D}_{7,2}$, $\mathcal{D}_{6,3}$ and rest of the sets account for the lags in the range $[Rv + m(\mathcal{T} + 1) - \mathcal{T}, Rv + 2\mathcal{T}(m - 1) + 4m]$.

$$\left\{ \begin{array}{l} \mathcal{D}_{5,1} = \{Rv + m(\mathcal{T} + 1) + (\mathcal{T} + 1)q_2 - 2q_1 - \mathcal{T}\} \\ \mathcal{D}_{6,1} = \{Rv + 2m(\mathcal{T} + 1) + 2(q_3 - q_1 - \mathcal{T}) - 1\}, \\ \mathcal{D}_{7,1} = \{Rv + 2m(\mathcal{T} - 1) + 4m - 2q_1\}, \\ \mathcal{D}_{7,2} = \{Rv + 2m(\mathcal{T} - 1) + 2m + 1\} \\ \mathcal{D}_{6,2} = \{Rv + 2m(\mathcal{T} + 1) + 2(q_3 - m - \mathcal{T})\} \\ \mathcal{D}_{5,2} = \{Rv + m(\mathcal{T} - 1) + (\mathcal{T} + 1)q_2 - \mathcal{T} + 1\} \\ \mathcal{D}_{7,3} = \{Rv + 2m\mathcal{T} - (\mathcal{T} - 1)q_2 + 1\} \\ \mathcal{D}_{6,3} = \{Rv + 2\mathcal{T}(m - 1) + 2q_3 - (\mathcal{T} - 1)q_2\} \\ \mathcal{D}_{6,5} = \{(m + q_2)(\mathcal{T} + 1) + 2q_3 - \mathcal{T} - 1 | i \in [1, r]\} \\ \mathcal{D}_{7,6} = \{2(R - q_3) + 1\}. \end{array} \right. \quad (8.20)$$

Therefore, the cases a)–c) accounts for the lags in the range $[1, Rv + 2\mathcal{T}(m - 1) + 4m]$, and therefore, completes the proof.

CV

Education

- * Ph.D., Electrical and Computer Engineering, Yokohama National University, Yokohama, Japan, September 2023.
- * M.S., Electrical and Computer Engineering, Yokohama National University, Yokohama, Japan, September 2020.
- * B.Ed., Electronics and Physics, University of Malawi, Zomba, Malawi, June 2018.

Professional Membership

- * The Institute of Electrical and Electronics Engineers (IEEE)
- * IEEE Signal Processing Society (IEEE SPS)

Publications

Journal Papers

- [1] S. Wandale and K. Ichige, Wandale, “Design of sparse arrays via deep learning for enhanced DOA estimation,” *EURASIP Journal of Advanced Signal Process*, 2021, 17 (2021), doi:<https://doi.org/10.1186/s13634-021-00727-5>.
- [2] S. Wandale and K. Ichige, “Simulated annealing assisted sparse array selection utilizing deep learning,” *IEEE Access*, vol. 9, pp. 156907-156914, 2021, doi:[10.1109/ACCESS.2021.3129856](https://doi.org/10.1109/ACCESS.2021.3129856).
- [3] S. Wandale, and K. Ichige, “Flexible extended nested arrays for DOA estimation: Degrees of freedom perspective,” *Signal Processing*, vol. 201, no.

108710, 2022. ISSN 0165-1684, <https://doi.org/10.1016/j.sigpro.2022.108710>.

- [4] S. Wandale and K. Ichige, “A generalized extended nested array design via maximum inter-element spacing criterion,” *IEEE Signal Processing Letters*, vol. 30, pp. 31-35, 2023, [doi:10.1109/LSP.2023.3238912](https://doi.org/10.1109/LSP.2023.3238912).
- [5] S. Wandale and K. Ichige, “xMISC: Improved sparse linear array via maximum inter-element spacing concept,” *IEEE Signal Processing Letters*, vol. x, pp. xx-xx, 2023, (under review).

Intenational Conference Papers

- [1] S. Wandale, T. Basikolo and K. Ichige, “Super nested sparse circular array for high-resolution DOA estimation,” *2019 IEEE International Symposium on Circuits and Systems (ISCAS)*, Sapporo, Japan, 2019, pp. 1-5, [doi:10.1109/ISCAS.2019.8702389](https://doi.org/10.1109/ISCAS.2019.8702389).
- [2] S. Wandale, T. Basikolo, and K. Ichige, “Super nested sparse circular array for high-resolution DOA estimation and its wideband extension,” *2019 International Radar Conference (RADAR)*, Toulon, France, 2019, pp. 1-4, [doi:10.1109/RADAR41533.2019.171416](https://doi.org/10.1109/RADAR41533.2019.171416).
- [3] S. Wandale and K. Ichige, “On the DOA estimation performance of optimum arrays based on deep learning,” *2020 IEEE 11th Sensor Array and Multichannel Signal Processing Workshop (SAM)*, Hangzhou, China, 2020, pp. 1-5, [doi:10.1109/SAM48682.2020.9104365](https://doi.org/10.1109/SAM48682.2020.9104365).
- [4] S. Wandale, and K. Ichige, “2D sparse array selection via deep learning,” *2020 International Symposium on Antennas and Propagation (ISAP)*, Osaka, Japan, 2021, pp. 445-446, [doi:10.23919/ISAP47053.2021.9391414](https://doi.org/10.23919/ISAP47053.2021.9391414).
- [5] S. Wandale and K. Ichige, “A nested array geometry with enhanced degrees of freedom and hole-free difference coarray,” *2021 29th European Signal Processing Conference (EUSIPCO)*, Dublin, Ireland, 2021, pp. 1905-1909, [doi:10.23919/EUSIPCO54536.2021.9616342](https://doi.org/10.23919/EUSIPCO54536.2021.9616342).
- [6] S. Wandale and K. Ichige, “Flexible extended nested array with multiple subarrays achieving improved degrees of freedom,” *2022 30th European Sig-*

nal Processing Conference (EUSIPCO), Belgrade, Serbia, 2022, pp. 1931-1935, doi:10.23919/EUSIPCO55093.2022.9909786.

- [7] S. Wandale and K. Ichige, “Enhanced maximum interelement constrained array design via simple hole-filling strategy,” *International Radar Conference 2023*, Sydney, Australia, 2023, pp. 1-5 (accepted).
- [8] K. Sato, S. Wandale, K. Ichige, K. Kimura and R. Sugiura, “Low-cost vehicle in-cabin occupancy detection using an approximate model of XG-Boost,” *International Radar Conference 2023*, Sydney, Australia, 2023, pp. 1-6 (accepted).

Local Conference Papers

- [1] S. Wandale and K. Ichige, “Undetermined direction of arrival estimation using super nested sparse circular arrays in the presence of mutual coupling,” *Signal Processing Symposium*, Tottori, Japan, pp. 1-2, 2019.
- [2] S. Wandale and K. Ichige, “Extended nested array with enhanced degrees of freedom and hole-free difference co-array,” *Signal Processing Symposium*, pp. 1-5, Nov. 2021.
- [3] S. Wandale and K. Ichige, “A novel sparse linear array design via generalized interelement spacing criterion achieving enhanced degree-of-freedom and hole-free difference co-array,” *Signal Processing Symposium*, Niigata, Japan, pp. 1-5, 2022.
- [4] S. Obata, S. Wandale and K. Ichige, “Underdetermined DOA estimation of correlated signals using atomic norm minimization,” *IEICE Tech. Report*, no. SIP2022-101, Maebashi, Japan, pp. 1-2, Jan. 2023.
- [5] S. Wandale and K. Ichige, “xMISC: A novel sparse linear array via maximum interelement spacing principle for DOA estimation,” *IEICE Tech. Report*, no. B-1-96, Nagoya, Japan, pp. 1, Sept. 2023.